Please provide feedback

Please support the ScholarWorks@UMBC repository by emailing scholarworks-group@umbc.edu and telling us what having access to this work means to you and why it's important to you. Thank you.

arXiv:2109.10350v1 [astro-ph.HE] 20 Sep 2021

Competitive X-ray and Optical Cooling in the Collisionless Shocks of WR 140

A. M. T. POLLOCK,[1] M. F. CORCORAN,[2,3] I. R. STEVENS,[4] C. M. P. RUSSELL,[3] K. HAMAGUCHI,[2,5] P. M. WILLIAMS,[6] A. F. J. MOFFAT,[7] G. WEIGELT,[8] V. SHENAVRIN,[9] N. D. RICHARDSON,[10] D. ESPINOZA,[3] AND S. A. DRAKE[2]

[1]*Department of Physics and Astronomy, University of Sheffield, Sheffield S3 7RH, UK*

[2]*CRESST and X-ray Astrophysics Laboratory, NASA/Goddard Space Flight Center, Greenbelt, MD 20771, USA*

[3]*The Catholic University of America, 620 Michigan Ave., N.E. Washington, DC 20064, USA*

[4]*School of Physics and Astronomy, University of Birmingham, Edgbaston, Birmingham, B15 2TT, UK*

[5]*Department of Physics, University of Maryland, Baltimore County, 1000 Hilltop Circle, Baltimore, MD 21250, USA*

[6]*Institute for Astronomy, University of Edinburgh, Royal Observatory, Edinburgh EH9 3HJ, UK*

[7]*Département de physique and Centre de Recherche en Astrophysique du Québec (CRAQ), Université de Montréal, C.P. 6128, Succ. Centre-Ville, Montréal, Québec, H3C 3J7, Canada*

[8]*Max-Planck-Institut für Radioastronomie, Auf dem Hügel 69, 53121 Bonn, Germany*

[9]*Sternberg Astronomical Institute, Moscow State University, Universitetskii pr. 13, Moscow, 119992 Russia*

[10]*Embry-Riddle Aeronautical University, Physics and Astronomy Department, 3700 Willow Creek Road, Prescott, AZ 86301, USA*

ABSTRACT

WR 140 is a long-period, highly eccentric Wolf-Rayet star binary system with exceptionally well-determined orbital and stellar parameters. Bright, variable X-ray emission is generated in shocks produced by the collision of the winds of the WC7pd+O5.5fc component stars. We discuss the variations in the context of the colliding-wind model using broad-band spectrometry from the *RXTE*, *Swift*, and *NICER* observatories obtained over 20 years and nearly 1000 observations through 3 consecutive 7.94-year orbits including 3 periastron passages. The X-ray luminosity varies as expected with the inverse of the stellar separation over most of the orbit: departures near periastron are produced when cooling shifts to excess optical emission in C III $\lambda5696$ in particular. We use X-ray absorption to estimate mass-loss rates for both stars and to constrain the system morphology. The absorption maximum coincides closely with inferior conjunction of the WC star and provides evidence of the ion-reflection mechanism that underlies the formation of collisionless shocks governed by magnetic fields probably generated by the Weibel instability. Comparisons with K-band emission and He I $\lambda10830$ absorption show that both are correlated after periastron with the asymmetric X-ray absorption. Dust appears within a few days of periastron suggesting formation within shocked gas near the stagnation point. X-ray flares seen in η Car have not occurred in WR 140, suggesting the absence of large-scale wind inhomogeneities. Relatively constant soft emission revealed during the X-ray minimum is probably not from recombining plasma entrained in outflowing shocked gas.

Keywords: plasmas — shock waves — stars: Wolf-Rayet — stars: individual (WR 140) — X-rays: stars

1. WR 140: A COLLIDING-WIND BINARY LABORATORY

Massive stars, though extremely rare in the local Universe, are important cosmic engines which generate those chemicals critical for planetary habitability. There are many open questions about how these unusual stars evolve and die, mostly having to do with mass and angular momentum loss during their short lives (e.g. Meynet & Maeder 2003), and how such losses depends on the (evolving) underlying stellar parameters of effective gravity, temperature and chemical abundance, and on initial rotation rate and other complicating factors. Additionally, the majority of massive stars either have binary companions or were part of a multiple system at some point in their history (Sana et al. 2012), so that binary-driven mass exchange and loss can play an important evolutionary role (Vanbeveren et al. 1979; Eldridge et al. 2008), and may play a key role in forming massive gamma-ray burst progenitors by enhancing the stellar rotation rate (Langer et al. 2010). Massive binaries are the progenitors of the gravitational wave mergers seen

by *LIGO*, but the evolutionary pathway between progenitor massive binary systems and *LIGO* sources is uncertain, and an area of current interest (see, for example, Kruckow et al. 2018).

Observations of massive binaries serve as the touchstone for models of stellar structure and evolution in the upper Hertzsprung-Russell Diagram, since the mass and radius of stars in binary systems can be directly measured using simple Newtonian mechanics and Euclidean geometry, as long as the observer is fortuitously oriented with respect to the orbital plane of the system, or clever enough. Massive binaries provide an observational connection between the underlying stellar parameters and stellar wind mass loss (for example, Corcoran & Heap 1990). Wind properties (densities and terminal velocities) have been determined using radio measures of thermal free-free emission (Wright & Barlow 1975); analysis of UV spectra of P-Cygni profiles in resonance lines (Snow & Morton 1976); and through measures of broad optical emission lines (Leitherer 1988). However, each of these methods carries its own assumptions, biases, and uncertainties.

Study of the orbital dependence of the X-ray emission from massive colliding-wind binaries is an independent and increasingly important means for constraining the properties of stellar wind mass-loss. This is because the localized "bow-shock" created where the winds from massive binary companions collide produces high-temperature gas which emits in the thermal X-ray band (0.1–10 keV). Because the X-ray emission occurs near the apex of the colliding-wind shock, it can be used as a probe of local conditions of the stellar winds in situ. The X-ray emission measures, temperatures and absorption column densities derived from analysis of the X-ray spectrum as a function of orbital phase provide unique measures of the dependence with distance from the photospheres of the densities and speeds of the stellar winds. Theoretical modeling of X-rays produced by colliding-wind shocks dates back more than forty years (Prilutskii & Usov 1976; Cherepashchuk 1976) and has remained an active area of research as computational resources and numerical models have become more sophisticated (e.g. Stevens et al. 1992; Usov 1992; Pittard 2007; Pittard & Parkin 2010; Parkin & Gosset 2011; Russell et al. 2013).

The small number of highly eccentric, long-period WR+O binaries are a particularly important means to establish the connection between stellar wind properties and stellar parameters through X-ray variability studies. Such systems offer a number of observational advantages. Since the stellar separation varies as the stars pass from apastron to periastron and back again, the emission measure of the shocked material along the wind collision boundary varies with orbital phase and constrains the spatial wind density distribution from apastron through periastron passage and back again. X-ray temperatures constrain the local stellar wind velocities of the upstream pre-shocked gas near the point of impact as a function of stellar separation. Variations in X-ray absorption, produced by the unshocked stellar winds as the stars orbit each other, constrain mass loss rates and the geometry of both the shocked and unshocked winds. In addition, because the stars are well separated for most of the orbit, mass transfer might only occur now near periastron, although a modest amount has probably taken place earlier over the course of WR 140's evolution (Thomas et al. 2021).

The outstanding example of an eccentric, long-period, X-ray-variable colliding-wind binary is undoubtedly WR 140 (HD 193793), a WC7pd+O5.5fc binary of period 7.94 years and eccentricity 0.900. Its exceptional nature was first recognized via periodic dust formation events (Williams et al. 1978, 1987, 1990, 1994; Williams 1996; Williams et al. 2009). This periodic outpouring of dust served as the "smoking gun" to establish the system's long-period and extreme eccentricity which is one of the highest of all known stellar binary systems[1]). Its orbit and the properties of both stars have been well established from ground-based observations (Dougherty et al. 2005; Monnier et al. 2011; Fahed et al. 2011). New analysis by Thomas et al. (2021), hereafter T21, using optical interferometry from the Center for High Angular Resolution Astronomy (CHARA) Array, combined with archival interferometry and new and archival stellar spectra, has provided precise values for the orbital elements and stellar masses. As a result of these detailed studies, WR 140 has the best established stellar and orbital parameters of any WR-type binary, rivalling other very high-eccentricity systems of assorted spectral type discussed, for example, by Farrington et al. (2018).

In a wider context, the shocks generated by the wind interactions in massive stellar binary systems and WR 140 in particular (Pollock et al. 2005) are prime and arguably optimal exemplars of the physics of collisionless shocks. Collisionless shocks play important roles throughout the Universe in the dynamics of plasmas across the widest range of settings (e.g. Marcowith et al. 2016; Dimmock et al. 2019) from the flow of the solar wind into the Earth's magnetosphere and later into the heliopause; through supernova remnants blasting into the interstellar medium; to merging clusters

---

[1] There are 38 binary systems with orbital eccentricity> 0.89 in the 9th Catalog of Spectroscopic Binaries (Pourbaix et al. 2004) of which WR 140 is the only WR binary. Worth noting, the peculiar massive long-period binary η Car also has a high orbital eccentricity (near 0.9, Madura et al. 2012, though it has not been directly measured). The catalogued system with the highest eccentricity is the low-mass binary HD 137763 ($P = 889.95$ days, $e = 0.976$).

of galaxies. The behaviour of all these systems is governed by interlocking varieties of physics that encompass one or more of shock formation, development and dissipation; independent ion and electron heating and cooling, excitation and emission; non-thermal particle acceleration; dust formation; magnetic field generation and reconnection; plasma waves; turbulence; and dynamical instabilities. WR 140 exhibits many of these in tightly constrained conditions. It is bright, nearby and unobscured enough to offer observers unrivalled opportunities for the remote study of shock physics to contrast and complement measurements made in solar system space and laboratories on earth. By virtue of the combination of this precision with its exceptional brightness, X-ray emission from WR 140 currently serves as a uniquely valuable resource for the study of the behavior of collisionless astrophysical shocks under predictable, repeatable, time-dependent physical conditions.

WR 140 was first detected as a luminous X-ray source on 1984 May 19 by the *EXOSAT* observatory (Pollock 1985), at what subsequently proved to be orbital phase 0.889, and has been observed many times since by X-ray observatories like *ROSAT* (Pollock et al. 1995), *ASCA* (Koyama et al. 1994; Zhekov & Skinner 2000), *XMM-Newton* (De Becker et al. 2011), *CHANDRA* (Pollock et al. 2005) and *Suzaku* (Sugawara et al. 2015). WR 140 is the brightest X-ray source among all single or binary massive stars, rivaled only by η Car with which it shares a similar range of observed count rates in many instruments. While the X-ray brightness of WR 140 has obvious advantages, at the same time care is required regarding the choice of observing modes in order to avoid where possible adverse instrumental effects such as photon pile-up.

Here we report detailed X-ray monitoring of the system from observations with *RXTE*, *Swift*, and *NICER*, emphasizing the broad-band variations revealed as the stars revolve in their orbits, on timescales of days to weeks, over 3 orbital cycles according to the orbital and stellar parameters given in Table 1. Most have been accurately determined through observations except perhaps the more uncertain O-star mass loss, for which we have adopted the preferred smallest of the clumping-free rates reported by Pittard & Dougherty (2006). Also given, to inform the discussion below, are shock-cone opening angles, θ_S, and the shock stand-off distance from the WC7 star as a fraction of the binary separation, D. These were derived from analytical geometrical models of radiative and adiabatic binary shock formation (Canto et al. 1996; Gayley 2009) and depend on the momentum flux ratio, η. Their rigor and applicability were assessed by Pittard & Dawson (2018) based on 2D numerical fluid simulations.

We investigate variations of the emergent X-rays in the intensity and spectrum of the shock emission as modulated by photoelectric absorption during transfer through cooler pre-shock wind and the interstellar medium, on timescales according to orbital phase from hours and days to years and beyond, over the three most recent orbital cycles that span the first 20 years of the 21st century. As expected, in common with longer-wavelength regimes, X-ray events move much more quickly near periastron than at other phases, so we requested observations at increasingly higher cadence in order to sample appropriate details of the system's emerging behaviour when the stars are close. Ultimately nearly a thousand separate observations have been accumulated and analyzed.

In WR 140's eccentric 7.94-year orbit, the succession of Keplerian events of geometrical relevance occur within a few months of periastron: the O star is in front at −129 days; followed by quadrature when the stars are sideways on with the WC star moving towards the observer at −10 days; the WC star in front at +9 days; and quadrature with the WC star moving away at +104 days. These times are accurate to about a day near periastron and a week otherwise. Between periastron and apastron, the distance between the companion stars varies from 1.5 to 27.5 AU, similar to the separations of Mars and Neptune from the Sun.

The paper is organized as follows: Section 2 presents an overview of the X-ray satellite observatories, *RXTE*, *Swift*, and *NICER*, and their work on WR 140. In Section 3 we derive a suitable spectral model for WR 140 which we then use consistently to model the spectra from all three observatories. In Section 4, we present the full X-ray lightcurve from 2001 through 2020, and discuss the variations of the spectral parameters as a function of time and orbital phase paying special attention in Section 5 to the mechanisms of shock formation and cooling in WR 140. Section 6 discusses the implications for the understanding of the mass loss from the WR and O components, and we summarize the main results in Section 7.

2. THE OBSERVATIONS

There are a total of 940 observations of WR 140 by *RXTE*, *Swift* or *NICER*, for a total exposure of 1342.0 ksec, included here. Table 2 summarizes the observations for each of the missions.

2.1. *RXTE*

Table 1. Adopted Orbital and Stellar Parameters

Parameter	Value	Reference or Comment
Period (days)	2895±0.17	T21 (from Table 3, "Adopted Fit")
eccentricity	0.9883 ± 0.0013	T21
Time of Periastron Passage (MJD)	60637.23 ± 0.53	Best fit T_o from T21
ω_{WR} (degrees)	227.44 ± 0.52	T21
Ω (degrees)	353.87 ± 0.67	T21
i (degrees)	119.07	T21
a (AU)	13.55± 0.21	T21
M_{WR} (M$_\odot$)	10.31 ± 0.45	T21
M_O (M$_\odot$)	29.27 ± 1.14	T21
$\dot{M}_{WR}$ (10^{-6}M$_\odot$ yr^{-1})	43.0	Pittard & Dougherty (2006)
$\dot{M}_O$ (10^{-6}M$_\odot$ yr^{-1})	0.8	Pittard & Dougherty (2006)
$V_{\infty,WR}$ (km s^{-1})	2860	Setia Gunawan et al. (2001)
$V_{\infty,O}$ (km s^{-1})	3100	Setia Gunawan et al. (2001)
η	49.6	$= (\dot{M}_{WR}V_{\infty,WR})/(\dot{M}_O V_{\infty,O})$
Adiabatic-Shock Opening Angle (degrees)[a]	41.3	Gayley (2009) equation (11)
Radiative-Shock Opening Angle (degrees)[a]	31.7	Canto et al. (1996) equation (28)
WR-Shock Stand-off Distance[b]	0.876	Canto et al. (1996) equation (27)
Distance (pc)	1518	Gaia DR2 & T21
v	7.07	Massey (1984)
$b-v$	+0.27	Massey (1984)
N_H (10^{21} cm^{-2})	4.3	Interstellar absorption column density

[a] Theoretical asymptotic opening half-angle determined by η

[b] Fraction of binary separation determined by η

The *Rossi X-ray Timing Explorer* (*RXTE*, Bradt et al. 1993), which operated between 1995 December and 2012 January, was a satellite observatory with the flexibility to observe variable X-ray emitting cosmic objects on timescales from microseconds to years. The primary instrument, the Proportional Counter Array (PCA, Jahoda et al. 2006; Shaposhnikov et al. 2012), was an array of collimated, non-imaging proportional counters with a field-of-view of about $1°$, sensitive to X-rays emitted in the $\sim 3 - 60$ keV band. This band includes a significant fraction of the absorbed emission generated within WR 140's wind-wind collision shock which falls almost entirely between 0.5 and 10 keV. However, the lack of soft response below 3 keV made *RXTE* insensitive to column density variations at relatively low values of $N_H \lesssim 10^{22}$ cm^{-2}. Also, *RXTE*'s wide field-of-view means that PCA spectra are contaminated by cosmic background at a level dependent on satellite roll angle. *RXTE* had limited spectral resolution ($E/\Delta E = 3.45$ - 6.15) between 3 and 8 keV, too coarse for studies of emission lines.

The first observation of WR 140 by *RXTE* was obtained on 2000 December 09, 63 days before WR 140's periastron passage (which occurred on 2001 February 10), after which *RXTE* observed the system approximately once per week for just over two years. After a two year hiatus starting in 2003 March, observations resumed on 2005 March 08, 39 days after apastron ($\phi = 0.513$), and continued for six years until 2011 December 23, just before end of mission, at a variable cadence of a few observations per month to one per day during the periastron passage and X-ray minimum in 2009 January. As for many space observatories, *RXTE* observing time was awarded on an annual basis so that its cumulative WR 140 campaign comprised 8 separate proposals after being initiated to inform the context of two *CHANDRA* observations of WR 140 being made at the time and whose success they helped guarantee. These data have been discussed previously (Corcoran et al. 2011; Pollock 2012). Most recently, Zhekov (2021) analyzed these data (along with *CHANDRA* X-ray spectra) and suggested that the stellar winds are significantly clumped and/or non-spherically symmetric.

Though the PCA consists of 5 individual Proportional Counter Units (PCUs, conventionally numbered 0–4), we concentrate here on data from PCU-2, which provides the most complete and reliable data, and in particular, the data obtained in Layer 1 of PCU-2, where most of the X-rays from a relatively soft source like WR 140 are measured. We obtained and analyzed these data from the *RXTE* data archive at the HEASARC, NASA's archive of high energy space mission data. For each observation, we created individual responses for and instrumental background estimates of the

Table 2. Summary of the Observations

Instr.	Num. Obs.	Tot. Expo.	Obs. Start	Obs. End	Min. Expo.	Max. Expo.	Min. Sep.
		ksec	MJD	MJD	s	s	day
RXTE PCA	533	510	51887	55919	16	2192	0.55
Swift PC	145	313	54689	57891	376	19760	0.06
Swift WT	173	391	54843	58588	79	18648	0.07
NICER XTI	89	128	58074	59002	57	4501	0.05

Note—Tot. Expos. is the sum of the exposures for the individual observations; Obs. Start, End are the start and stop of the observing campaigns in MJD; Min., Max. Expo. are the minimum and maximum exposure for individual observations; Min. Sep. is the minimum separation between consecutive observations

PCU-2 layer 1 data using software tools (`pcarsp` and `pcabackest`) provided by the *RXTE* Guest Observer Facility and distributed with the HEASARC's `HEASoft` software package. Note that the background estimates provided by `pcabackest` provide estimates of the internal detector background and external charged particle background and do not account for cosmic background. Thus the amount of residual cosmic "sky" background included in the $\approx 1°$ field of view of PCU-2 will be different than the amount of residual cosmic background in imaging observations (such as the *Swift* XRT in photon-counting mode) or non-imaging instruments with narrower fields of view (like *NICER*). Difference in cosmic background in the different instruments complicates comparison between the various observatories. We used calibrations from the most recent version of the PCA calibration data (version 20120110) obtained from the *HEASARC RXTE* Calibration Database (CALDB).

2.2. *Swift*

We used the X-ray Telescope (XRT, Burrows et al. 2000) on the *Neil Gehrels Swift* observatory (*Swift*, Gehrels et al. 2004) to monitor changes in the X-ray spectrum. *Swift* was used to augment the *RXTE* data since the XRT's softer instrumental sensitivity and better spectral resolution allow for more precise determination of column densities than possible with *RXTE*. On the other hand, the XRT is prone to light leaks at low energies, which can complicate analysis of the soft part of the X-ray spectrum where the effect of wind absorption is most pronounced. This contamination, known as optical loading, has been particularly relevant in the treatment of the soft "relic" component (Sugawara et al. 2015, Section 4.5 below) revealed during WR 140's X-ray minimum near periastron.

The XRT is also susceptible to photon pile-up in imaging ("Photon-Counting", hereafter PC) mode observations if more than one X-ray photon strikes a pixel of the XRT detector before readout, reducing the observed count rate and distorting the spectrum. The count-rate threshold above which this becomes significant is about 0.5 cts s^{-1} and applies to most of WR 140's orbit except the minimum near periastron. This was not understood during the early XRT observations. Though data analysis methods available to mitigate the problem have been used, the XRT's alternative "Windowed-Timing" mode (hereafter WT), was later usually judged preferable. Its faster readout incurs the loss of spatial information in one direction leading to higher backgrounds and more difficult treatment of bad detector columns.

The *Swift* XRT observations of WR 140 started on 2008 August 11, with sporadic phase coverage. The last observation we analyze here was taken on 2018 April 05. *Swift*, along with *Suzaku* (Sugawara et al. 2015), provided critical measurements of the variation in the WR 140's soft X-ray spectrum near the 2009 periastron passage since only *Swift* and *Suzaku* were available to measure the WR 140 X-ray spectrum below 3 keV at that time[2].

The *Swift* data were downloaded from the *HEASARC* data archive, then reprocessed using the standard pipeline software (`xrtpipeline`, part of the *Swift* XRTDAS software distributed with the HEASoft Analysis package). We calculated individual effective areas for the PC and WT mode data. We visually inspected each observation and defined valid "good-time" intervals from extracted lightcurves, avoiding times of large excursions in count rates produced by

---

[2] WR 140 violated viewing constraints of *XMM-Newton*, and mitigation of photon pileup in the *CHANDRA* ACIS camera would have resulted in prohibitively long exposures. In addition, at that time it was unclear if the *RXTE* mission would be extended beyond February 2009; if not, it would have been up to *Swift* alone to monitor the details of the recovery of WR 140's X-ray flux from the X-ray minimum state.

background fluctuations or other, non-source-related variations. We then extracted spectra and lightcurves from the X-ray events which fell within these good time intervals. For the PC-mode data, source spectra were extracted from a circular region of radius $1.1'$ centered on WR 140. Background was extracted from an annulus between $2.7'$ and $8.3'$, whose inner boundary extends beyond the *Swift* PC-mode 90% encircled energy radius, and which contained no visible X-ray sources. For each PC-mode spectrum we calculated observation-specific effective areas using the `xrtmkarf` task distributed with the *Swift* XRTDAS, and used the standard XRT PC-mode response function from version 20170501 of the *Swift* XRT CALDB in the spectral analysis.

For the WT mode data, neither pileup nor optical loading is a significant issue. For data in windowed-timing mode, source photons were extracted from a region extending to $1.1'$ around the source in the 1-D spatially compressed image, while background was extracted from an apparently source-free region extending to $1.1'$ in the 1-D spatially compressed image. Because of the compression in the spatial dimension, the background spectrum in the windowed-timing mode data depends on the spacecraft roll angle since cosmic sources and bad detector columns included in the spatially-compressed vary with roll angle. Thus the WT mode backgrounds are in general different from the backgrounds in photon-counting mode but, from examination of a few selected datasets at different roll angles, we estimate that the variation between background levels in different WT observations is probably less than 5%. We computed individual, observation-specific effective areas for all the WT-mode data and analyzed the data using the standard WT-mode response function. Comparison of net fluxes derived from PC-mode data with those derived from the analysis of net WT-mode data indicates that the net WT-mode data are in general 40% brighter than the net PC-mode data, presumably due to an under-estimation of background contamination in the WT-mode data.

2.3. *NICER*

The Neutron Star Interior Composition Explorer (*NICER*, [Arzoumanian et al. 2014]) is an X-ray astronomy facility which was installed on the International Space Station (ISS) in June 2017. *NICER*'s primary mission is to obtain high-time resolved X-ray spectrometry in the 0.2–12 keV band with moderate spectral resolution of cosmic X-ray sources, primarily of X-ray binary pulsars. *NICER*'s X-ray Timing Instrument (XTI, [Prigozhin et al. 2016]) is comprised of a co-aligned array of 52 Focal Plane Modules, each consisting of a matched pair of X-ray "concentrator" (XRC) optics a silicon drift detector (SDD) for readout. Each XRC optic collects X-rays over a roughly 30 arcmin^2 region of the sky centered on the target of interest in the 0.2–12 keV energy band and concentrates them onto an SDD. *NICER*'s combination of large effective area, restricted field of view and broad bandpass in the thermal X-ray range makes it especially well-suited to observe X-ray variables like long-period colliding wind binaries (and other sources) in addition to X-ray pulsars.

The *NICER* data were extracted from the clean, merged photon events files, using data obtained outside of the South Atlantic Anomaly at sun angles of $> 40°$ to avoid stray-light contamination, using the NICERDAS software package distributed with HEASoft. We used standard *NICER* event cleaning criteria[3] to clean each observation. *NICER* is subject to a varying charged particle environment at the high-inclination ISS orbit, which is most noticeable at high energies, so we extracted lightcurves in the $0.4 − 10$ keV band for all the *NICER* observations and visually inspected them to exclude intervals of large rapid increases in count rate produced by the variable charged particle environment. In addition, low-energy events produce a "noise spike" at energies $\lesssim 0.4$ keV. Therefore, in our analysis, we extracted and fit spectra in the 0.4–10 keV band, which has good overlap with *Swift* and *RXTE* and excludes the *NICER* spectral bands most affected by background issues. For each observation we estimated background using the `nibackgen3C50` tool[4] ([Remillard et al. 2021]) provided by the *NICER* Guest Observer Facility, which estimates background from a library of spectra extracted from blank-field observations, using rates at energies beyond the XRC cutoff and other proxies. We subtracted this background estimate from the observed spectrum for each observation before fitting.

3. DETERMINING A SPECTRAL TEMPLATE MODEL

In order to determine a uniform set of phase-dependent broadband X-ray spectral parameters from the moderate resolution data delivered by *RXTE*, *Swift*, and *NICER* we created a template model of the spectrum using high-resolution *CHANDRA* grating spectrometer data, as these contain the most detailed information on the combination of lines and continuum. In particular, we chose three *CHANDRA* ObsIDs, 6286, 5419 and 6287, obtained over a two week period in 2006 March and April, only 14 months (0.15 in orbital phase) after the stars passed apastron (on

---

[3] see the help file for `nimaketime` for a description of the standard data screening criteria.

[4] See https://heasarc.gsfc.nasa.gov/docs/nicer/tools/nicer_bkg_est_tools.html.

2005-01-28). These spectra show the plasma in its most relaxed condition, and stellar wind absorption at or near its lowest. The total exposure time of the combined spectrum is 141 ks. Because of the resemblance of the spectrum to thermal emission, we used a simple combination of plasma models in collisional equilibrium with the same adjustments for velocity broadening and non-solar abundances and subject to absorption by the interstellar medium and the stellar winds, and used XSPEC (Dorman & Arnaud 2001) to fit the combined set of 12 MEG and HEG first-order spectra.

The model we adopted was selected for its ability to reproduce the morphology of the spectrum, so it does not necessarily represent a realistic description of the actual physics of the plasma which is more likely to be out of equilibrium as discussed, for example, by Pollock et al. (2005). In XSPEC notation, the model is (TBabs(bvapec$_1$ + bvapec$_2$ + bvapec$_3$), where TBabs is the "Tuebingen-Boulder ISM absorption model" (Wilms et al. 2000, which was used to estimate the combination of ISM and stellar wind absorption columns to the X-ray source), and the three bvapec components are non-solar-abundance ("v"), doppler-broadened ("b") plasma emission models (Smith et al. 2001)[5]. When absorption becomes high as the Wolf-Rayet star moves in front of the colliding-wind source a weak additional soft component not captured by the template model becomes visible, amounting to less than 0.25% of the maximum count rate. Known by Sugawara et al. (2015) as the "relic" component, its behavior is discussed below in section 4.5.

Abundances were held in common for the three thermal emission components and are mostly representative of the shocked wind of the chemically-evolved WC7 star with a minor contribution, amounting to less than 10% according to Pittard & Stevens (2002), from the shocked wind of the less chemically-evolved O star. In order to accommodate this, with hydrogen absent in the WC7 star and replaced by helium, the abundances of the *CHANDRA* emission model were fixed: helium to a high value; carbon to a number fraction C/He = 0.4; and nitrogen to zero.

The reference template model parameters from the *CHANDRA* fit are given in Table 3 including the best-fit abundances used for all three emission components, given with respect to solar abundances (Anders & Grevesse 1989) and as number and mass fractions. The best-fit emission measures of the three thermal components to the HETGS spectra were fixed at values adjusted downwards by an indicative factor of 1.061 calculated from the relative binary separation of the orbit between apastron and the later mean epoch of observation. With density estimates based on parameters in Table 1, these emission measures equate to volumes of less than 1% of a characteristic volume given by $(1 - \cos\theta_S)D^3$. Other than the relic component, the luminosity scaling factor was one of the two free parameters of the template model along with the absorbing column density whose initial value was also thought to be characteristic of low values at apastron or maximum binary separation, although expectations at the outset were ill-defined of its overall phase dependence. The line-velocity structure was also frozen in the template model, since line velocity broadening is only of relevance at high (grating) resolution. The HETG spectrum and template model, including the 3 individual emission components representing emission from the shocked gas in the wind collision region, is shown in Figure 1.

We then fit this "standard" X-ray spectrum model to each individual spectrum from the *RXTE*, and *Swift* observations, fitting for the overall column densities, using an overall constant to adjust the flux normalization of the model, with the temperatures and relative emission measures of the emission model fixed. We found that this was adequate to generate acceptable fits to the low-resolution *RXTE* spectra and the relatively low precision *Swift* and *NICER* spectra (null hypothesis probablilty > 0.05) which therefore gave no evidence of any change with orbital phase of the adopted equivalent plasma temperatures although this conclusion is ripe for exploration with high resolution data.

We used an automated Python script to fit the data, using pyxspec, the Python version of the XSPEC spectral analysis package. We recorded values of all variable parameters, namely those not fixed in Table 3, for each spectrum and calculated observed and absorption-corrected fluxes in the 2–10 keV band for all observations. We adopted the 2–10 keV band as standard, since it is consistent with the harder response of *RXTE* that does not extend much below 2 keV and includes the bulk of the colliding-wind emission. Any intrinsic emission from the individual stellar winds is also likely to be mostly confined to the soft band below 2 keV although even this is weak in WR 140: the residual soft emission near periastron discussed in Section 4.5 below amounts to less than 2% of the colliding-wind emission in the same band observed at apastron.

## 4. X-RAY VARIABILITY IN WR 140

---

[5] see http://atomdb.org.
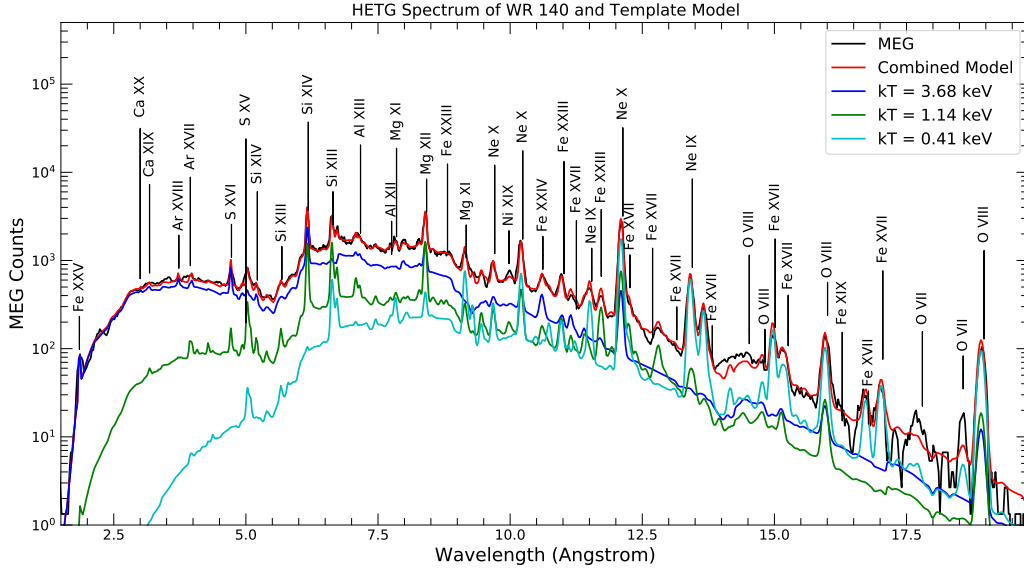
Figure 1. *CHANDRA* HETG combined ±1st order MEG spectra from the ObsIDs 6286, 5419, 6287 of WR 140 (black) closest to apastron and the standard template model (red). Strong lines in the 1–20 Å region are marked among which those of Ne X and O VIII are particularly strong.

Table 3. X-ray Spectrum Template Model

Parameter	Unit	Initial Value	Type
nH	10^{22} cm^{-2}	0.50	
kT$_1$	keV	3.68	Fixed
EM$_1$	10^{53} cm^{-3}	3.87	Fixed
kT$_2$	keV	1.14	Fixed
EM$_2$	10^{53} cm^{-3}	1.42	Fixed
kT$_3$	keV	0.41	Fixed
EM$_3$	10^{53} cm^{-3}	1.54	Fixed
Velocity Shift	1000 km s^{-1}	-1.37	Fixed
Line Broadening	100 km s^{-1}	5.78	Fixed
Normalization factor		1.0	

Fixed Emission Abundances by number, N, and mass fraction, X			
	N/N$_\odot$	N	X
He	1000	1.	0.548
C	65247	0.242	0.398
N	0	0.	0.
O	1938	1.69×10^{-2}	3.70×10^{-2}
Ne	3139	3.95×10^{-3}	1.09×10^{-2}
Mg	1061	4.13×10^{-4}	1.37×10^{-3}
Al	976	2.95×10^{-5}	1.09×10^{-4}
Si	881	3.20×10^{-4}	1.23×10^{-3}
S	713	1.18×10^{-4}	5.18×10^{-4}
Ar	602	2.24×10^{-5}	1.22×10^{-4}
Ca	374	8.75×10^{-6}	4.80×10^{-5}
Fe	297	1.42×10^{-4}	1.09×10^{-3}
Ni	385	7.02×10^{-6}	5.64×10^{-5}

4.1. *Cross-Calibration and Cosmic Background*

One important objective of instrumental calibration procedures is to enable stable, robust and consistent estimates of physical parameters. Comparisons of results for calibration standards such as the IACHEC group's work on the supernova remnant 1E 0102.2-7219 (Plucinsky et al. 2017), show that different instruments usually agree to within a few percent with some energy dependence. Similar considerations apply to measurements of WR 140.

We found that there were flux offsets between observations from different instruments for observations which overlap in phase and in time. In addition to the cross-calibration uncertainties, flux offsets arise because of the different amount of cosmic X-ray background (diffuse X-ray background along with other possible cosmic sources) included in the non-imaging observations by *RXTE*, *NICER*, and *Swift* in WT mode, since all these instruments have different fields-of-view in addition to different sensitivities. The imaging *Swift* PC-mode data allow the most accurate account for cosmic background since background is directly determined from source-free regions of the PC image. We therefore corrected the *RXTE*, *NICER* and *Swift* WT mode fluxes to the PC fluxes. We found that we needed to subtract an additional background flux of 0.50×10^{-11} ergs cm^{-2} s^{-1} from the *RXTE* 2–10 keV band fluxes, and 0.70×10^{-11} ergs cm^{-2} s^{-1} from the *NICER* fluxes, and 0.80×10^{-11} ergs cm^{-2} s^{-1} from the *Swift* WT mode data to bring them into agreement with the *Swift* PC-mode data. In addition, we needed to divide the background-corrected *RXTE* fluxes by a scale factor of 1.35 to match the *Swift* PC-mode data in order to bring the amplitude of variation of the *RXTE* data into agreement with the *Swift* PC-mode data in the regions near X-ray maximum.

4.2. *X-ray Flux Variations in the 2–10 keV Band*

In what follows, times and phases are calculated using the following ephemeris:

$$T_o(JD) = 2454846.7270 + 2895.00E$$

where E is the cycle count, the period is given by T21, and the epoch T_o (2454846.7270 = 2009-01-15 05:26:52 UTC) corresponds to the time of periastron passage from T21, but 2 orbital cycles earlier. We adopt this value of T_o since this periastron passage was densely monitored by both *RXTE* and *Swift*.

Figure 2 shows the complete *RXTE*, *Swift*, and *NICER* 2–10 keV band X-ray flux curve of WR 140 covering three periastron passages. The general characteristic of WR 140's X-ray flux curve is a gradual increase in X-ray brightness as the stars approach periastron, followed by a rapid decline to a brief, sharp minimum, a quick recovery from the minimum, and a gradual decline in brightness up to apastron. While this is similar to the X-ray variation seen in WR 140's "sister star", η Car[6] , another long-period, highly eccentric colliding wind binary, it is worth noting that, unlike η Car, there are no strong, rapid ($\sim$weeks) X-ray variations ("flaring", Moffat & Corcoran 2009) of the X-ray brightness seen in WR 140 just prior to the start of its X-ray minimum. As shown in Figures 2 and 3, the X-ray fluxes from the two orbits observed by *RXTE* agree very well with each other at all common phases. In addition the depth and duration of WR 140's X-ray minima are nearly constant from one orbital cycle to another. This can also be contrasted with η Car which shows significant changes in the duration of X-ray minimum from cycle to cycle (Corcoran et al. 2010, 2017).

If the cooling of the shocked gas is effectively adiabatic and wind absorption is minimal, the luminosity of X-ray flux with phase is expected to vary inversely with D, the separation between the two stars (Usov 1992; Stevens et al. 1992). In the figures the gray dashed curve represents a $1/D$ variation and it is clear that near X-ray maximum & minimum the X-ray brightness curve does not follow the expected $1/D$ variation. As can be seen more clearly in Figure 3, the deviation from the $1/D$ dependence in the X-ray flux starts about 120 days prior to periastron passage, i.e. around the time of superior conjunction of the WC star.

Figure 4 shows the *Swift* X-ray fluxes in the 2–10 keV band around the 2016 minimum, along with *NICER* 2–10 keV band fluxes. *NICER* began observations in July 2017, so that observations started after periastron passage ($\phi = 2.1$). There is good agreement between the *Swift* and *NICER* contemporaneous fluxes. As shown in Figure 2 and in Figure 4, the *NICER* fluxes seem to be about 10% below the projected level of the *RXTE* fluxes at these phases (but in good agreement with the *Swift* fluxes in the area of overlap).

The exceptional X-ray brightness of WR 140 enables accurate assessment of its variability. Even the first few isolated observations of WR 140 with *EXOSAT*, *ROSAT*, and *ASCA* showed that variability was an obvious feature

---

[6] An interesting numerological coincidence between these sister binaries: in 2009 WR 140 reached its X-ray minimum on 24 January 2009, just 8 days after η Car began its own X-ray "deep minimum" phase (on 16 January 2009) near its periastron passage. This coincidence will not happen again for another 400 years. The next time the X-ray minima will be similarly coincident will be in 2413 CE, when η Car's minimum will occur on 29 July, just three days before WR 140's own X-ray minimum on 1 August.
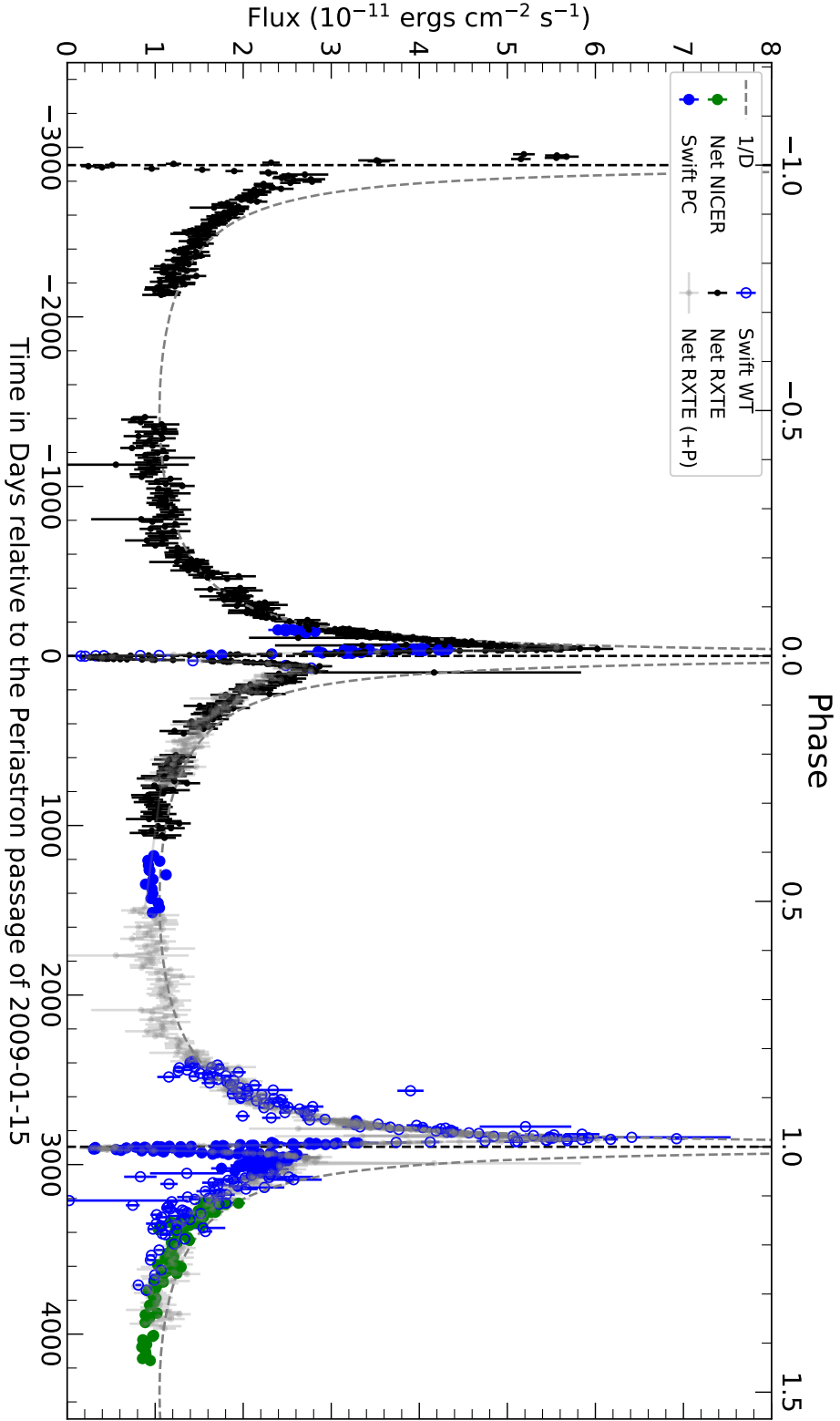
Figure 2. The *RXTE*, *Swift*, and *NICER* lightcurve of WR 140, 2000-2020. The time zero point corresponds to the periastron passage JD 2454846.727 = 2009-01-15 05:26. The gray points are the RXTE fluxes advanced by one period. The black dashed vertical lines are times of periastron passages, while the gray dashed curves show the expected $1/D$ variation in flux for an unobscured adiabatic system of colliding winds.
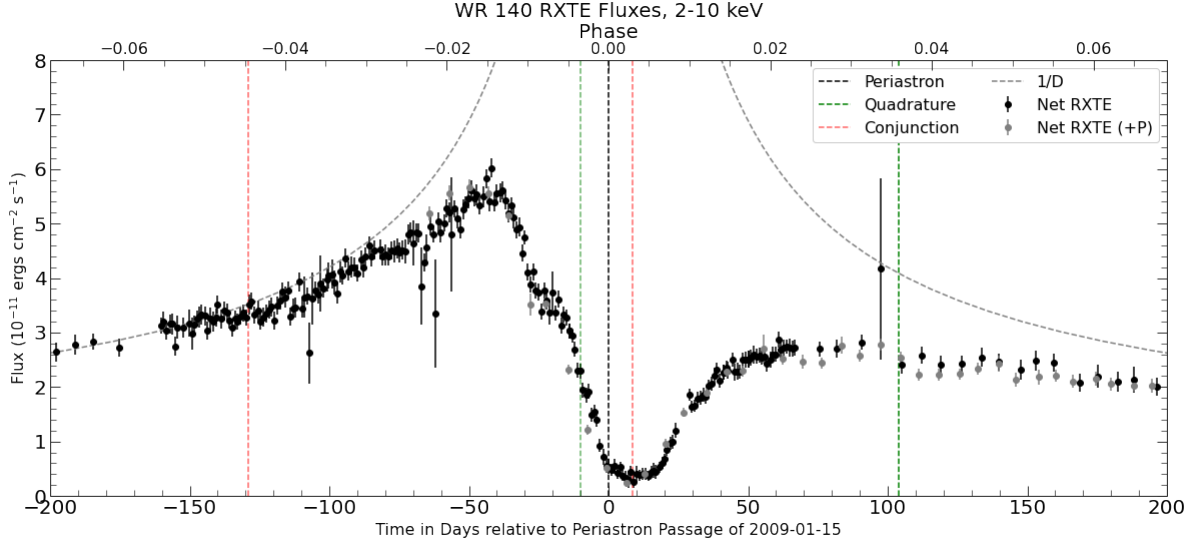
Figure 3. Comparison of the two minima observed by *RXTE* in 2001 (gray circles) and 2009 (black circles). Also shown are the timings of quadratures and conjunctions, with periastron passage in black. WC-star inferior conjunction occurs very close in time to the minimum of the X-ray flux a significant fraction of which is due to the cosmic X-ray background. The gray dashed curve shows a model flux inversely proportional to the stellar separation (D).
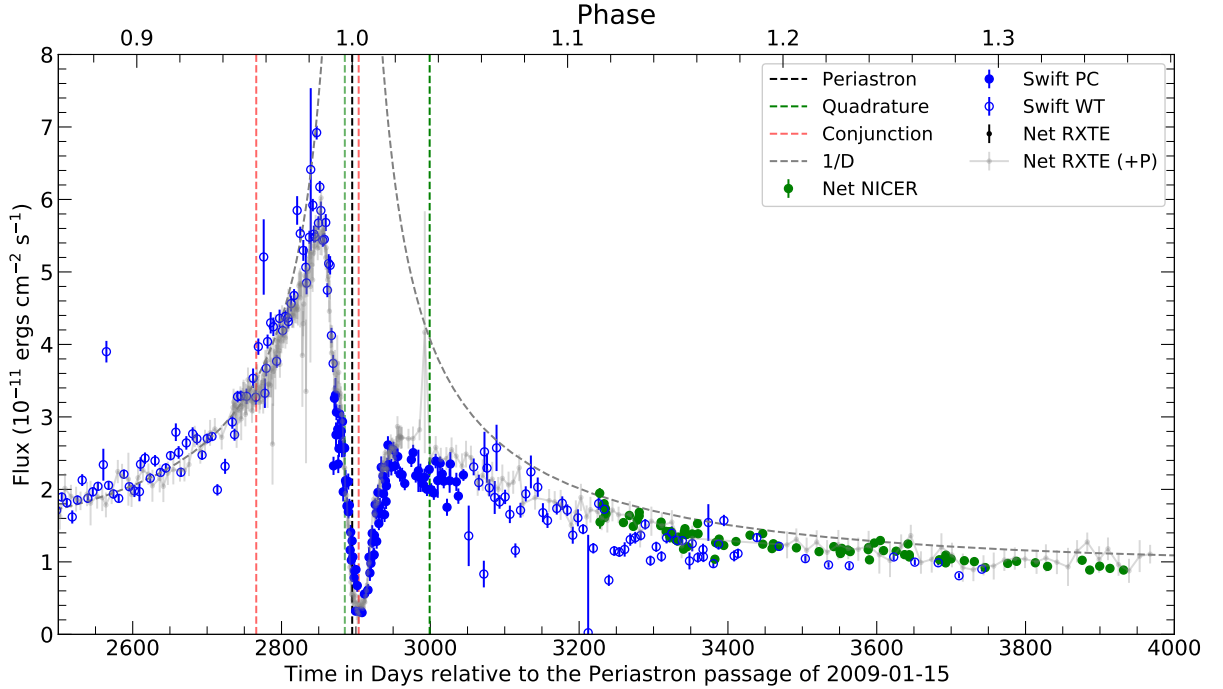
Figure 4. Comparison of *NICER* and *Swift* contemporanous 2–10 keV X-ray fluxes around the 2016 minimum. *RXTE* fluxes from the 2009 minimum are also shown. *Swift* PC-mode data are shown as filled blue circles, while WT-mode data are shown as open blue circles.

of its behaviour in line with broad expectations of the eccentric binary colliding-wind model. The detailed monitoring built up since over the last two decades through nearly a thousand separate observations with *RXTE*, *Swift*, and *NICER*

allows a fairly complete picture to be drawn of the phase-dependent balance between downstream shock emission from the interacting winds and upstream foreground absorption during transfer principally through the more powerful wind of the WC star. As the ensemble of data under consideration here shows no evidence of changes in the equivalent temperature structure of the emission, discussion may properly be framed in terms of the independent measures of luminosity and absorption of the X-ray emission with reference where necessary to where this simple scheme fails, notably at low energies near periastron.

The X-ray observations also show that the X-ray spectrum of WR 140 is repeatable at all phases between orbital cycles in both emission and absorption and varies smoothly and monotonically between a few turning points that emerge due to boundary conditions of macroscopic orbital dynamics or microscopic X-ray emission physics. Of particular note is the absence of flares or other short-term episodes. Instances of apparent rapid variability between individual exposures visible in some of the figures are invariably due to instrumental instabilities. These ideas will be subject to stricter test in work underway on the ensemble of the few dozen X-ray observations of WR 140 of much higher statistical weight at scattered phases made with other instruments.

4.3. *Orbital Dependence of WR 140's X-ray Luminosity*

As shown chronologically for the different instruments in Figure 5 and in folded form near periastron in Figure 6, the intrinsic X-ray luminosity of WR 140 evolves smoothly as a function of binary phase. At apastron, when the binary system is at its maximum separation, the X-ray luminosity is a minimum. During the subsequent long, nearly 4-year approach to periastron, covered in its entirety from 2005 March by *RXTE*, the luminosity gradually increases in inverse proportion to the binary separation until about 6 months before periastron when it has doubled, behaviour confirmed in its later stages by the long-term *Swift* campaign initiated 16 months before the next periastron passage in 2016 December. After this point, the luminosity continues its steadily accelerating increase, though now slower than expected from the inverse binary separation, until reaching a maximum, not at periastron, but about 20 days beforehand after which a rapid decrease occurs by about a factor of five over about 20 days. This unexpected decrease corresponds closely, as shown below, with the complementary increase of excess emission in the C III $\lambda 5696$ optical emission line in WR 140 (Fahed et al. 2011).

Spectral properties close to the X-ray minimum have been relatively hard to establish for a combination of reasons: the observed count rates are lowered even further than just the decreasing luminosity by heavy and changing absorption during the transit of the WC star; the unresolved *RXTE* background becomes much more significant; and the appearance of the relic component. Despite these challenges, it is clear the minimum is relatively flat for 10-15 days near periastron and conjunction before recovery gets underway. Furthermore, in common with the rest of the X-ray orbit, there is little evidence of the type of secular changes seen during repeated observations of η Car's X-ray minimum.

Despite fewer observations and the higher absorption described below, the recovery after periastron generally mirrors its previous evolution with some asymmetry as the luminosity appears to reach its local maximum perhaps 10 days later than expected from its counterpart before periastron. A few weeks later, symmetry in luminosity seems to have been established with good agreement between the three instruments during a steady decrease towards apastron inversely proportional to the binary separation.

4.4. *Orbital dependence of WR 140's X-ray absorption*

As shown in Figure 7 on a logarithmic column-density scale, the variable X-ray absorption observed in WR 140 has a complex structure of high dynamic range that is asymmetric with orbital phase. Agreement is good between measurements by *RXTE* and *Swift* near the periastron passages of 2009 and 2016, indicating that the wind absorption stayed repeatable with orbital phase over at least the last two orbital cycles. *NICER* and *Swift* also agree well at common phases.

The variations in column density are consistent with general expectations of the colliding-wind shock model in which the upstream O-star wind is confined by the more powerful WC-star wind within a cone-shaped boundary having a half-opening angle relative to the line of centers of $\theta_S \approx 32° - 41°$ according to the rough radiative and adiabatic estimates in Table 1. The X-ray emission occurs in the intervening interaction region that forms an extensive interface between the two upstream winds of dimension comparable with the binary separation. The carbon-rich WC-star wind is responsible for most of the absorption around the orbit, shown by the maximum within a few days of WC-star inferior conjunction when the WC-star is in front of the system's center-of-mass, the stagnation point and its stellar
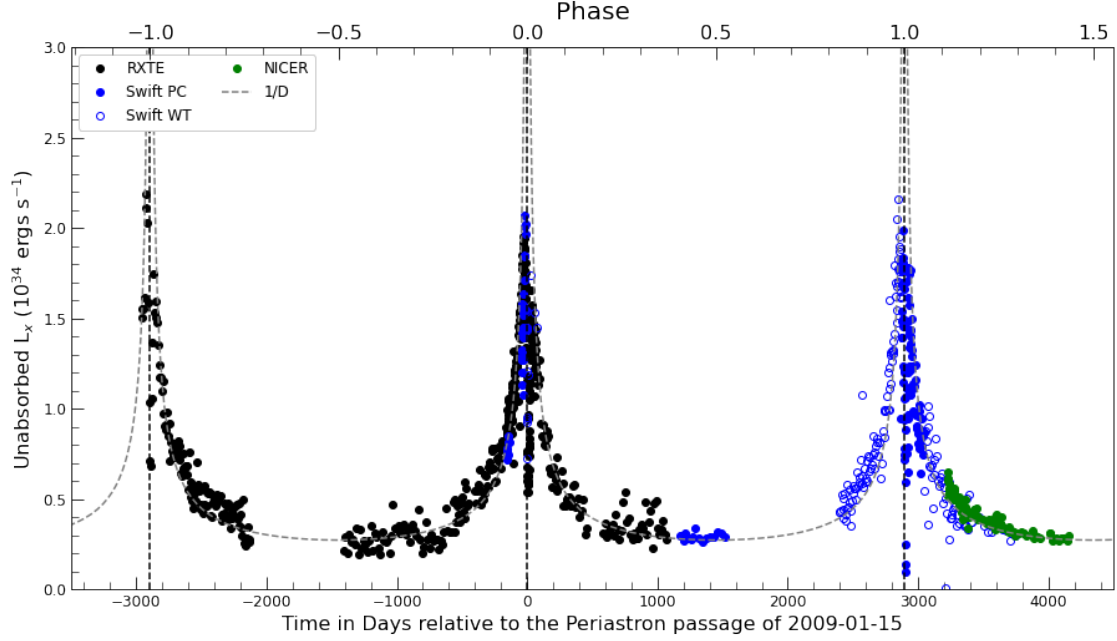
Figure 5. X-ray luminosity in the 2–10 keV band corrected for interstellar and circumstellar absorption assuming the distance in Table 1. The dashed line shows a $1/D$ variation.
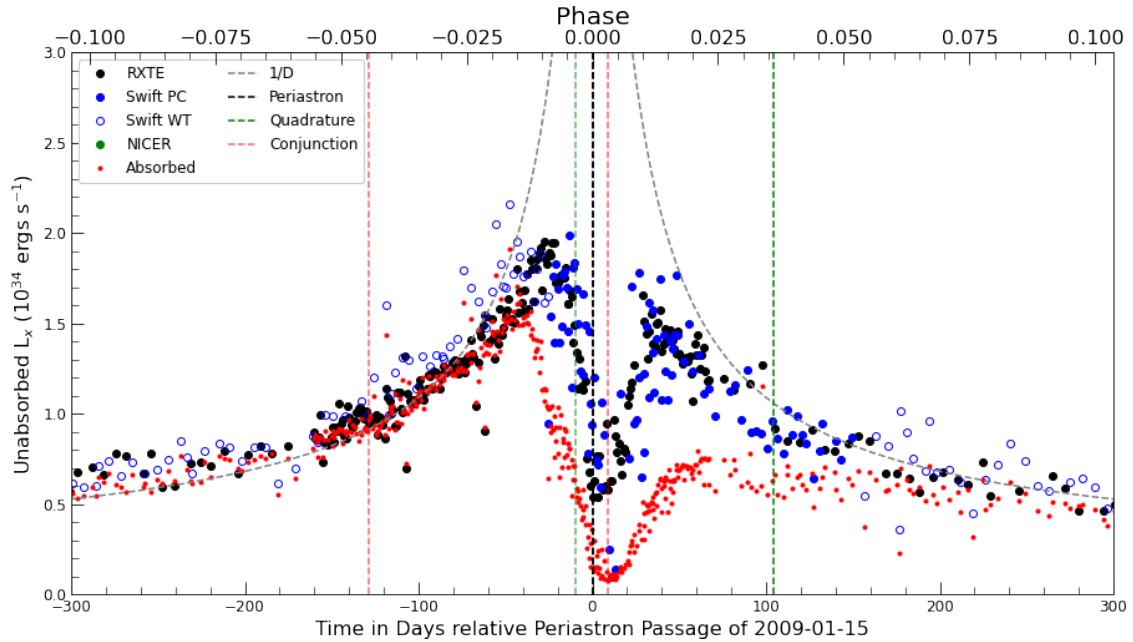
Figure 6. X-ray luminosity in the 2–10 keV band corrected for absorption in the interval 300 days around periastron passage. The red points show the observed (i.e. absorbed) luminosity from the *RXTE* and *Swift* observations.
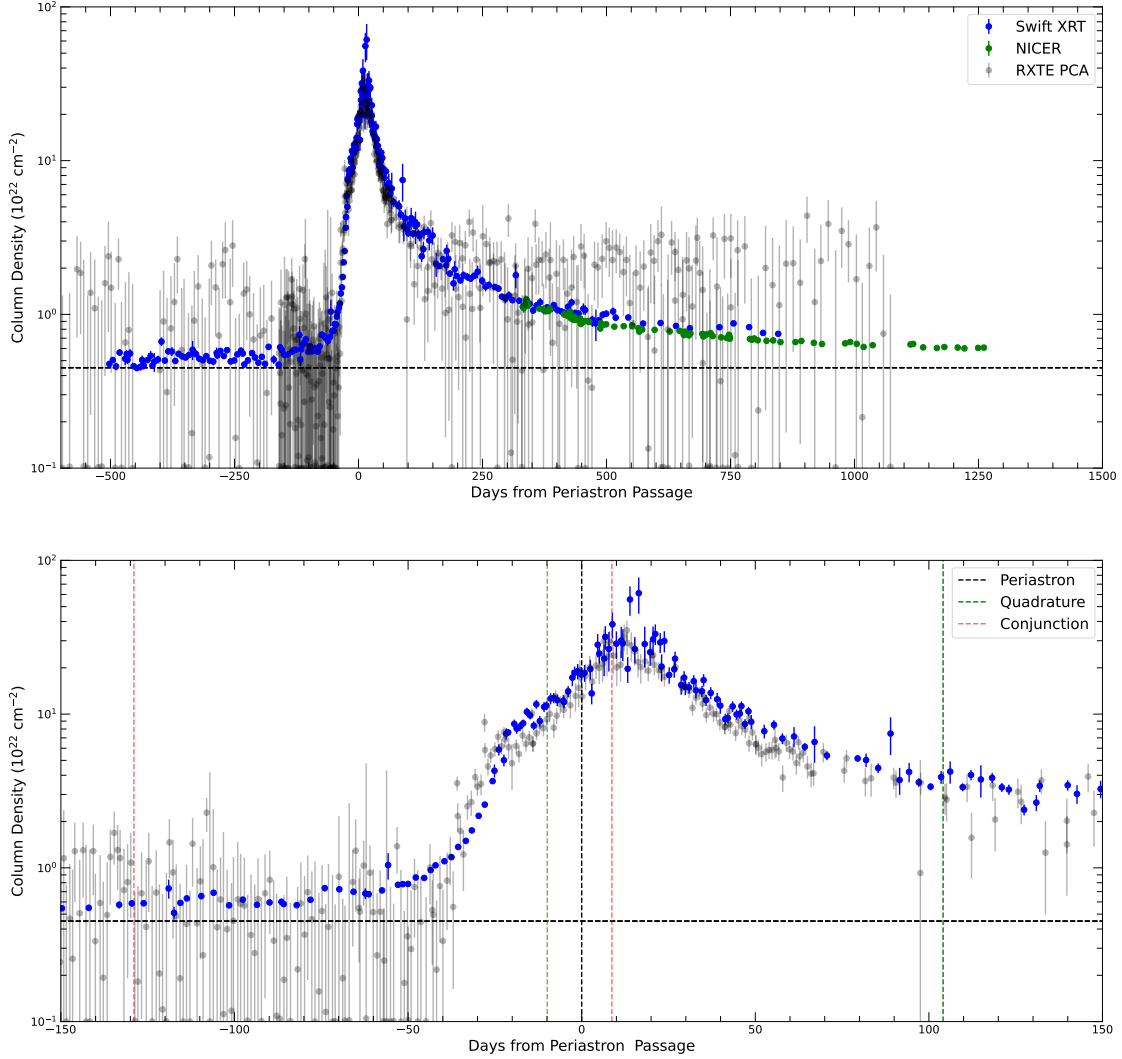
Figure 7. *Top*: Column density variations from best fits to *RXTE*, *Swift* and *NICER* spectra. A horizontal dashed blue line shows the column density far from periastron, i.e. $N_H = 4.6 \times 10^{21}$ cm^{-2}, which represents the interstellar column to the system without additional wind absorption. *Bottom*: Same as above emphasizing the 300 day interval around periastron passage. Red, green and black vertical lines mark times of conjunctions, quadratures and periastron passage, respectively.

companion. The high eccentricity and the longitude of periastron ω determine that the WC star is nearer the observer for only about 138 days including periastron, while the O star is in front for the remaining 2757 days, including apastron.

Significant absorption path lengths through the wind of the O star occur near its inferior conjunction for orbital inclinations $\sin i > \cos \theta_S$, i.e., $i > 58°$. For WR 140, although Table 1 suggests that $\sin i \approx \cos \theta_S$, the obvious transition in the column density measurements over the short interval between the two conjunctions shows that the

winds of both stars are involved, allowing among other things estimates to be made below of the system geometry. Other slower variations with orbital phase are partly due to changing absorption path lengths through the two winds.

A basis of the hydrodynamic models often used for simulations of colliding-wind systems is the absence of any information to the flow of upstream gas that would signal the presence of shocks further downstream. In this case, foreground absorption is identical to that of single stars, allowing the construction of simple geometrical models. The column density integrated along a path entirely through the terminal velocity flow of a wind from a point $\vec{R}_x$ to a distant observer takes the concise form

$$N_x \ \mathrm{cm}^{-2} = 4.31 \times 10^{23} \frac{\dot{M}_{-6}}{\mu v_8} \frac{\Theta}{b} + N_{\mathrm{ISM}} \tag{1}$$

where $\dot{M}_{-6} \times 10^{-6}$ $\mathrm{M}_\odot$ yr^{-1} is the mass-loss rate; μ is the mean atomic weight; $v_8 \times 1000$ km s^{-1} is the wind terminal velocity; Θ radians is the aspect angle between the vector joining the stars and the line-of-sight; $b = R_x \sin \Theta \ R_\odot$ is the impact parameter; and N_{ISM} is the constant interstellar term. In WR 140, the geometrical terms are accurately defined by the well-constrained orbit.

Although the X-ray source is likely to be comparable in size to the binary separation, for simplicity we have calculated indicative column densities along single lines-of-sight from the stagnation point as a function of phase. The single-point approximation provided good fits to all the data considered here and has been widely used in the literature for the analysis of colliding-wind systems. Its use is justified by examples that we have calculated of X-ray sources extended along the analytical shell interface of Canto et al. (1996). More sophisticated approximations are likely to require detailed dynamical simulations. For example, in order to anticipate the type of work that will be required and to illustrate for present purposes the system geometry at significant phases in the column density curve from the beginning of the *Swift* campaign, Figure 8 shows density distributions in the orbital plane of WR 140 from 3-D smoothed-particle hydrodynamics simulations (Russell et al. 2013) based on the parameters in Table 1.
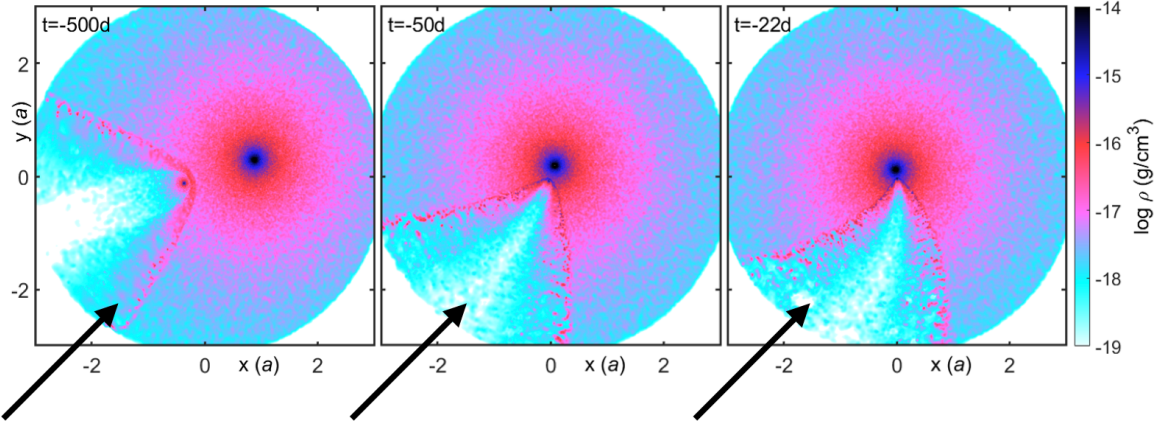
Figure 8. Simulated density distributions of WR 140 in the orbital plane at 500 days (left), 50 days (middle) and 22 days before periastron passage from a dynamic 3-D smoothed-particle hydrodynamics fluid model (2021, C. Russell et al., in prep.). The arrow represents the observer's line-of-sight projected onto the orbital plane with the spatial scale in units of the semi-major axis, a. The half-opening angle of the shock cone in this simulation is about 40°. At −500 days the leading edge of the shock cone around the O star has recently crossed the observer's line-of-sight. The shock cone takes about 450 days to pass the line-of-sight. Between −50 and −22 days, the trailing edge of the shock cone passes the line-of-sight which shortly afterwards encounters the dense unshocked wind of the WC7 star, causing a rapid increase in column density as the stagnation point of the shock passes close to and behind the WC7 star.

4.4.1. *Absorption by the O-star wind*

While maximum absorption close to WC-star conjunction was already evident from the earliest observations with *RXTE*, the orbital dependence at the lowest columns has only been revealed with the soft X-ray capabilities of the *Swift* XRT campaign that began in 2015 August, about a year and a half before the most recent periastron. In the observations from the beginning of the campaign in the approach to O-star conjunction 129 days before periastron and beyond, the observed column increased slowly but steadily by about 20% over the course of a year or more until 50 or

60 days before periastron, when a rapid increase in column began. As shown in Figure 9, when the shocks around the O star are directed towards the observer and the WC7-star wind makes its smallest contribution, this lowest part of the absorption curve observed so far between 500 and 80 days before periastron is well modelled by a combination of a constant component due to the interstellar medium and a term linear in Θ/b following Eq. (1) for the O star. With this model, the estimate of the constant interstellar term is $(4.64 \pm 0.07) \times 10^{21}$ cm^{-2}, consistent with the interstellar column in the direction of WR 140 derived from WR 140's colour excess or Lyα absorption. For $\mu_{O5} = 1.30$, the linear term yields an O-star mass-loss rate of $\dot{M}_{O5} = (3.7 \pm 0.3) \times 10^{-7}$ M$_\odot$ yr^{-1}, about half the smooth-wind value adopted in Table 1, which was the lowest among several alternatives discussed by Pittard & Dougherty (2006).
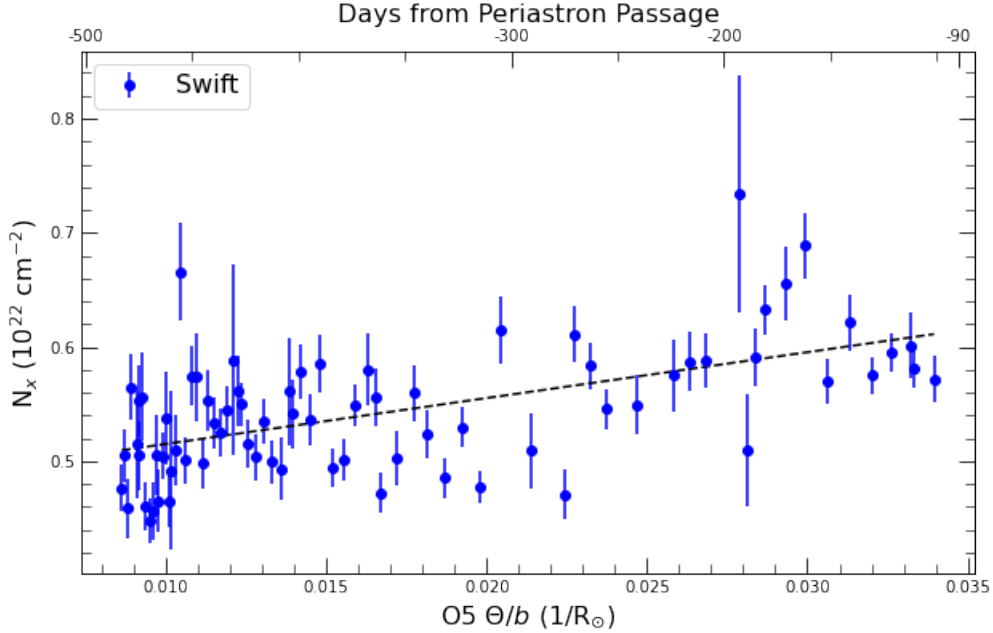
Figure 9. X-ray absorption column density observed in WR 140 with the *Swift* XRT as a function of the column-density integral through the O-star wind given by ratio of the aspect angle (Θ) to impact parameter b in the range 500-80 days before periastron passage. The dashed line is the linear fit to the data, $(3.956 \times \Theta/b + 0.464) \times 10^{22}$ cm^{-2}.

4.4.2. *Transition between O-star and WC-star winds*

An interesting and perhaps unexpected feature revealed by both the measurements and the simple model of this highly eccentric binary is that the conjunction of the O star does not coincide with an absorption maximum. Instead, as a result of the rapidly decreasing binary separation, the absorption maximum would have been reached about 100 days later, a month or so before periastron, if other events did not intervene.

The extended episode of low absorption ends between O-star conjunction and quadrature with a rapid increase in column density of more than an order of magnitude in a month as the line-of-sight passes from the O-star wind into the WC-star wind, presumably via an intermediate direct view of shocked gas as the line of sight encounters the wall of the shock cone. The transition begins slowly about 60 days before periastron before increasing rapidly until an inflection point 22 days before periastron when the line-of-sight starts to pass predominantly through the WC-star wind. These phases mark the angular positions with respect to the system axis of the two shock discontinuities corresponding to aspect angles of 34.6° at the inner O-star shock and 61.2° at the outer WC-star shock. A contact discontinuity, whose existence might be doubtful in a collisionless plasma, would be located at some intermediate value. In any case, this estimate of the angular extent of the shock is within a few degrees of the theoretical values given in Table 1. It agrees well with the estimate of 34°±1° for the angle of the contact discontinuity inside the shock[s] derived from He I λ10830 absorption (Williams et al. 2021) and is reproduced with reasonable success by the fluid simulations shown in Figure 8.

4.4.3. *Absorption by the WC-star wind*
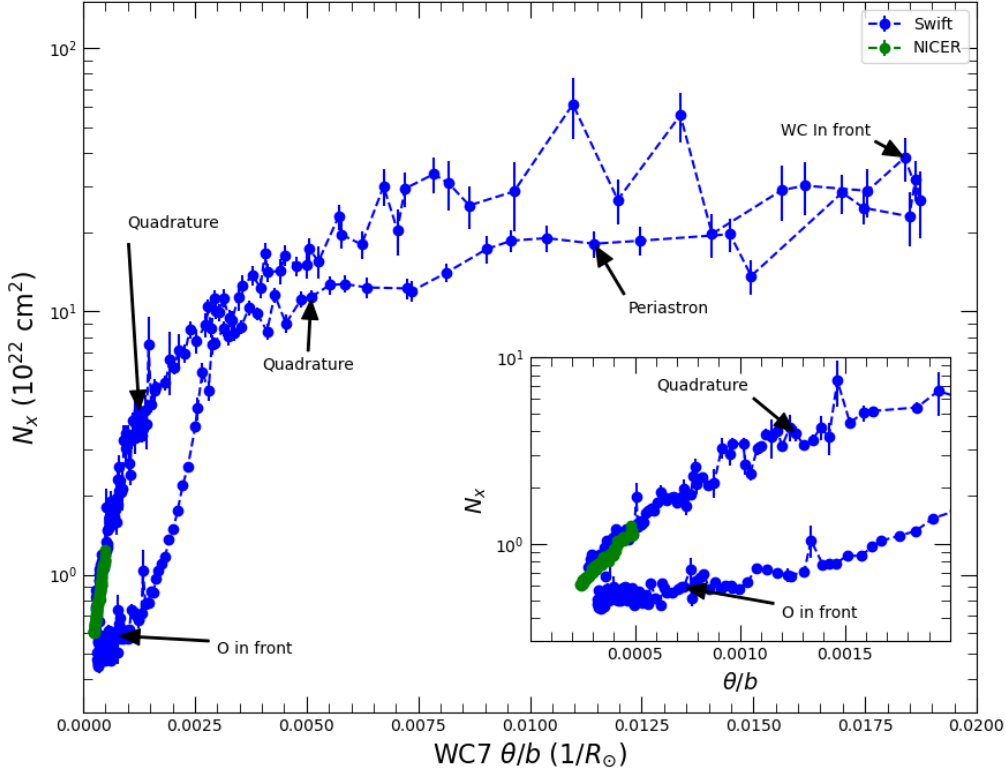
Figure 10. X-ray absorption column density observed in WR 140 with *Swift* and *NICER* as a function of the column-density integral through the WC-star wind at all available phases including those associated with the O star shown in Figure 9.

Once the WC-star wind intervenes, absorption becomes much stronger due to the appearance of material enriched in carbon and oxygen and a higher mass-loss rate which combine easily to outweigh the greater distance of the shock from the Wolf-Rayet star. It should be borne in mind that in order to make a fair comparison of absorption at all orbital phases, the same solar abundance photoelectric model has been used throughout and any mass-loss rate estimates need to take this into account. When the 30–40 day transition is over, the column density continues to increase for another 30 days at a slower but more regular pace through quadrature and periastron to reach a maximum close to WC-star inferior conjunction. At this point, for absorbing material of Table 3 emission abundances with $\mu_{WC7} = 5.73$ and correspondingly higher photoelectric cross-sections, the implied mass-loss rate is $\dot{M}_{WC7} = 1.7 \times 10^{-5}$ M$_\odot$ yr^{-1}, a factor of 3 smaller than the value given in Table 1.

The post-periastron orbital dynamics are slow in comparison so that the aspect angle of 61.2° marking the WC-star shock encountered 22 days before periastron is reached only 654 days afterwards at much greater orbital separation. The binary dynamics of this highly eccentric system are therefore the major cause of the comparatively slow decrease in absorption over years after WC-star conjunction compared with the rapid evolution over a month before. However, in contrast to the absorption through the O-star wind, the same type of simple linear geometrical model has no success reproducing the higher, longer-lived WC-star absorption. Instead, the absorption follows the distinctive locus in the $N_x - \Theta/b$ plane shown in Figure 10 that was constructed from all the available column density measurements made with *Swift* and *NICER* from 502 days before periastron to 1261 days after. This amounts to 61% of the orbit where the stars are moving at their slowest leading to the expectation that the small unexplored part of the locus at the lowest column densities will take just over 3 years to complete and probably close.

The locus consists of two loops: an upper, rapid, roughly horizontal loop associated with the WC-star wind and high column densities that lasts about 70 days when the stars are moving at their greatest orbital velocities; and a lower,

slower, roughly vertical loop associated with the O-star wind and lower column densities that otherwise occupies nearly the whole orbit. The locations of periastron, conjunctions and quadrature are marked. The two loops coincide close to the inflection point that marks the end of the rapidly ascending transition between the winds of the O star and WC star. Once the highest values have built up relatively slowly towards WC-star conjunction, the column density stays roughly constant for nearly three weeks despite a large reduction in Θ/b. This behaviour strongly suggests the presence of a large amount of absorbing material not connected with the line-of-sight through the undisturbed upstream wind but instead with the shock itself. This matter is discussed further below where we suggest that reflected ions are responsible.

4.4.4. *Transition between WC-star and O-star winds*

The rapid transition between O-star wind and WC-star wind intervening in the lines-of-sight to the X-ray source observed a few weeks before periastron through the sharp increase in column density over a month must have a counterpart in the opposite direction after periastron in which the lines-of-sight move from WC-star wind to O-star wind. Neglecting the curvature of the shock fronts, it is plausible that this could take place roughly near the corresponding orientations between aspect angles 61.2° and 34.6°. If so, it would involve a slowly decreasing column density starting 654 days after periastron and lasting for more than half the entire orbit over years rather than weeks. The observations taken so far are consistent with this idea with the latest *NICER* measurements showing gradually falling column densities to values still significantly greater than the lowest values seen at the beginning of the *Swift* campaign. This trend should continue through apastron and require precise measurements to follow its progress for the next few years and complete the loop which might include a shallow local minimum a few months after the binary separation starts to decrease again.

4.5. *The "Relic" Component*

Analysis of *Suzaku* X-ray spectra during the X-ray minimum associated with the 2009 periastron passage by Sugawara et al. (2015) uncovered a soft component below about 2 keV, which they suggested was a relic of cooling plasma from the wind collision. This "relic" component was seen in spectra obtained on 2009-01-04 and 2009-01-13, at orbital phases of -0.004 and 0.001, respectively. The relic component seems similar to residual soft emission revealed in other systems at orbital phases when the colliding-wind emission suffers severe photoelectric absorption: relevant examples include γ^2 Velorum (Hartman et al. 2004), the brightest Wolf-Rayet star in the sky and also a WC+O binary system; and η Car (Hamaguchi et al. 2007) where a so-called "Central Constant Emission" component emerges at its deep X-ray minimum.

Figure 11 shows a well-exposed *XMM-Newton* EPIC-pn X-ray spectrum of WR 140 taken two days before maximum X-ray absorption at the inferior conjunction of the WC7 star. It was retrieved from the *XMM-Newton* Science Archive[7] under ObsID 0790850201. It shows clear distinction between the hard colliding-wind emission in which the line emission from Fe XXV remains prominent above the highly absorbed continuum, and the soft relic component. The relic is composed of narrow features that are resolved even with the limited spectral capabilities of the EPIC-pn instrument and whose energies are well-determined enough to enable the identifications suggested in Figure 11 following Sugawara et al. (2015).

The *Swift* monitoring observations around the 2016 periastron passage provide a measure of the appearance of this component and its temporal behavior once account is taken of the effects of PC-mode optical loading. The *XMM-Newton* data shown in Figure 11 do not suffer from this effect. The XRT was switched to PC mode once the count rate had fallen sufficiently as WR 140 approached its minimum for pile-up no longer to be significant, since PC-mode provided a directly-determined background estimate, important when the X-ray source was faint. Initial inspection of the lowest-energy data then showed erratic variability which proved to be confined to multiple-pixel (as opposed to single-pixel) X-ray events as classified by event grade. Event grade is assigned early during data processing to show the number and pattern of neighboring detector pixels contributing to the recognition and reconstruction of an individual X-ray photon. Single pixel events are classified as grade 0 while multiples are doubles with grades 1-4; triples with grades 5-8; or quadruples with grades 9-12. Composite spectra for doubles, triples and quadruples accumulated during the minimum showed the narrow low-energy peaks at 2, 3 and 4 times the event threshold, respectively, characteristic

---

[7] http://nxsa.esac.esa.int/nxsa-web/
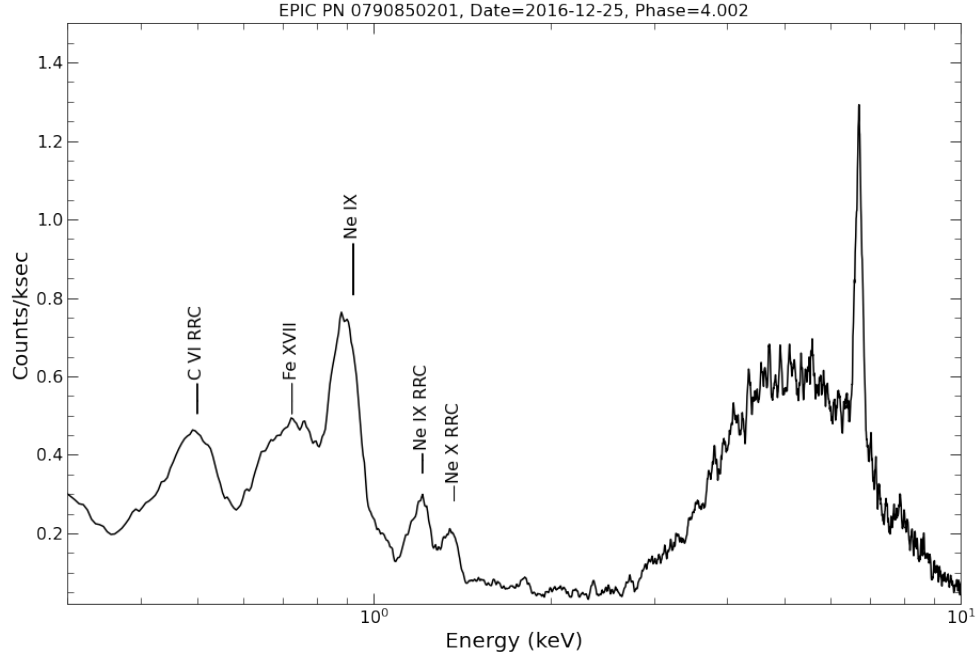
Figure 11. *XMM-Newton* EPIC-pn energy spectrum of WR 140 observed about a week after periastron passage in 2016 showing most clearly the relic component emission below 2 keV and suggested identifications for some of its narrow features displayed on a logarithmic scale in energy.
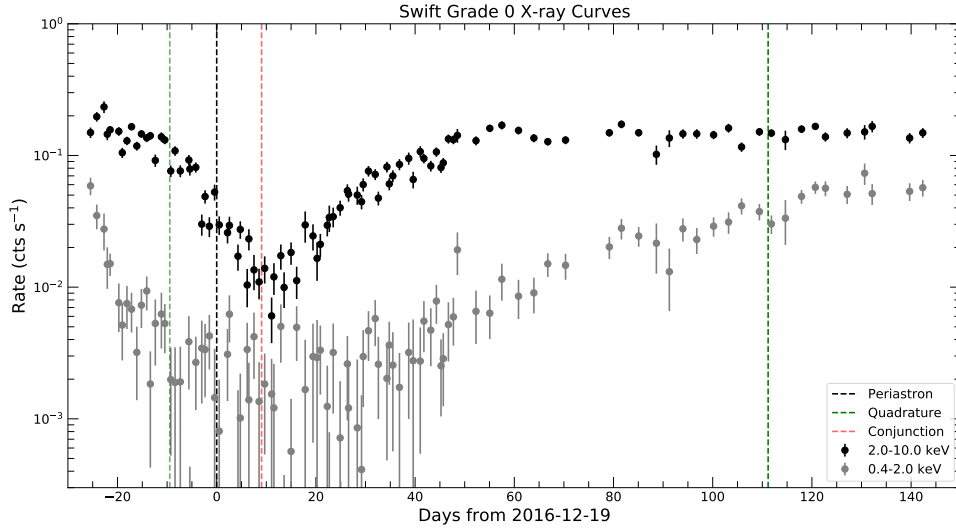
Figure 12. The X-ray count rate in the relic band (0.4 – 2.0 keV) from *Swift* XRT observations including only grade 0 events above 0.4 keV, compared to the 2 – 10 keV colliding wind emission from the grade 0 events. The relic component is visible from 25 days before periastron passage to about 50 days afterwards, during times of high absorption. The XMM-Newton spectrum in Figure 11 was taken close to conjuction

of optical loading affecting optically bright targets in tailored calibration work. Single grade 0 events with energies below 0.4 keV were excluded for the same reason.

Figure 12 shows the variations of the grade-0 selected count rates in soft ($0.4 < E < 2.0$ keV) and hard ($2.0 < E < 10.0$ keV) bands as a function of phase near periastron passage and WR conjunction a few days later. The soft band includes the relic component while the hard band is dominated by the thermal emission from the colliding wind shock. The relic component is revealed about $10 – 15$ days before periastron due to combination of increasing absorption and decreasing luminosity of the colliding-wind shocks, and is visible for about 50 days after periastron until absorption and luminosity have recovered for low-energy events again to be dominated by emission from the wind-wind collision. During the 50-d minimum, although the relic component is responsible for only a handful of counts in each observation, there is some statistical evidence for variability. The accumulated spectrum closely resembles that seen at occasional relevant phases during much longer observations with *CHANDRA*, *XMM-Newton*, and *Suzaku*.

5. THE C III λ5696 CONNECTION

As the stars in WR 140 approach and pass periastron, significant excess emission appears superimposed on the strong flat-topped C III λ5696 emission line characteristic of WC stars (Hervieux 1995; Marchenko et al. 2003; Fahed et al. 2011). The excess has complex and well-resolved velocity structure that moves rapidly from blue to red across the line as the intensity strengthens and fades through periastron and beyond. Similar excesses are also seen in C III λ5696 in other WC colliding-wind binaries (e.g., Hill et al. 2018) and in other lines in WR 140 such as He I λ10830 (Williams et al. 2021). It has been natural to suppose such optical and infrared excesses to originate some way downstream in the wind collision zone after shocked WC-star plasma has had time to cool to an appropriate temperature ($T \lesssim 10^5$ K) with the velocity profile formed in the continuously changing orientation of the shocked flow wrapping around the O star as the system revolves in its orbit.

However, three observational arguments suggest instead a closer connection between X-rays and C III λ5696 concerning, in turn, their correlated temporal behavior; the comparative luminosities; and the observed velocity profiles; all considered in the context of the succession of orbital events of quadrature, periastron and conjunction that occur so close together in WR 140's highly eccentric but accurately-defined orbit when shocked gas flows away on time scales $D/v_\infty \sim 1$ day or less. During this crucial part of the orbit, many things are changing rapidly at once on a daily basis with the sharp fall in intrinsic X-ray luminosity and sharp rise in absorption, combining to produce a steeply declining X-ray count rate as the strength of the C III λ5696 line increases before turning points throw the system into reverse.

5.1. *Anti-correlated variability of X-ray and C III λ5696*

Figure 13 compares the evolution of the equivalent widths of C III λ5696 during the 2009 periastron passage (from Table 7 in Fahed et al. 2011) with the 2–10 keV X-ray flux measured during that time by *RXTE*. This shows an exceptionally tight correlation between the observed drop in X-ray flux and the strengthening C III before periastron: formally, the Pearson correlation coefficient $= -0.963$ in the interval between 2008-12-18 and 2009-01-21. About 20 days before periastron, a step occurs in the X-ray decline mimicking closely a similarly subtly-shaped feature in the strengthening C III line. The lack of any apparent lag between the two morphologies coupled with the timing of the turning points of C III maximum and X-ray minimum close to periastron suggests a common central origin of both types of radiation.

5.2. *Luminosities of X-rays and C III λ5696*

We converted the C III λ5696 excess equivalent widths reported by Fahed et al. (2011) to luminosities to compare to the phase-dependent intrinsic X-ray luminosities and assess the relative importance of the X-ray and C III in the overall shock energy budget during the few weeks around periastron when the excess appears. For WR 140 values of $V = 6.85$ and $A_V = 2.01$ and the standard calibration of the V-magnitude intensity scale of $f_\lambda = 3.64 \times 10^{-9}$ erg cm^{-2} s^{-1} Å^{-1} at $V = 0$ gives a conversion factor of 1.16×10^{34} erg s^{-1} Å^{-1} for a distance of 1.52 kpc to WR 140. Figure 14 shows immediately the close complementary relationship between the X-ray and C III luminosities in which the central X-ray deficit seen in Figure 5 is almost exactly compensated by C III. The combined luminosity $L_{X+CIII} = L_X + L_{CIII}$ formed by these two components of the energy budget and derived by interpolation is also shown and closely resembles the ideal $1/D$ prediction of colliding-wind theory. The combined luminosity observed at periastron, where the C III λ5696 excess peaks, is $L_{X+C\ III} = 1.8 \pm 0.1 \times 10^{35}$ ergs s^{-1} and the X-ray luminosity observed at apastron, in the expected absence of a C III excess, is $L_X = 1 \times 10^{34}$ ergs s^{-1}. Their ratio, 18 ± 1, is consistent with the value of $(1 + e)/(1 - e) = 18.9$,
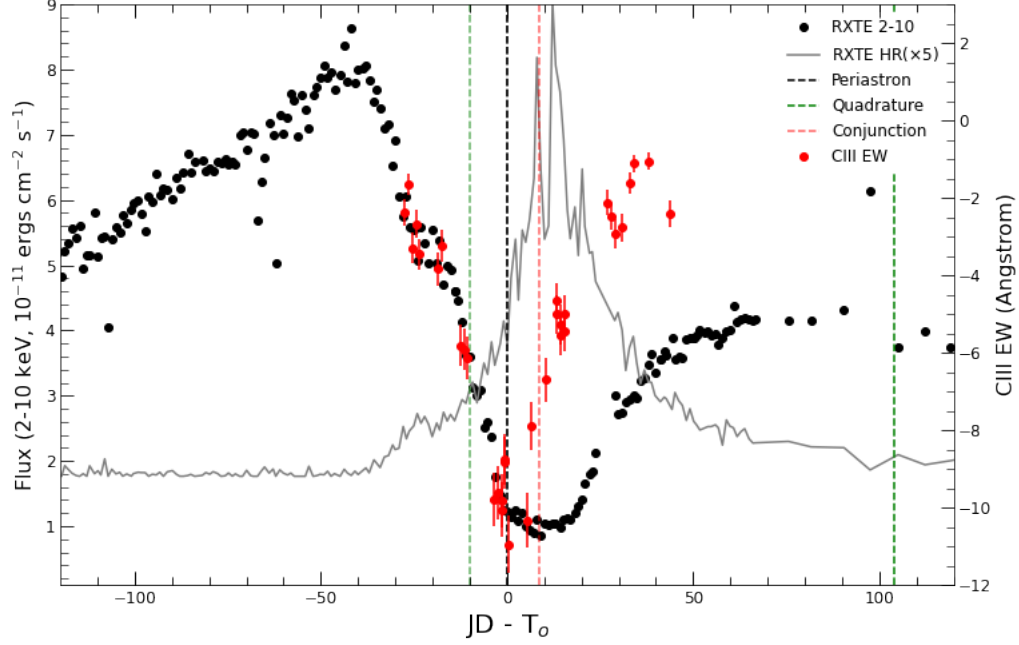
Figure 13. Comparison of the equivalent width of the C III $\lambda5696$ excess and the X-ray flux seen by *RXTE* during the 2009 periastron passage of WR 140. The asymmetry in the X-ray curve is mostly due to photoelectric absorption by the WC-star wind traced by the *RXTE* hardness ratio, HR.

where e is the orbital eccentricity, expected if the $1/D$ prediction applies around the entire orbit of WR 140. This is encouraging, though it should be borne in mind that the error given in the ratio, determined by the reported uncertainty in the C III equivalent width, is probably an underestimate due to unknown systematic errors that apply, for example, to the reddening correction.

5.3. *Velocity structure of the C III excess*

Information about the dynamics and location of the material radiating in the C III $\lambda5696$ line is available by considering, in addition to its intensity, the variable velocity profiles of the excess shown in Figure 3 and plotted in Figure 5 of Fahed et al. (2011). The observations illustrated there fall conveniently into separate groups according to orbital geometry. Before quadrature, when the WC star is behind its O-star companion, the excess, though faint in its early development, is nearly all confined as expected to negative velocities as the radiating material flows towards the observer. A week later, in a set of 3 observations more-or-less at quadrature, the excess is distributed roughly evenly between blue and red velocities. The maximum observed red shift is reached within perhaps 2 or 3 days of conjunction when the WC star is directly in front of its companion and shocked material is flowing away.

6. DISCUSSION

RXTE, *Swift*, and *NICER* X-ray monitoring observations of WR 140 have confirmed that its X-ray properties varied in a predictable way over the 4 orbital cycles between 2000 and 2020. They show that the shock conditions and radiation transfer vary repeatably as a function of orbital phase and therefore provide a rich and detailed set of measurements on which improved understanding of the underlying physics may be built. Appropriate 3D models combining orbital and gas dynamics with the physics of shock formation and dissipation are likely to be a challenging enterprise but whose boundary conditions are now more clearly defined by the results presented here concerning the cooling mechanisms of collisionless shocks under different conditions and the geometry of the interacting winds.
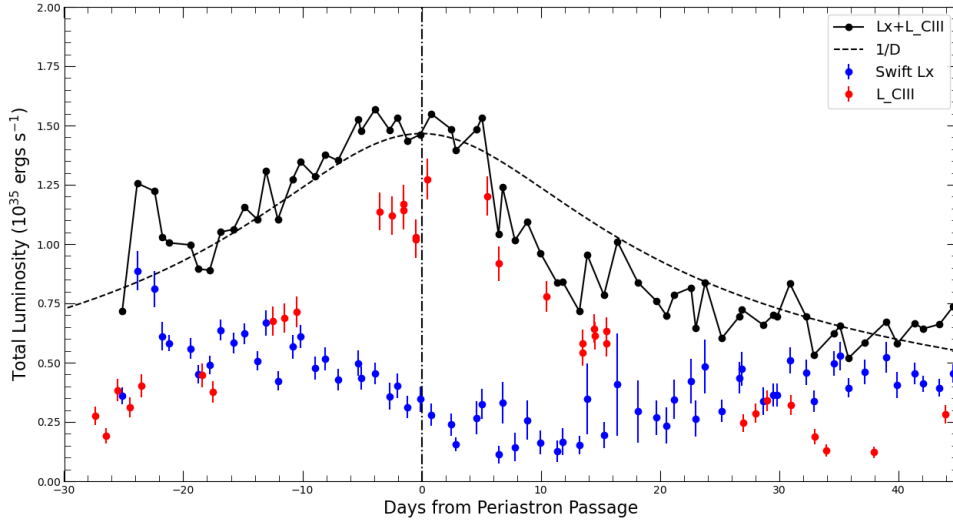
Figure 14. Comparison of the 0.5–10.0 X-ray luminosity and the luminosity of the C IIIline excess, both corrected for absorption, and the combined (Lx + C III) luminosity. The dashed line is a $1/D$ variation scaled by eye to the data.

With its uniquely well-determined 3D highly-eccentric orbit, WR 140 presents optimum opportunities for the study of its collisionless shocks in an astrophysical setting whose variable physical conditions of density, temperature, wind and orbital velocities and viewing angle remain under the simple control of gravity and orbital geometry.

The physical justification for classifying WR 140's shocks as collisionless (Pollock et al. 2005) and therefore regulated by collective electromagnetic processes as opposed to gas collisions rests on the long mean-free-paths for Coulomb collisions that pertain in the plasmas that constitute the winds of the hot stars. Conclusive supporting evidence for a collisionless classification comes from WR 140's status as a strong non-thermal synchrotron radio source (White & Becker 1995a). The relativistic electrons and magnetic fields required are both common properties of collisionless shock physics (e.g. Marcowith et al. 2016) that do not arise in the collisional regime.

6.1. *Magnetic Conditions in the Shocks of WR 140.*

Though Marcowith et al. (2016) argue that the background upstream magnetic field plays a pivotal role in the formation and dissipation of collisionless shocks, particle-in-cell simulations (Kato & Takabe 2008) show that the Weibel instability also operates in interacting unmagnetised plasmas to generate magnetic fields whose energy density amounts to 1% or 2% of the upstream bulk kinetic energy density. At the stagnation point in the terminal-velocity regime in that case

$$\frac{1}{8\pi}B^2 = W_B \frac{1}{2}\rho V\infty^2 \tag{2}$$

suggesting a shock-generated field of

$$B \approx 1141 \frac{1}{R_X}(W_B \dot{M}_{-6} V_8)^{\frac{1}{2}} G \tag{3}$$

where W_B is the fractional magnetic-field energy density and otherwise the units are those of equation (1) including R_X in solar radii. Shock-generated fields in initially unmagnetized media have been successfully reproduced in the laboratory (Huntington et al. 2017) and are an alternative to the common practice following Weber & Davis (1967) of extrapolating a stellar field into the wind, especially since strong surface fields are rare in O stars (Grunhut et al. 2017) and undetected so far in Wolf-Rayet stars (de la Chevrotière et al. 2014). At periastron, equation (3) implies a field of $0.05 - 0.1\ G$ at the stagnation point, and a shock dissipation scale length defined by the proton gyroradius of a few km. This field is about two orders of magnitude greater than those typically encountered in interplanetary space in front of the Earth's magnetosphere.

6.2. *Competitive Shock Cooling*

The combination of X-ray and C III λ5696 luminosities in the shock energy budget suggests that the ideal $1/D$ prediction of colliding-wind theory might still make reasonable sense for WR 140. If scalable geometry also applies, the O-star shock would lie only 36 $R_\odot$ from the center of the star at periastron, only a few radii above the stellar surface. The evident competition between X-ray and C III λ5696 cooling in such extreme conditions could conceivably be density or radiation dependent (Martins & Hillier 2012) if some other mechanism is excluded like charge exchange due to mixing between the two winds (Pollock 2012). However, when it is understood that lines at long wavelengths often classified as recombination lines can provide cooling under certain conditions to rival or surpass the X-ray luminosity, it will be necessary to consider other transitions such as He I λ5876 (Marchenko et al. 2003) and He I λ10830 for which Williams et al. (2021) have shown the importance of extensive phase coverage. Pending these assessments, it does not yet seem necessary to appeal to the suggestion of a variable effective mass-loss rate due to clumping effects (Zhekov 2021) to account for the unexpected decrease in WR 140's X-ray luminosity near periastron. Rather, the plasma has found another way to cool.

Future observations would be able to establish more firmly the nature of the cooling competition in at least three respects: first, more complete phase coverage including templates; second, simultaneous X-ray and optical line velocity profiles; and third, how close the C III emission peak is to the 2024 November 22 periastron in comparison with the 1-day flow time. These will all allow judgement of whether the rival cooling mechanisms compete on microscopic, as seems likely, or macroscopic scales.

In other WC+O binary systems of shorter period and smaller separation, WR 42, WR 48 and WR 79 (Hill et al. 2002) and WR 113 (Hill et al. 2018), the competition may have been decided in favour of C III λ5696 by their luminous excesses and weak or undetected X-ray luminosities.

6.3. *X-ray Absorption Tomography*

While the X-ray luminosity can be be considered almost an integrated thermodynamic state variable that responds to externally imposed conditions like an ideal astrophysical Carnot cycle, the observed absorption of the X-ray spectrum is sensitive to the morphology of whatever cold gas intervenes between source and observer. The model spectrum used to estimate the absorption as a function of phase simply incorporated a single line-of-sight column density to the stagnation point in the flow. This is adequate for the current campaign in which the scarce resource of observing time was shared between multiple observations to yield spectra of modest statistical weight at many different phases. The X-ray source is almost certainly extended on the scale of the binary separation. Though its detailed spatial form is not known, it is small enough for sharp features to appear in Figure 7 that delineate the morphology of the cool gas as the orbit rotates. Notably, the duration of the transition between O-star and WC-star winds implies that the post-shock gas occupies a significant angular size of 26° which Figure 8 suggests is due in about equal measure to the angular extent of the post-shock gas and the curvature of the shock front. As a consequence, the implication is that the shock has not suffered collapse at this point close to periastron from radiative losses.

The measurements made separately near both stellar conjunctions have enabled the estimates above of the mass-loss rates of both companion stars of $\dot{M}_{WC7} = 1.7 \times 10^{-5}$ M$_\odot$ yr^{-1} and $\dot{M}_{O5} = 3.7 \times 10^{-7}$ M$_\odot$ yr^{-1} implying a measured value of $\eta = 44$ that is reasonably close to the wind-balance parameter adopted in Table 1. This looks encouraging, though there remain challenges for future, 3D dynamical models to resolve in accounting for the phase-dependent absorption through the WC-star wind where the simple absorption model of Eq. 1 breaks down.

The simple model of the phase-dependent O-star wind absorption implies consistent mass-loss rate estimates from measurements made over more than a year. The mass-loss rate may be low and dependent on elemental abundances that take no account of any mass-exchange that may have taken place in the course of the binary system's evolution but it does have the merit of demonstrating the sensitivity of X-ray absorption measurements of colliding-wind systems for making realistic clumping-free estimates of the mass-loss rates of the O stars in these systems and determining the extent of the absorbing media.

By contrast, point estimates following the same procedure of the WC-star mass-loss rate from its absorption lead to inconsistent values depending on orbital phase that differ by a factor of a few. In the formation and dissipation mechanisms of collisionless shocks, it becomes necessary to consider instead the established importance of reflected ions as described, for example, by Burgess & Scholer (2015) and Madanian et al. (2021b). Reflected ions form a "sheath" of cool material around the collisionless shock, and, for WR140, the sheath on the WC7-side of the shock would consist largely of He & C rich material with large X-ray opacity. Observations of collisionless shocks in supernovae suggest

that the reflected-ion fraction increases with Mach number, reaching up to 50% or more of the material entering the shock (Ghavamian et al. 2013). The similarities between collisionless shocks in colliding-wind binaries and supernovae was emphasized earlier (Pollock et al. 2005).

Figure 10 shows that, at the highest columns observed, there's relatively little change of N_x with θ/b, indicating a thick source of absorbing material which remains relatively independent of the orbital geometry as the stars move from O star inferior conjunction through WC star inferior conjunction and beyond. Zhekov (2021) used 2D hydrodynamic models of WR 140's *RXTE* data precisely to argue for an additional absorption component, although leaving its origin open. In this orbital phase range, the WC star is in front of the shock boundary, so it seems natural to suggest that the outer surface of WR 140's collisionless shocks are enveloped in a sheath of reflected ions through which the X-rays from the colliding wind shock pass and that dominates the observed absorption in the range of maximum absorption, $0.01 < \theta/b < 0.02$, shown in Figure 10. The ionization state and chemical abundance of the reflected ion sheath would be similar to upstream WC7 wind and present an immediate additional absorption to the X-rays originating immediately on the other side of the shock discontinuity. Because X-ray absorption would occur mainly in the enriched carbon content of the WC-star material, this would be the first direct detection outside the solar system of the reflection of heavy ions in high Mach-number collisionless shocks, and an astrophysical analog to the He II reflected ion sheath in the magnetosphere directly detected by Madanian et al. (2021a). In order to satisfy mass continuity the sheath would also have some dynamical structure that involves flow parallel to the shock that might be visible in the velocity structure of long-wavelength absorption lines in either stellar continuum at favourable orbital phases as discussed below for He I λ10830. In WR 140 it also becomes possible to explore the shock formation process involving ion reflection as a function of density and velocity shear driven by the orbital motion of the stars.

6.3.1. X-ray Absorption and Dust

We compared the column density variations to the K-band lightcurve in Figure 15 for contemporaneous data taken as part of the 2016 periastron passage observing campaign. The K-band lightcurve, a measure of the brightness of the periodic dust formation, is shown in orange. The K-band brightness increases almost exactly at periastron passage (although it's not clear why the dust appears so precisely here and not sometime before or after), which suggests that dust nucleation begins very near periastron or that it first becomes visible to the observer at periastron passage. In either case there's no physical reason why this coincidence would occur, unless the cold, dust-forming gas is embedded within the hot shocked gas and somehow shielded from the harsh radiative environment near the WC7 and O5 stars (as suggested by Williams et al. 2009) and the X-ray emission of the shocked gas in the collision zone. As noted above, the rapid increase in X-ray column density begins about 50 days before periastron passage. About one month after periastron passage, the decline in K-band brightness is (unexpectedly) very similar to the decline in column density. The fading in K-band brightness is believed to be due to the cooling of dust in the dust shell as it expands away from WR 140. The similarity between the decline in K-band brightness and decline in X-ray column may indicate a physical connection between the X-ray absorption and the dust shell, i.e. it may be that some of the X-ray absorption arises in the dust shell itself, as well as in the unshocked wind of the WC star.

In Figure 15, the relative K-band flux is derived from the K-band magnitudes as $F_K = 10^{-K/2.5}$, where F_K is the relative K-band flux and K the K-band magnitude. The K-band increase starts within five days of periastron passage (unfortunately there is no K-band data in the interval $\approx \pm 2.5$ days around periastron passage in 2016). The increase in K-band brightness occurs well after the start of the increase in X-ray column density, and maximum K-band brightness occurs after maximum X-ray absorption (which, as noted, occurs very near superior conjunction of the O star). The K-band brightness does not reach its maximum until about 70 days after periastron. Assuming the speed of the dust is 1600 km s^{-1} (Williams et al. 1990), after 70 days the dust has moved 65 AU, about 5 times the semi-major axis of WR 140. After K-band brightness reaches its maximum, it begins to decline exponentially, with an e-folding time of about 153 days. In the $H-$band and other short-wavelength IR bands, the brightness starts to decline shortly after dust formation ends (Williams et al. 1990). At longer IR bands, the brightness maximum is reached at later orbital phases and the decline is slower, as the dust cools and the peak emission moves to longer wavelengths.

6.3.2. X-ray and He I λ10830 Absorption

Williams et al. (2021) describes the variation of the P-Cygni He I λ10830 line near the 2009 and 2016 periastron passages. The He I λ10830 emission and absorption components are primarily produced by the He-rich wind of the WC7 star. This line is both very bright, with a flux exceeding the 2 – 10 keV X-ray flux for most of the orbit and complex, showing an emission sub-peak which varies with orbital phase in strength and radial velocity. The P-Cygni
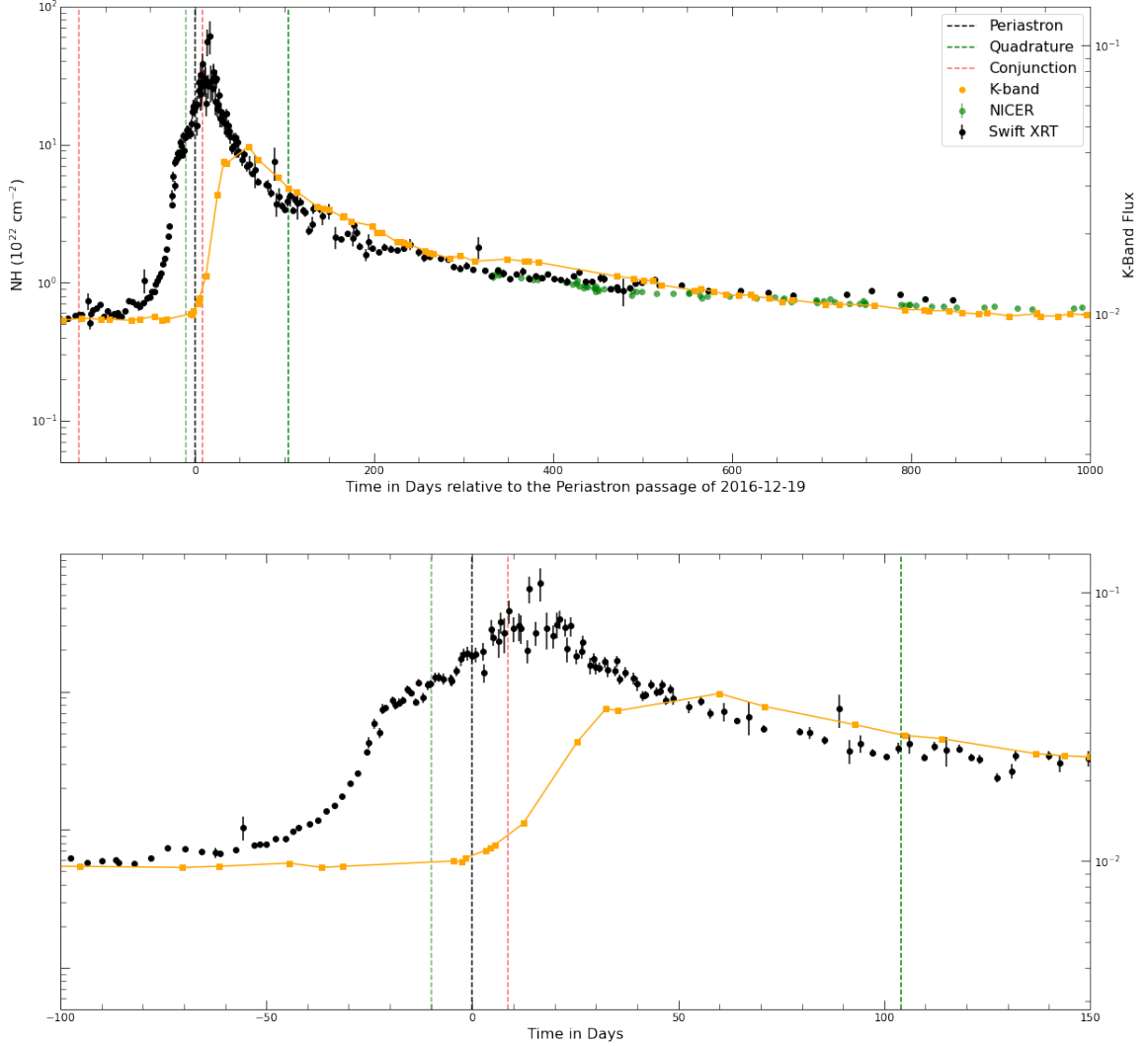
Figure 15. Comparison of the X-ray column density derived from *Swift* and *NICER* spectra, with the variation in relative K-band flux vs. orbital phase around the 2016 periastron passage. The decline in N_H is well correlated with the decline in relative K-band flux.

absorption is seen in the radial velocity range -3000 km s$^{-1} < V < -2000$ km s^{-1}, and so is produced by He-rich gas from the WC7 star lying along the line of sight in front of the stars. We compared the equivalent widths of the He I $\lambda10830$ P-Cygni absorption (given in Tables 1 & 2 of Williams et al. 2021) to the X-ray absorption column measured from the *Swift* and *NICER* spectra (see Fig. 16).

As discussed by Williams et al., the observed variation in the equivalent width of the He I absorption is mostly due to absorption variations in the WC7 wind along the line of sight to the O star, since the amount of WC7 material in front of the O star varies systematically as the orientation and separation of the stars change with orbital motion. There's an interval of (mostly) weak absorption near the time of inferior conjunction of the O star since near this phase O star
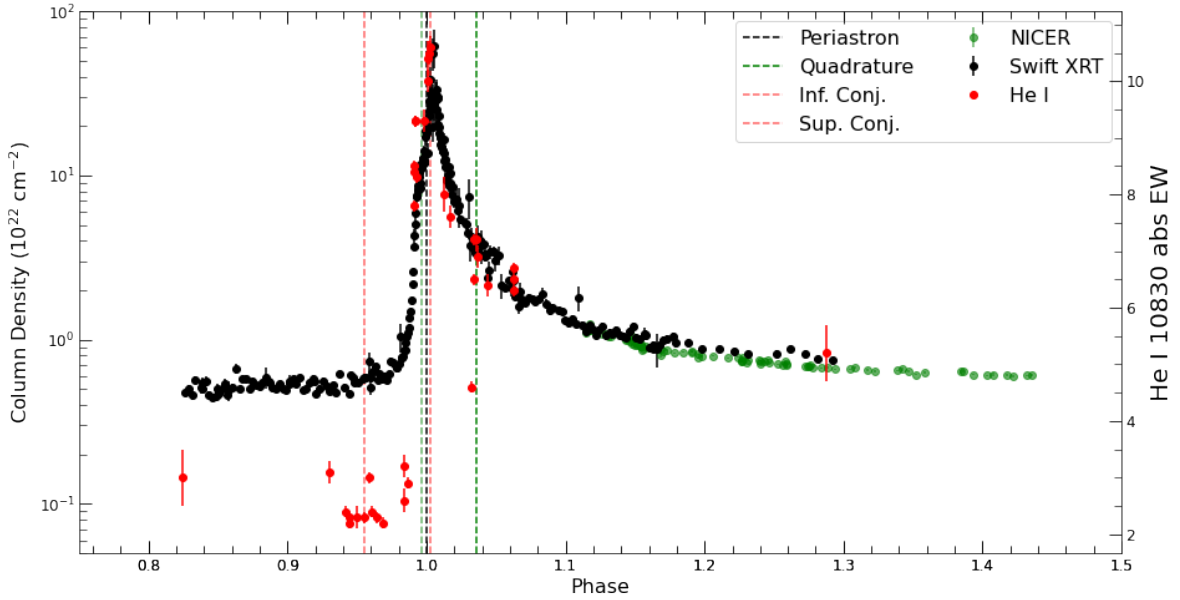
Figure 16. Comparison of the equivalent width of the He I 1.083μ P-Cygni absorption component from Williams et al. (2021) to the X-ray column densities as measured from the analysis of the *Swift* and *NICER* spectra versus orbital phase.

is mostly viewed through its own lower-density wind which fills the shock cavity. Starting at roughly $\phi \approx 0.98$ (when the trailing arm of the colliding wind bow shock passes the observer's line of sight) both stars and the colliding wind shock are viewed through the dense wind of the WC7 star and the X-ray column and He I absorption increase rapidly, reach maxima near superior conjunction of the O star, and then gradually decline. The variation in X-ray column is larger than the observed variation in He I equivalent width; a drop by about a factor of 50 in X-ray column corresponds to a decline of about a factor of 2 in He I equivalent width. This may suggest that some of the absorption is filled in by high velocity, blueshifted emission. As discussed by Williams et al., there's a spectrum showing anomalously strong He I absorption near the inferior conjunction of the O star (near $\phi \approx 0.96$), and anomalously weak absorption near the second quadrature (near $\phi \approx 1.04$). These probably arise from stochastic density variations produced by instabilities in the WC7 wind near the colliding-wind bow shock, as noted by Williams et al. (2021).

6.4. *The Relic Component*

The *Swift* data presented in Figure 12 show that the relic component can be first seen about 25 days prior to periastron passage up to 50 days after periastron passage, when absorption is high enough that the colliding wind component is a negligible contributor to the emission in the 0.4-2.0 keV band. The *Swift* data also show that the flux of this component is not strongly variable through this interval. Sugawara et al. (2015) suggested that this component is radiative recombination continua produced by the shocked wind as it cools (perhaps as a precursor to dust formation), but this seems unlikely given the *Swift* observations. In this 75 day interval around periastron the stellar winds have flowed out a distance $\sim$124 AU. Assuming the recombining gas is entrained in the wind, it's difficult to see how this gas could show a relatively constant X-ray brightness while moving such a large distance while experiencing large changes in density and temperature. The *Swift* observations of the relic component suggest that this is instead a soft, relatively constant source. This source has a flux of 1.1×10^{-12} ergs cm^{-2} s^{-1}, corresponding to a luminosity of 2.9×10^{32} ergs s^{-1}. The X-ray flux from the embedded shocks in the O star wind should be approximately 1.4×10^{32} erg s^{-1}, since the luminosity of the O5.5fc star is $L_O \approx 3.5\times10^5 L_\odot$ (Thomas et al. 2021) using the canonical relation for X-ray luminosity from embedded wind shocks in O stars, $L_x/L_{bol} \approx 10^{-7}$. It's unlikely that the O5.5fc star is the source of the "relic" component, however, since near periastron passage the star is behind the WC7 star, so that any soft emission in its wind would suffer significant, and significantly variable, absorption by the wind of the WC7 star. Another alternative

is that this emission is produced by embedded shocks within the wind of the WC7 star, which seems unlikely since in general single WC7 stars are very weak X-ray sources. The emission could be produced by a third unresolved O-type star in the system, but this also seems unlikely since the star would need to be similarly bright as the O5.5fc star. η Car shows soft, constant X-ray emission from the "Outer Debris Field", the shell of ejecta produced by the eruption of the star in the 1840's. Unresolved ejecta near the star from some past outburst of WR 140 could also reveal itself as the "relic" component, but there's no recorded outburst of WR 140, so this alternative seems unlikely as well. Perhaps the most likely explanation is that this source is similar to the "Central Constant Emission" component seen in η Car (Hamaguchi et al. 2007), which is produced by residual hot shocked gas trapped between the distorted shock cone near periastron passage (Russell et al. 2016).

6.5. *Comparison with η Car*

Long-period, eccentric massive binaries are hard to detect unless they present evidence of wind-wind collision emission. This is because the stars in these systems spend most of their time near apastron, in accordance with Kepler's second law. In the case of WR 140, for example, it takes the component star 1220 days (about 40% of the orbital period) to travel ± 0.05 in orbital phase around apastron, while around periastron the same interval in phase is covered in only 25 days (about 1% of the orbital period). Because stellar radial velocity variations are minimal at apastron, and photocenter variations non-existent, it's difficult or nearly impossible to identify such systems using classical radial velocity, photometric or proper-motion surveys in the absence of colliding-wind effects. Such systems can be identified, as in the case of WR 140 and other carbon-rich "dustars" (like WR 125 and WR 19) via periodic brightening in the IR caused by dust formation in the compressed wind collision near periastron. But it usually requires a bit of patience and/or luck in order to catch such dust formation episodes as they are occurring. The X-ray emission produced by colliding winds is a more constant tracer, since X-rays are produced through most of the orbit and since single WR stars are usually weak X-ray sources.

Both WR 140 and η Car are now understood as long-period, highly-eccentric binary systems and first recognized as such based on variations produced by their wind-wind collision regions. In both cases, periodic variations in the IR were reported – but the nature of these variations was rather mysterious and their ties to a putative companion star unclear. In both WR 140 and η Car, such periodic photometric variations were initially discussed in terms of "shell events" (periodic ejection of shells of material from a – perhaps single – star). Early X-ray observations of the stars revealed unusually bright X-ray flux, whose origin was also at first unclear, but which is now recognized as a clear sign of the presence of hot shocked gas produced by a wind-wind collision. Establishing strictly periodic photometric variability though long, painstaking campaigns in the IR (Moffat et al. 1987) and radio (White & Becker 1995b), coupled with sporadic X-ray observations (Pollock 1985; Williams et al. 1990) made a convincing case for the presence of another star in WR 140, confirmed by subsequent observations in the radio and optical, along with high-resolution ground-based radial-velocity studies which spatially and spectrally resolved the orbital motions of the two stars (and even showed emission from the ionized gas in the bow shock). Similarly in the case of η Car, observations of periodic variations in the equivalent width of the He I $\lambda 10830$ emission line over half a century, along with Paschen line variations (Damineli 1996; Damineli et al. 1997), and hard (Seward & Chlebowski 1982), variable (Ishibashi et al. 1999) X-ray emission provided persuasive evidence that η Car is also a long-period, highly eccentric binary (even though η Car's companion star has not been directly seen).

The X-ray behavior of η Car and WR 140 shows similar variation with orbital phase – long, slow rise in flux, a sudden drop accompanied by an increase in absorption, a brief flux minimum, the appearance of a soft component during the minimum – but also important differences. The 2-10 keV X-ray minimum in η Car appears flat-bottomed (mostly due to the presence of circumstellar X-ray background emission) and to last for 30–60 days before increasing in flux. WR 140's X-ray minimum state in the same band only lasts for about 10 days once the minimum is reached. Figure 17 compares the X-ray flux variations of WR 140 and η Car, normalized to their fluxes at apastron. Although η Car is about an order of magnitude brighter in the 2–10 keV band (and about $15\times$ brighter in X-ray luminosity), the ratio of X-ray flux at maximum to X-ray flux at apastron is about a factor of two greater for WR 140 compared to η Car. These differences may be due to differences in orbital eccentricity, if the orbital eccentricity of η Car is lower than the eccentricity of WR 140 ($e = 0.90$). Other important differences that shape the X-ray lightcurves are the relative terminal stellar wind speeds V_∞ of the component stars in the binary (V_∞ is about a factor of 8 different for the stars in η Car, and nearly the same for the two stars in WR 140), along with wind (and circumstellar) absorption.
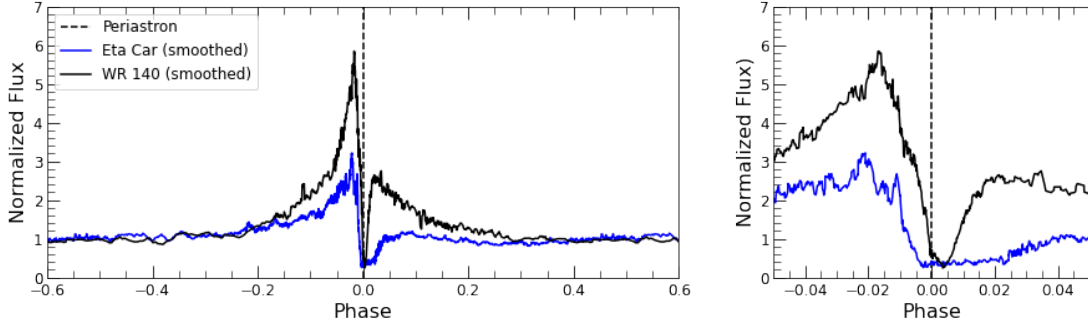
Figure 17. *Left*: Comparison of the 2–10 keV X-ray lightcurve of WR 140 from *RXTE*, *Swift* and *NICER*, to the 2–10 keV *RXTE* and *Swift* fluxes for η Car, normalized at apastron. η Car is about an order of magnitude brighter than WR 140 at apastron. The phases for η Car are calculated using the periastron passage epoch T_o = JD 2,456,874.4 from Teodoro et al. (2016) and the X-ray period, 2023.7 days, and fluxes from Corcoran et al. (2017). The lightcurves for each binary have been combined and smoothed using a 5-point boxcar for display purposes. *Right*: The phase interval near periastron passages for the two binaries.

On approach to X-ray maximum, η Car's X-ray flux shows large variations on timescales of weeks to days (Corcoran et al. 1997; Moffat & Corcoran 2009). This variability has not been seen in any of the pre-minimum phase intervals for WR 140, and flux variations (apparently stochastic) appear to be $< 10 - 20\%$ at any phase. Moffat & Corcoran (2009) suggested that the flux variations in η Car are driven by large, stochastic overdensities ("clumps") in the massive, slow wind of the LBV primary, η Car-A. If this is the case, the relative smoothness of the WR 140's X-ray lightcurve may reflect the smoothness of the wind of the WC7 star, perhaps because its higher-velocity wind helps reduce out any perturbations before they can grow substantially.

7. CONCLUSIONS

In the 66 years since the initial suggestion by Gold (Temple 1955, p103) that shock discontinuities occur in low-density plasmas on scales far shorter than their long Coulomb collisional mean-free-paths, collisionless shocks have become recognised as central for the understanding of gas dynamics throughout the Universe. Similarly, in the 45 years since the predictions by Prilutskii & Usov (1976) and Cherepashchuk (1976) that Wolf-Rayet binary systems should be bright sources of X-rays from shocked gas produced by the dynamical interaction of two counterstreaming supersonic stellar-wind plasmas, observations have confirmed their high luminosities among hot-star X-ray sources. WR 140 is the preeminent example that unites these two themes for its exceptional X-ray brightness among other observational riches and the precision with which its orbital and stellar parameters are known, allowing the boundary conditions to be accurately defined under which the collisionless shocks arise.

The accumulation of nearly 1000 X-ray observations and nearly complete phase coverage have allowed some progress to be made towards a coherent understanding of the physics underlying its collisionless shocks and the various instruments that have been employed. WR 140 is bright enough in the X-ray band for statistical errors to be smaller than residual low-levels of systematic calibration errors. In order to exploit the promise of high-precision collisionless-shock physics enabled by WR 140, attention has variously been necessary to instrumental features such as X-ray pile-up, optical loading, background contamination and cross-calibration. Within these limits and within the framework of a colliding-wind binary model in which the shocks are understood to be collisionless, a clear and consistent set of conclusions has emerged from campaigns with *RXTE*, *Swift*, and *NICER* in the first 20 years of the 21st century regarding WR 140's behaviour as a function of the phase of its highly eccentric 7.94-year orbit:

- X-ray emission and absorption from WR 140 are repeatable with orbital phase

- The smooth X-ray lightcurve shows no evidence of instabilities or other short-term variability or of changes in its effective temperature

- Shock X-ray luminosity is inversely proportional to binary separation for most of the orbit

- Luminosity departures near periastron are largely restored in a switch from X-rays to excess optical line emission that probably operates on a microscopic level

- The shock energy budget probably also involves magnetic-field generation through the Weibel instability

- Foreground X-ray absorption occurs upstream in the wind terminal-velocity regimes of both WC7 and O5 stars according to phase allowing clumping-free estimates of their mass-loss rates and the interstellar absorption

- Features in the X-ray absorption curve arise from the geometry of the shock system

- Shock-reflected ions would naturally explain a substantial part of the X-ray absorption by the WC-star wind

- Dust-powered K-band photometry and He I 1.083μ absorption are correlated in their own fashion with the falling X-ray absorption after periastron

- Residual soft X-rays revealed near periastron are less variable than the bulk shock emission and their origin remains uncertain

The full physical implications of the considerable body of accumulated data on WR 140 including the conclusions listed above will require detailed models to be built. In this, we are happy to anticipate sharing with modelers whatever data or summary parameters they may require. In the specific context of collisionless shocks, it is an open question how successful fluid models might be or whether kinetic particle-in-cell calculations are necessary or even feasible. In either case, the shock continuity equations that determine post-shock conditions on the basis of things we know probably need to face adjustments that conceivably involve, for example, reflected ions; magnetic-field generation; non-thermal particle acceleration; or cooling competition. The presence of a sheath of reflected ions could also provide an alternative dense environment cooler than shocked gas that might be worth considering as a possible site for dust formation.

As evident from WR 140, the utility of complete and repeated phase coverage should encourage similar efforts in other binary systems. These might be especially worthwhile in objects for which even currently available piecemeal work has already shown to have interesting behavior such as V444 Cygni (Lomax et al. 2015) or γ^2 Velorum (Schild et al. 2004).

Future work on WR 140 itself should immediately entail absorption measurements to close the vertical loop in Figure 10 to trace the comparatively slow transition between WC-star and O-star winds and to seek a global absorption minimum to test the reliability of the interstellar component estimated above. More important will be plans to explore further the complementary relationship established here between competitive means of plasma cooling in at least two ways: by establishing precise timing of the total radiative luminosity compared with the key orbital event of periastron; and by comparing the velocity profiles of the emission lines at short X-ray wavelengths and long optical or IR wavelengths. These will help to determine the extent to which the X-ray and excess optical emission arise in the same physical space and establish how prompt are electron and ionic heating.

The current data suggest that WR 140's X-ray properties are highly predictable and that it could or should therefore serve as a calibration source both for high-energy instruments and for numerical models of shock formation. In any case, the way seems open for WR 140 to become a key reference point for the study of collisionless shocks. The space physics and astrophysics communities might join forces in devising ideas for observations and models to exploit the richness of its observational variety to advance understanding of physical processes that operate throughout the Universe.

Facility: RXTE(PCA),

Facility: Swift(XRT),

Facility: NICER(XTI).

REFERENCES

Anders, E., & Grevesse, N. 1989, GeoCoA, 53, 197

Arzoumanian, Z., Gendreau, K. C., Baker, C. L., et al. 2014, in Society of Photo-Optical Instrumentation Engineers (SPIE) Conference Series, Vol. 9144, Space Telescopes and Instrumentation 2014: Ultraviolet to Gamma Ray, 914420

Bradt, H. V., Rothschild, R. E., & Swank, J. H. 1993, A&AS, 97, 355

Burgess, D., & Scholer, M. 2015, Collisionless Shocks in Space Plasmas

Burrows, D. N., Hill, J. E., Nousek, J. A., et al. 2000, in Society of Photo-Optical Instrumentation Engineers (SPIE) Conference Series, Vol. 4140, X-Ray and Gamma-Ray Instrumentation for Astronomy XI, ed. K. A. Flanagan & O. H. Siegmund, 64–75

Canto, J., Raga, A. C., & Wilkin, F. P. 1996, ApJ, 469, 729

Cherepashchuk, A. M. 1976, Soviet Astronomy Letters, 2, 138

Corcoran, M. F., Hamaguchi, K., Pittard, J. M., et al. 2010, ApJ, 725, 1528

Corcoran, M. F., & Heap, S. R. 1990, in Astronomical Society of the Pacific Conference Series, Vol. 7, Properties of Hot Luminous Stars, ed. C. D. Garmany, 294–296

Corcoran, M. F., Ishibashi, K., Davidson, K., et al. 1997, Nature, 390, 587

Corcoran, M. F., Pollock, A. M. T., Hamaguchi, K., & Russell, C. 2011, ArXiv e-prints, arXiv:1101.1422

Corcoran, M. F., Liburd, J., Morris, D., et al. 2017, ApJ, 838, 45

Damineli, A. 1996, ApJL, 460, L49+

Damineli, A., Conti, P. S., & Lopes, D. F. 1997, New Astronomy, 2, 107

De Becker, M., Pittard, J. M., Williams, P., & WR140 Consortium. 2011, Bulletin de la Societe Royale des Sciences de Liege, 80, 653

de la Chevrotière, A., St-Louis, N., Moffat, A. F. J., & MiMeS Collaboration. 2014, ApJ, 781, 73

Dimmock, A. P., Russell, C. T., Sagdeev, R. Z., et al. 2019, Science Advances, 5, eaau9926

Dorman, B., & Arnaud, K. A. 2001, in Astronomical Society of the Pacific Conference Series, Vol. 238, Astronomical Data Analysis Software and Systems X, ed. F. R. Harnden, Jr., F. A. Primini, & H. E. Payne, 415

Dougherty, S. M., Beasley, A. J., Claussen, M. J., Zauderer, B. A., & Bolingbroke, N. J. 2005, ApJ, 623, 447

Eldridge, J. J., Izzard, R. G., & Tout, C. A. 2008, MNRAS, 384, 1109

Fahed, R., Moffat, A. F. J., Zorec, J., et al. 2011, MNRAS, 418, 2

Farrington, C. D., Fekel, F. C., Schaefer, G. H., & ten Brummelaar, T. A. 2018, AJ, 156, 144

Gayley, K. G. 2009, ApJ, 703, 89

Gehrels, N., Chincarini, G., Giommi, P., et al. 2004, The
    Astrophysical Journal, 611, 1005

Ghavamian, P., Schwartz, S. J., Mitchell, J., Masters, A., &
    Laming, J. M. 2013, SSRv, 178, 633

Grunhut, J. H., Wade, G. A., Neiner, C., et al. 2017,
    MNRAS, 465, 2432

Hamaguchi, K., Corcoran, M. F., Gull, T., et al. 2007, ApJ,
    663, 522

Hartman, H., Gull, T., Johansson, S., Smith, N., & HST
    Eta Carinae Treasury Project Team. 2004, A&A, 419, 215

Hervieux, Y. 1995, in IAU Symposium, ed. K. A. van der
    Hucht & P. M. Williams, 460−+

Hill, G. M., Moffat, A. F. J., & St-Louis, N. 2002, MNRAS,
    335, 1069

—. 2018, MNRAS, 474, 2987

Huntington, C. M., Manuel, M. J. E., Ross, J. S., et al.
    2017, Physics of Plasmas, 24, 041410

Ishibashi, K., Corcoran, M. F., Davidson, K., et al. 1999,
    ApJ, 524, 983

Jahoda, K., Markwardt, C. B., Radeva, Y., et al. 2006,
    ApJS, 163, 401

Kato, T. N., & Takabe, H. 2008, ApJL, 681, L93

Koyama, K., Maeda, Y., Tsuru, T., Nagase, F., & Skinner,
    S. 1994, PASJ, 46, L93

Kruckow, M. U., Tauris, T. M., Langer, N., Kramer, M., &
    Izzard, R. G. 2018, MNRAS, 481, 1908

Langer, N., van Marle, A. J., & Yoon, S. C. 2010, NewAR,
    54, 206

Leitherer, C. 1988, ApJ, 326, 356

Lomax, J. R., Nazé, Y., Hoffman, J. L., et al. 2015, A&A,
    573, A43

Madanian, H., Schwartz, S. J., Fuselier, S. A., et al. 2021a,
    arXiv e-prints, arXiv:2106.10214

Madanian, H., Desai, M. I., Schwartz, S. J., et al. 2021b,
    ApJ, 908, 40

Madura, T. I., Gull, T. R., Owocki, S. P., et al. 2012,
    MNRAS, 420, 2064

Marchenko, S. V., Moffat, A. F. J., Ballereau, D., et al.
    2003, ApJ, 596, 1295

Marcowith, A., Bret, A., Bykov, A., et al. 2016, Reports on
    Progress in Physics, 79, 046901

Martins, F., & Hillier, D. J. 2012, A&A, 545, A95

Massey, P. 1984, ApJ, 281, 789

Meynet, G., & Maeder, A. 2003, A&A, 404, 975

Moffat, A. F. J., & Corcoran, M. F. 2009, ApJ, 707, 693

Moffat, A. F. J., Lamontagne, R., Williams, P. M., Horn,
    J., & Seggewiss, W. 1987, ApJ, 312, 807

Monnier, J. D., Zhao, M., Pedretti, E., et al. 2011, ApJL,
    742, L1

Parkin, E. R., & Gosset, E. 2011, A&A, 530, A119+

Pittard, J. M. 2007, ApJL, 660, L141

Pittard, J. M., & Dawson, B. 2018, MNRAS, 477, 5640

Pittard, J. M., & Dougherty, S. M. 2006, MNRAS, 372, 801

Pittard, J. M., & Parkin, E. R. 2010, MNRAS, 403, 1657

Pittard, J. M., & Stevens, I. R. 2002, A&A, 388, L20

Plucinsky, P. P., Beardmore, A. P., Foster, A., et al. 2017,
    A&A, 597, A35

Pollock, A. M. T. 1985, SSRv, 40, 63

Pollock, A. M. T. 2012, in Astronomical Society of the
    Pacific Conference Series, Vol. 465, Proceedings of a
    Scientific Meeting in Honor of Anthony F. J. Moffat, ed.
    L. Drissen, C. Rubert, N. St-Louis, & A. F. J. Moffat, 308

Pollock, A. M. T., Corcoran, M. F., Stevens, I. R., &
    Williams, P. M. 2005, ApJ, 629, 482

Pollock, A. M. T., Haberl, F., & Corcoran, M. F. 1995, in
    IAU Symposium, ed. K. A. van der Hucht & P. M.
    Williams, 512−+

Pourbaix, D., Tokovinin, A. A., Batten, A. H., et al. 2004,
    A&A, 424, 727

Prigozhin, G., Gendreau, K., Doty, J. P., et al. 2016, in
    Proc. SPIE, Vol. 9905, Space Telescopes and
    Instrumentation 2016: Ultraviolet to Gamma Ray, 99051I

Prilutskii, O. F., & Usov, V. V. 1976, Soviet Astronomy,
    20, 2

Remillard, R. A., Loewenstein, M., Steiner, J. F., et al.
    2021, arXiv e-prints, arXiv:2105.09901

Russell, C. M. P., Corcoran, M. F., Hamaguchi, K., et al.
    2016, MNRAS, 458, 2275

Russell, C. M. P., Okazaki, A. T., Owocki, S. P., et al.
    2013, in Massive Stars: From alpha to Omega, 182

Sana, H., de Mink, S. E., de Koter, A., et al. 2012, Science,
    337, 444

Schild, H., Güdel, M., Mewe, R., et al. 2004, A&A, 422, 177

Setia Gunawan, D. Y. A., van der Hucht, K. A., Williams,
    P. M., et al. 2001, A&A, 376, 460

Seward, F. D., & Chlebowski, T. 1982, ApJ, 256, 530

Shaposhnikov, N., Jahoda, K., Markwardt, C., Swank, J.,
    & Strohmayer, T. 2012, ApJ, 757, 159

Smith, R. K., Brickhouse, N. S., Liedahl, D. A., &
    Raymond, J. C. 2001, ApJL, 556, L91

Snow, Jr., T. P., & Morton, D. C. 1976, ApJS, 32, 429

Stevens, I. R., Blondin, J. M., & Pollock, A. M. T. 1992,
    ApJ, 386, 265

Sugawara, Y., Maeda, Y., Tsuboi, Y., et al. 2015, PASJ, 67,
    121

Temple, G. 1955, in Gas Dynamics of Cosmic Clouds, ed.
    J. M. Burgers & H. C. van de Hulst, Vol. IAU Symp. 2
    (North Holland Publishing Co., Amsterdam), 97

Teodoro, M., Damineli, A., Heathcote, B., et al. 2016, ApJ, 819, 131

Thomas, J. D., Richardson, N. D., Eldridge, J. J., et al. 2021, arXiv e-prints, arXiv:2101.10563

Usov, V. V. 1992, ApJ, 389, 635

Vanbeveren, D., De Greve, J. P., De Loore, C., & van Dessel, E. L. 1979, A&A, 73, 19

Weber, E. J., & Davis, Leverett, J. 1967, ApJ, 148, 217

White, R. L., & Becker, R. H. 1995a, ApJ, 451, 352

—. 1995b, ApJ, 451, 352

Williams, P. M. 1996, in Revista Mexicana de Astronomia y Astrofisica Conference Series, ed. V. Niemala & N. Morrell, 47–+

Williams, P. M., Beattie, D. H., Lee, T. J., Stewart, J. M., & Antonopoulou, E. 1978, MNRAS, 185, 467

Williams, P. M., van der Hucht, K. A., Florkowski, D. R., Pollock, A. M. T., & Wamsteker, W. M. 1987, in IAU Symposium, Vol. 122, Circumstellar Matter, ed. I. Appenzeller & C. Jordan, 453–454

Williams, P. M., van der Hucht, K. A., Pollock, A. M. T., et al. 1990, MNRAS, 243, 662

Williams, P. M., van der Hucht, K. A., & Spoelstra, T. A. T. 1994, A&A, 291, 805

Williams, P. M., Marchenko, S. V., Marston, A. P., et al. 2009, MNRAS, 395, 1749

Williams, P. M., Varricatt, W. P., Chené, A.-N., et al. 2021, MNRAS, 503, 643

Wilms, J., Allen, A., & McCray, R. 2000, ApJ, 542, 914

Wright, A. E., & Barlow, M. J. 1975, MNRAS, 170, 41

Zhekov, S. A. 2021, MNRAS, 500, 4837

Zhekov, S. A., & Skinner, S. L. 2000, ApJ, 538, 808

APPENDIX

A. SAMPLE SPECTRA

To show the differences in spectral resolution and energy sensitivity, we show sample spectra in the orbital phase range $0.1 < \phi < 0.4$ in A1. This phase range was chosen because it's the only range sampled by all 3 instruments, and also because there's relatively little variation in flux within this range. To improve statistics, these spectra are combined from all the spectra for a given instrument in this phase range. The the *RXTE*-PCA spectrum is combined from net spectra, where the net spectrum has been accumulating after correcting individual *RXTE*-PCA spectra for estimated instrumental background. No background correction has been applied to either the *NICER*-XTI or *Swift*-XRT spectra.
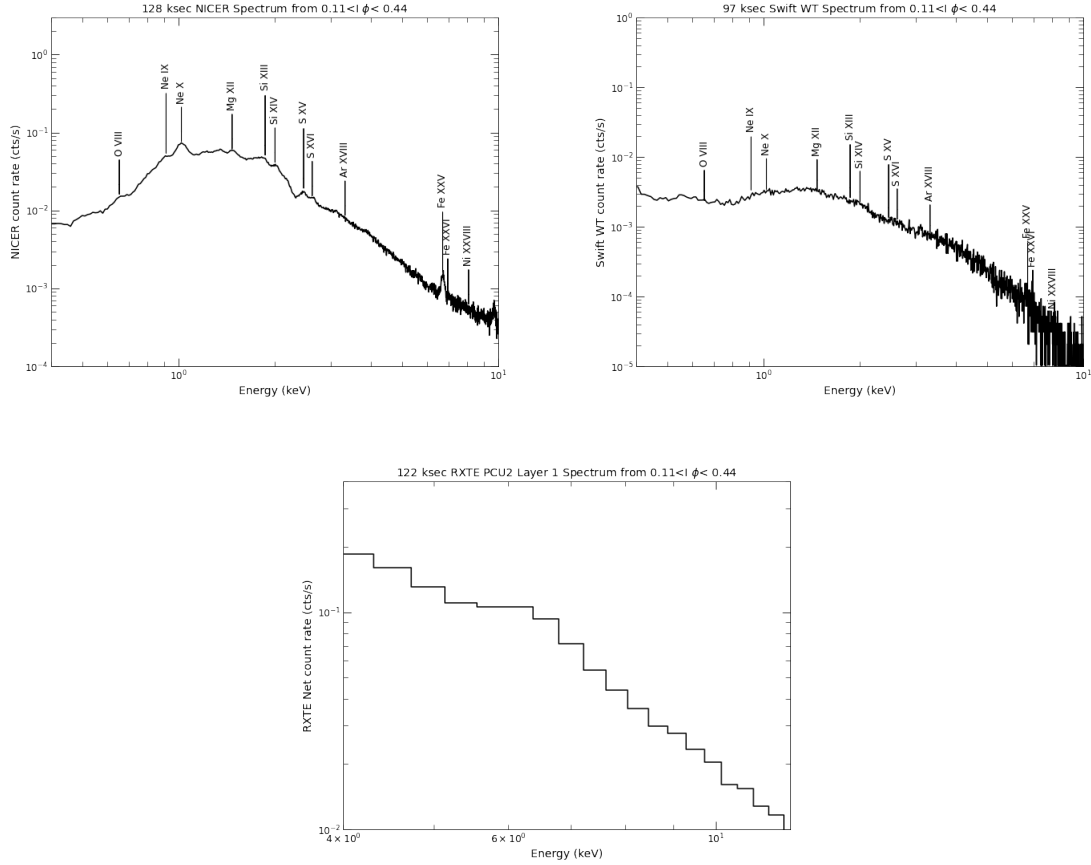
Figure A1. Comparison of combined spectra from the 3 instruments (*NICER*-XTI, *Swift*-XRT and *RXTE*-PCA) in a common interval of WR 140's orbital phase ($0.1 < \phi < 0.4$). Some strong lines are marked in the *NICER*-XTI and *Swift*-XRT spectrum (the poor spectral resolution of the *RXTE*-PCA means it's incapable of resolving line features, though the Fe XXV feature does show up as an apparent "shelf" near 6.7 keV). The *Swift*-XRT PC-mode data are not shown because there were only 4 PC-mode observations in this phase interval.

Table A1. Log of *RXTE* Observations and Fluxes

Sequence	MJD	Phase	Expo.	Net Rate	Rate Error	Bkg Rate	Flux	Error
			s	cts/s	cts/s	cts/s	10^{-11} ergs/s/cm^2	10^{-11} ergs/s/cm^2
2000120902	51887.106	1.978	1472.0	6.56	0.11	12.29	5.19	0.17
2000121607	51894.334	1.980	1440.0	6.65	0.12	13.02	5.56	0.18
2000122305	51901.252	1.983	1248.0	6.87	0.12	12.21	5.67	0.19
2000123004	51908.194	1.985	1440.0	6.71	0.12	12.91	5.56	0.18
2001010608	51915.365	1.988	1584.0	7.07	0.11	12.64	5.15	0.15
2001011406	51923.266	1.990	304.0	5.73	0.24	11.55	3.52	0.28
2001011919	51928.827	1.992	1024.0	5.49	0.13	13.10	3.54	0.17
2001012722	51936.930	1.995	1440.0	3.85	0.11	12.63	2.32	0.13
2001020316	51943.681	1.997	1536.0	2.45	0.10	13.08	1.21	0.12
2001021016	51950.675	2.000	1328.0	1.46	0.10	11.85	0.51	0.11
2001021713	51957.566	2.002	1392.0	0.99	0.10	11.95	0.24	0.11
2001022405	51964.253	2.004	1584.0	1.16	0.10	13.62	0.40	0.12
2001030319	51971.817	2.007	1472.0	2.00	0.10	12.16	0.96	0.12
2001031005	51978.257	2.009	1280.0	3.18	0.11	12.49	1.53	0.12
2001031810	51986.455	2.012	1360.0	3.23	0.11	12.09	1.90	0.13
2001032516	51993.695	2.015	1392.0	3.84	0.11	12.60	2.28	0.13
2001033109	51999.418	2.017	1472.0	3.69	0.11	13.30	2.29	0.14
2001040722	52006.914	2.019	224.0	4.32	0.28	13.53	2.70	0.36
2001041415	52013.665	2.022	1440.0	3.96	0.11	12.87	2.51	0.14
2001042119	52020.821	2.024	944.0	3.98	0.13	12.34	2.47	0.17
2001042811	52027.503	2.026	1376.0	3.81	0.11	12.36	2.44	0.14
2001050515	52034.592	2.029	608.0	4.20	0.17	12.47	2.77	0.22
2001051202	52041.105	2.031	1456.0	3.86	0.11	12.73	2.58	0.15
2001051920	52048.862	2.034	1472.0	3.90	0.10	11.62	2.78	0.15
2001052620	52055.871	2.036	1344.0	3.51	0.11	11.57	2.54	0.16
2001060205	52062.241	2.038	1392.0	3.26	0.10	11.62	2.23	0.15
2001060914	52069.599	2.041	1312.0	3.38	0.11	12.29	2.23	0.15
2001061620	52076.869	2.043	1456.0	3.35	0.10	11.75	2.24	0.14
2001062315	52083.646	2.046	1424.0	3.51	0.11	12.50	2.33	0.15
2001063023	52090.972	2.048	1008.0	3.46	0.13	13.84	2.43	0.19
2001070702	52097.104	2.050	1120.0	3.14	0.12	13.08	2.13	0.17
2001071505	52105.254	2.053	1216.0	2.83	0.11	12.04	2.18	0.18
2001072114	52111.609	2.055	1600.0	3.22	0.10	12.59	2.21	0.14
2001072716	52117.703	2.058	1344.0	2.96	0.11	12.14	2.10	0.16
2001080416	52125.697	2.060	1552.0	2.86	0.10	13.85	2.15	0.17
2001081001	52131.074	2.062	1296.0	2.82	0.11	11.70	2.05	0.17
2001081812	52139.547	2.065	1488.0	3.08	0.10	11.44	2.02	0.14
2001082420	52145.857	2.067	1184.0	2.80	0.11	11.91	2.03	0.17
2001090303	52155.137	2.070	960.0	2.75	0.12	11.68	1.98	0.19
2001090817	52160.753	2.072	1456.0	2.82	0.11	13.79	2.09	0.17
2001091415	52166.642	2.074	1680.0	2.94	0.10	14.30	2.16	0.16
2001092215	52174.650	2.077	1472.0	2.74	0.10	13.02	1.82	0.15
2001093004	52182.190	2.080	1312.0	2.61	0.10	11.65	1.75	0.15
2001100700	52189.014	2.082	1424.0	2.71	0.10	11.83	1.79	0.15
2001101322	52195.958	2.085	1216.0	2.77	0.11	12.06	1.94	0.17
2001101923	52201.980	2.087	288.0	2.28	0.23	12.63	1.67	0.37
2001102621	52208.901	2.089	1312.0	2.89	0.11	12.15	1.95	0.16
2001110305	52216.243	2.092	1632.0	2.81	0.10	12.52	1.92	0.14
2001111016	52223.710	2.094	1584.0	2.89	0.09	11.34	1.92	0.14
2001111712	52230.515	2.096	1440.0	2.58	0.10	11.74	1.79	0.15
2001112520	52238.847	2.099	1648.0	2.93	0.10	12.36	1.91	0.14
2001120318	52246.780	2.102	1264.0	2.45	0.11	11.88	1.76	0.17

Table A1 *(continued)*

Sequence	MJD	Phase	Expo.	Net Rate	Rate Error	Bkg Rate	Flux	Error
			s	cts/s	cts/s	cts/s	10^{-11} ergs/s/cm^2	10^{-11} ergs/s/cm^2
2001121011	52253.489	2.104	912.0	2.71	0.12	11.06	1.71	0.17
2001121819	52261.827	2.107	1232.0	2.43	0.11	11.20	1.84	0.17
2001122500	52268.022	2.109	1408.0	2.48	0.10	11.25	1.69	0.15
2001123003	52273.175	2.111	1504.0	2.15	0.10	11.69	1.64	0.16
2002010610	52280.466	2.114	1456.0	2.35	0.10	10.93	1.73	0.16
2002011316	52287.718	2.116	1968.0	2.40	0.09	12.30	1.70	0.14
2002011903	52293.143	2.118	688.0	2.57	0.14	11.05	1.67	0.20
2002012715	52301.656	2.121	1040.0	2.19	0.12	11.78	1.66	0.20
2002020213	52307.574	2.123	1232.0	2.66	0.11	12.73	1.63	0.15
2002020916	52314.709	2.126	1296.0	2.45	0.10	11.07	1.55	0.15
2002021611	52321.509	2.128	1872.0	2.53	0.09	11.40	1.62	0.12
2002022400	52329.040	2.131	1232.0	2.26	0.11	11.62	1.48	0.16
2002030300	52336.018	2.133	1424.0	2.03	0.10	12.13	1.42	0.16
2002030908	52342.379	2.135	1296.0	2.12	0.10	12.13	1.56	0.18
2002031707	52350.306	2.138	928.0	1.90	0.13	12.96	1.36	0.21
2002032313	52356.549	2.140	336.0	1.83	0.20	11.98	1.45	0.37
2002033108	52364.374	2.143	1648.0	2.42	0.10	12.60	1.61	0.14
2002040811	52372.493	2.146	1296.0	2.04	0.10	11.09	1.49	0.17
2002042101	52385.078	2.150	1456.0	2.13	0.10	11.04	1.50	0.15
2002042706	52391.282	2.152	1520.0	2.17	0.10	11.91	1.51	0.15
2002050518	52399.793	2.155	1008.0	2.13	0.11	10.94	1.39	0.17
2002051203	52406.148	2.157	1328.0	2.13	0.10	11.39	1.48	0.16
2002052006	52414.265	2.160	1296.0	1.84	0.11	13.21	1.51	0.20
2002052719	52421.834	2.163	1712.0	2.06	0.09	10.97	1.50	0.15
2002060202	52427.119	2.164	1488.0	2.34	0.10	11.31	1.50	0.14
2002060823	52433.971	2.167	1472.0	2.27	0.10	11.19	1.41	0.14
2002061714	52442.601	2.170	1312.0	2.37	0.11	12.29	1.36	0.14
2002062513	52450.583	2.172	1424.0	2.08	0.10	11.12	1.29	0.14
2002070122	52456.939	2.175	1680.0	1.92	0.09	11.94	1.22	0.14
2002070809	52463.413	2.177	720.0	2.22	0.14	11.03	1.46	0.21
2002071520	52470.850	2.179	1776.0	2.19	0.09	11.39	1.34	0.12
2002072300	52478.042	2.182	1984.0	2.19	0.08	10.80	1.33	0.11
2002073011	52485.493	2.185	1328.0	2.33	0.10	11.20	1.52	0.15
2002080509	52491.420	2.187	1312.0	2.32	0.10	11.28	1.46	0.15
2002081207	52498.338	2.189	864.0	1.98	0.13	11.63	1.35	0.20
2002081901	52505.052	2.191	1360.0	1.89	0.10	11.39	1.31	0.16
2002082419	52510.819	2.193	1632.0	1.82	0.09	10.78	1.21	0.14
2002090202	52519.130	2.196	1152.0	1.97	0.11	10.91	1.32	0.17
2002090912	52526.510	2.199	1312.0	2.25	0.10	11.43	1.37	0.14
2002091719	52534.805	2.202	2192.0	2.02	0.08	10.76	1.38	0.12
2002092312	52540.542	2.204	800.0	2.22	0.13	11.22	1.25	0.17
2002093001	52547.052	2.206	1552.0	1.76	0.09	11.75	1.09	0.14
2002100800	52555.019	2.209	1248.0	2.03	0.10	11.57	1.22	0.15
2002101422	52561.933	2.211	560.0	1.70	0.15	11.73	1.13	0.25
2002101823	52565.992	2.212	912.0	1.65	0.12	11.59	1.32	0.23
2002102716	52574.678	2.215	1792.0	1.96	0.09	12.40	1.36	0.15
2002110411	52582.505	2.218	1488.0	1.91	0.10	12.82	1.08	0.14
2002111111	52589.485	2.220	1872.0	2.13	0.09	11.61	1.21	0.12
2002111803	52596.141	2.223	1200.0	2.12	0.11	11.37	1.19	0.14
2002112706	52605.282	2.226	1424.0	2.11	0.10	10.86	1.47	0.15
2002120416	52612.688	2.228	928.0	2.01	0.12	11.66	1.33	0.19
2002120913	52617.554	2.230	1136.0	1.79	0.11	11.11	1.14	0.17

Table A1 *(continued)*

Sequence	MJD	Phase	Expo.	Net Rate	Rate Error	Bkg Rate	Flux	Error
			s	cts/s	cts/s	cts/s	10^{-11} ergs/s/cm^2	10^{-11} ergs/s/cm^2
2002121605	52624.255	2.232	1488.0	1.97	0.10	11.61	1.29	0.15
2002122609	52634.396	2.236	1360.0	2.26	0.10	12.15	1.18	0.13
2002123101	52639.081	2.238	1408.0	1.60	0.10	11.24	1.06	0.16
2003010603	52645.133	2.240	784.0	2.08	0.13	11.69	1.31	0.20
2003011415	52653.672	2.243	1648.0	1.82	0.09	11.87	1.34	0.16
2003012023	52659.987	2.245	1264.0	1.50	0.10	10.84	1.18	0.19
2003012707	52666.331	2.247	1440.0	2.27	0.10	11.34	1.22	0.13
2003020217	52672.726	2.249	1040.0	1.46	0.11	10.89	1.03	0.19
2003021102	52681.127	2.252	1504.0	1.47	0.09	10.79	1.00	0.16
2003021511	52685.478	2.254	1376.0	1.51	0.10	11.05	0.99	0.16
2003022514	52695.605	2.257	1376.0	1.76	0.10	12.56	1.14	0.16
2003030400	52702.039	2.259	1120.0	1.69	0.11	11.00	1.16	0.18
2003031214	52710.593	2.262	1120.0	1.60	0.11	11.25	1.10	0.18
2003031813	52716.576	2.264	400.0	1.64	0.18	11.24	1.07	0.29
2005030816	53437.689	2.513	1216.0	1.27	0.10	11.06	0.88	0.19
2005032301	53452.089	2.518	1024.0	1.33	0.12	13.02	0.75	0.19
2005040700	53467.027	2.524	864.0	1.35	0.12	10.80	0.84	0.20
2005042007	53480.334	2.528	528.0	1.54	0.16	11.33	1.07	0.27
2005050423	53494.969	2.533	992.0	1.52	0.11	11.56	0.99	0.19
2005051915	53509.662	2.538	912.0	1.64	0.12	11.25	1.10	0.20
2005060209	53523.414	2.543	368.0	1.43	0.19	11.36	1.01	0.33
2005061423	53535.963	2.547	544.0	1.49	0.15	10.77	1.07	0.27
2005062819	53549.832	2.552	992.0	1.13	0.12	12.47	0.81	0.23
2005071117	53562.734	2.557	912.0	1.63	0.12	11.96	1.08	0.20
2005072519	53576.821	2.562	752.0	1.53	0.13	11.44	0.93	0.21
2005080904	53591.184	2.566	928.0	1.41	0.12	11.61	0.89	0.20
2005082410	53606.452	2.572	896.0	1.14	0.12	11.17	0.97	0.26
2005090612	53619.518	2.576	1056.0	1.27	0.11	11.50	0.74	0.18
2005092200	53635.025	2.582	944.0	1.68	0.12	11.61	1.09	0.19
2005100510	53648.464	2.586	912.0	1.82	0.12	11.46	1.03	0.17
2005101815	53661.655	2.591	944.0	1.67	0.11	10.65	0.89	0.16
2005110300	53677.033	2.596	128.0	2.07	0.33	11.98	1.13	0.44
2005111621	53690.884	2.601	864.0	1.68	0.12	11.33	1.01	0.19
2005120115	53705.671	2.606	1120.0	1.19	0.11	11.51	0.93	0.22
2005121403	53718.128	2.610	32.0	1.00	0.65	12.37	0.55	1.12
2005122912	53733.531	2.616	880.0	1.34	0.12	11.57	0.97	0.22
2006011103	53746.154	2.620	944.0	1.45	0.12	12.74	0.91	0.20
2006012509	53760.388	2.625	864.0	1.53	0.12	11.06	0.97	0.20
2006020821	53774.905	2.630	800.0	1.39	0.13	12.35	0.87	0.22
2006022316	53789.684	2.635	816.0	1.60	0.13	11.45	0.85	0.18
2006030723	53801.971	2.639	1248.0	1.64	0.10	11.23	1.17	0.18
2006032215	53816.654	2.644	896.0	1.76	0.12	12.10	1.02	0.18
2006040506	53830.291	2.649	688.0	1.47	0.14	12.61	1.12	0.27
2006041811	53843.500	2.654	1040.0	1.85	0.11	11.69	1.31	0.19
2006050319	53858.825	2.659	880.0	1.74	0.13	12.55	1.04	0.19
2006051611	53871.476	2.663	880.0	1.83	0.12	11.48	1.14	0.19
2006060108	53887.349	2.669	688.0	1.41	0.15	14.58	1.17	0.31
2006061517	53901.728	2.674	928.0	1.80	0.12	11.42	1.12	0.18
2006062721	53913.912	2.678	896.0	1.47	0.12	11.50	1.07	0.22
2006071215	53928.637	2.683	816.0	1.60	0.12	11.11	1.12	0.22
2006072717	53943.717	2.688	880.0	1.64	0.13	12.66	1.05	0.21
2006080713	53954.589	2.692	944.0	1.50	0.11	10.85	1.08	0.20

Table A1 *(continued)*

Sequence	MJD	Phase	Expo.	Net Rate	Rate Error	Bkg Rate	Flux	Error
			s	cts/s	cts/s	cts/s	10^{-11} ergs/s/cm^2	10^{-11} ergs/s/cm^2
2006082115	53968.658	2.697	992.0	1.97	0.12	11.75	1.13	0.16
2006090507	53983.322	2.702	848.0	1.50	0.12	11.57	1.23	0.25
2006092000	53998.026	2.707	1168.0	1.68	0.10	11.10	1.19	0.18
2006100510	54013.453	2.712	880.0	1.74	0.13	13.68	1.17	0.22
2006101809	54026.414	2.717	848.0	1.70	0.13	11.69	1.12	0.20
2006103121	54039.903	2.721	80.0	1.21	0.41	12.16	0.84	0.77
2006111507	54054.329	2.726	880.0	1.74	0.12	10.92	0.97	0.17
2006112906	54068.261	2.731	1024.0	1.93	0.12	13.83	1.23	0.19
2006121311	54082.495	2.736	720.0	1.70	0.14	12.93	1.11	0.23
2006122719	54096.812	2.741	1056.0	1.66	0.11	12.17	0.95	0.17
2007011008	54110.371	2.746	896.0	1.45	0.13	13.79	1.21	0.26
2007012402	54124.108	2.751	800.0	1.39	0.13	12.69	1.08	0.26
2007020721	54138.903	2.756	752.0	1.55	0.13	10.88	1.08	0.22
2007022013	54151.576	2.760	672.0	1.61	0.14	11.27	1.10	0.23
2007030523	54164.992	2.765	496.0	1.15	0.16	11.85	0.91	0.33
2007032213	54181.588	2.770	848.0	1.36	0.12	11.76	1.08	0.25
2007040402	54194.113	2.775	944.0	1.52	0.12	12.35	1.00	0.20
2007041804	54208.188	2.780	1312.0	1.76	0.11	13.00	1.25	0.18
2007050301	54223.054	2.785	928.0	1.86	0.12	11.12	1.30	0.20
2007051602	54236.119	2.789	880.0	1.68	0.13	12.75	1.28	0.23
2007052907	54249.311	2.794	1008.0	1.84	0.12	12.40	1.25	0.19
2007061219	54263.818	2.799	1008.0	1.83	0.13	14.31	1.27	0.21
2007062715	54278.669	2.804	768.0	2.09	0.14	11.94	1.41	0.21
2007070423	54285.999	2.806	944.0	2.31	0.13	12.98	1.47	0.19
2007071103	54292.152	2.809	320.0	1.46	0.21	12.24	1.25	0.42
2007071905	54300.239	2.811	1088.0	1.87	0.11	11.57	1.46	0.20
2007072501	54306.055	2.813	880.0	2.05	0.13	12.13	1.46	0.21
2007080208	54314.370	2.816	928.0	1.80	0.13	12.78	1.37	0.22
2007080914	54321.611	2.819	880.0	1.81	0.13	13.33	1.47	0.25
2007081613	54328.577	2.821	944.0	1.70	0.12	12.01	1.45	0.24
2007082302	54335.098	2.823	800.0	2.06	0.13	11.91	1.47	0.22
2007082922	54341.964	2.826	480.0	1.96	0.17	11.68	1.38	0.28
2007090414	54347.607	2.828	928.0	2.33	0.13	13.23	1.58	0.20
2007091217	54355.729	2.831	928.0	2.03	0.13	14.45	1.66	0.25
2007091907	54362.330	2.833	1360.0	2.31	0.10	11.18	1.65	0.16
2007092508	54368.370	2.835	928.0	2.10	0.12	11.81	1.53	0.20
2007100306	54376.266	2.838	880.0	2.14	0.13	13.29	1.95	0.26
2007101005	54383.222	2.840	896.0	2.03	0.13	12.52	1.59	0.23
2007101720	54390.857	2.843	816.0	2.17	0.13	11.78	1.82	0.24
2007121205	54446.231	2.862	704.0	2.48	0.14	11.81	1.97	0.25
2007121905	54453.239	2.864	928.0	1.93	0.13	13.54	1.63	0.25
2007122603	54460.137	2.867	752.0	2.18	0.14	12.75	2.01	0.28
2008010305	54468.223	2.869	912.0	2.70	0.14	14.92	1.90	0.22
2008011003	54475.157	2.872	912.0	2.34	0.13	13.58	1.86	0.23
2008011601	54481.050	2.874	944.0	2.93	0.13	12.06	1.84	0.17
2008012421	54489.899	2.877	928.0	2.38	0.13	12.58	1.93	0.23
2008012914	54494.591	2.879	320.0	2.03	0.21	12.11	1.81	0.42
2008020710	54503.452	2.882	944.0	2.29	0.13	13.15	1.91	0.23
2008021407	54510.316	2.884	896.0	2.27	0.14	14.47	1.89	0.25
2008021905	54515.218	2.886	880.0	2.35	0.14	14.13	1.79	0.23
2008022622	54522.931	2.888	864.0	2.57	0.13	12.06	1.96	0.21
2008030604	54531.198	2.891	928.0	2.73	0.12	11.69	2.25	0.22

Table A1 *continued on next page*

Table A1 *(continued)*

Sequence	MJD	Phase	Expo.	Net Rate	Rate Error	Bkg Rate	Flux	Error
			s	cts/s	cts/s	cts/s	10^{-11} ergs/s/cm^2	10^{-11} ergs/s/cm^2
2008031122	54536.931	2.893	832.0	2.58	0.13	11.12	2.18	0.23
2008032010	54545.438	2.896	256.0	2.21	0.24	12.12	2.14	0.49
2008032415	54549.665	2.898	832.0	2.37	0.13	11.64	1.93	0.23
2008040208	54558.356	2.901	1056.0	2.90	0.12	12.63	2.16	0.19
2008040900	54565.016	2.903	1104.0	2.82	0.12	14.17	2.26	0.21
2008041607	54572.300	2.905	800.0	3.11	0.13	10.99	2.21	0.20
2008042117	54577.722	2.907	384.0	2.95	0.20	12.40	2.05	0.30
2008050112	54587.530	2.911	512.0	2.99	0.17	11.95	2.15	0.26
2008050610	54592.426	2.912	416.0	2.82	0.19	12.07	2.04	0.29
2008051210	54598.452	2.914	992.0	2.65	0.12	12.25	2.22	0.22
2008051919	54605.809	2.917	736.0	2.59	0.15	13.39	2.27	0.27
2008052818	54614.769	2.920	912.0	2.86	0.13	11.92	2.27	0.21
2008060318	54620.761	2.922	1008.0	2.88	0.12	12.81	2.26	0.21
2008060920	54626.844	2.924	912.0	2.92	0.13	11.98	2.34	0.22
2008061713	54634.570	2.927	960.0	3.61	0.13	12.33	2.73	0.20
2008062501	54642.086	2.929	896.0	2.96	0.13	12.20	2.53	0.23
2008070108	54648.370	2.932	784.0	3.10	0.14	11.87	2.64	0.24
2008070804	54655.211	2.934	736.0	3.40	0.15	12.10	2.78	0.24
2008071414	54661.594	2.936	1104.0	3.27	0.12	11.46	2.83	0.20
2008072319	54670.822	2.939	912.0	3.31	0.13	13.21	2.72	0.23
2008080723	54685.994	2.945	1232.0	3.72	0.12	13.40	3.13	0.20
2008080818	54686.775	2.945	736.0	3.76	0.15	12.08	3.20	0.25
2008080922	54687.957	2.945	880.0	3.68	0.14	13.30	3.04	0.23
2008081103	54689.138	2.946	848.0	3.63	0.14	11.91	3.16	0.24
2008081121	54689.882	2.946	640.0	3.88	0.16	13.21	3.16	0.27
2008081221	54690.897	2.946	912.0	3.28	0.14	13.36	2.75	0.23
2008081320	54691.879	2.947	832.0	3.12	0.14	13.29	3.10	0.28
2008081523	54693.973	2.947	800.0	3.50	0.14	11.94	3.09	0.25
2008081723	54696.001	2.948	496.0	3.34	0.18	12.10	3.17	0.34
2008081900	54697.048	2.948	272.0	3.68	0.24	12.57	2.97	0.40
2008081918	54697.794	2.949	1008.0	3.36	0.12	11.88	3.14	0.23
2008082018	54698.786	2.949	944.0	3.99	0.12	10.71	3.25	0.20
2008082114	54699.605	2.949	672.0	3.79	0.16	12.44	3.28	0.27
2008082205	54700.228	2.950	720.0	3.99	0.15	11.93	3.33	0.25
2008082315	54701.644	2.950	896.0	3.88	0.14	13.27	3.31	0.24
2008082414	54702.624	2.950	896.0	3.79	0.14	13.32	3.03	0.22
2008082511	54703.468	2.951	816.0	3.56	0.15	14.01	3.26	0.27
2008082613	54704.584	2.951	928.0	3.57	0.13	13.31	3.21	0.24
2008082713	54705.567	2.951	896.0	4.04	0.14	12.64	3.27	0.22
2008082803	54706.152	2.952	928.0	3.99	0.13	12.18	3.51	0.23
2008082912	54707.526	2.952	928.0	3.74	0.13	13.13	3.25	0.23
2008083010	54708.449	2.952	832.0	3.97	0.13	11.13	3.40	0.23
2008083113	54709.557	2.953	928.0	3.87	0.13	11.76	3.36	0.22
2008090111	54710.470	2.953	976.0	3.88	0.13	12.29	3.22	0.21
2008090213	54711.586	2.953	928.0	3.61	0.13	12.32	3.08	0.23
2008090313	54712.567	2.954	992.0	3.97	0.13	12.18	3.25	0.21
2008090406	54713.284	2.954	944.0	3.96	0.13	11.43	3.20	0.21
2008090509	54714.394	2.954	864.0	4.04	0.13	11.34	3.30	0.22
2008090610	54715.441	2.955	848.0	4.06	0.13	11.26	3.36	0.22
2008090708	54716.357	2.955	880.0	4.21	0.13	11.00	3.28	0.20
2008090812	54717.536	2.956	928.0	3.96	0.14	13.32	3.51	0.24
2008090909	54718.411	2.956	896.0	4.41	0.13	11.55	3.57	0.21

Table A1 *(continued)*

Sequence	MJD	Phase	Expo.	Net Rate	Rate Error	Bkg Rate	Flux	Error
			s	cts/s	cts/s	cts/s	10^{-11} ergs/s/cm^2	10^{-11} ergs/s/cm^2
2008091010	54719.457	2.956	992.0	3.93	0.13	11.76	3.32	0.21
2008091119	54720.812	2.957	752.0	3.98	0.14	11.79	3.40	0.25
2008091212	54721.526	2.957	1104.0	3.90	0.13	13.94	3.20	0.21
2008091311	54722.506	2.957	960.0	3.73	0.14	14.37	3.28	0.24
2008091416	54723.688	2.958	912.0	3.92	0.13	12.32	3.34	0.23
2008091514	54724.602	2.958	1040.0	3.92	0.13	13.30	3.42	0.22
2008091612	54725.515	2.958	1104.0	3.73	0.13	13.81	3.47	0.23
2008091714	54726.629	2.959	912.0	3.77	0.13	12.12	3.21	0.22
2008091811	54727.476	2.959	880.0	4.34	0.14	13.12	3.50	0.22
2008091912	54728.523	2.959	896.0	4.20	0.14	12.65	3.59	0.23
2008092010	54729.455	2.960	912.0	4.38	0.14	12.56	3.75	0.23
2008092113	54730.550	2.960	832.0	3.89	0.14	12.03	3.65	0.26
2008092211	54731.468	2.960	1152.0	4.17	0.12	12.47	3.78	0.21
2008092309	54732.411	2.961	912.0	3.84	0.13	12.31	3.29	0.23
2008092409	54733.392	2.961	912.0	3.96	0.13	12.49	3.45	0.23
2008092503	54734.161	2.961	688.0	4.32	0.15	12.03	3.46	0.24
2008092610	54735.456	2.962	848.0	4.58	0.14	11.98	3.93	0.23
2008092709	54736.402	2.962	1024.0	3.93	0.13	12.20	3.44	0.22
2008092804	54737.170	2.962	192.0	4.14	0.30	12.61	3.65	0.51
2008092904	54738.211	2.963	928.0	4.86	0.14	12.85	3.67	0.20
2008093003	54739.131	2.963	64.0	3.66	0.51	13.14	2.63	0.76
2008100102	54740.111	2.963	160.0	3.64	0.32	13.22	3.63	0.64
2008100205	54741.234	2.964	896.0	4.30	0.14	12.61	3.77	0.24
2008100305	54742.215	2.964	976.0	4.31	0.13	12.65	3.70	0.22
2008100401	54743.051	2.964	112.0	4.32	0.40	13.22	3.90	0.70
2008100502	54744.106	2.965	864.0	4.41	0.14	12.62	3.82	0.24
2008100608	54745.371	2.965	560.0	4.38	0.17	11.53	3.97	0.30
2008100622	54745.924	2.965	496.0	4.55	0.19	12.49	4.04	0.32
2008100803	54747.167	2.966	352.0	4.69	0.21	11.55	4.07	0.36
2008100823	54747.990	2.966	704.0	4.28	0.17	15.10	3.91	0.30
2008101001	54749.077	2.966	832.0	4.19	0.14	12.81	3.73	0.25
2008101100	54750.019	2.967	816.0	4.56	0.15	13.51	4.12	0.26
2008101123	54751.000	2.967	912.0	4.69	0.14	12.75	4.05	0.23
2008101300	54752.047	2.967	912.0	4.90	0.14	11.91	4.37	0.23
2008101323	54752.996	2.968	912.0	4.66	0.14	12.43	4.12	0.23
2008101423	54753.978	2.968	848.0	4.49	0.14	12.70	4.20	0.26
2008101600	54755.028	2.968	832.0	4.94	0.14	12.26	4.20	0.23
2008101709	54756.406	2.969	1168.0	4.73	0.12	12.38	4.09	0.20
2008101812	54757.521	2.969	944.0	4.83	0.13	11.91	4.33	0.23
2008101908	54758.363	2.970	768.0	4.65	0.15	13.44	4.20	0.27
2008102006	54759.289	2.970	912.0	4.96	0.13	11.17	4.39	0.22
2008102110	54760.462	2.970	928.0	5.09	0.13	11.78	4.60	0.23
2008102207	54761.307	2.971	832.0	4.87	0.14	12.34	4.39	0.25
2008102308	54762.354	2.971	896.0	5.06	0.14	11.88	4.51	0.23
2008102509	54764.410	2.972	752.0	5.20	0.15	11.63	4.53	0.25
2008102608	54765.363	2.972	896.0	4.99	0.14	12.00	4.40	0.23
2008102709	54766.412	2.972	880.0	4.78	0.14	13.44	4.43	0.26
2008102807	54767.325	2.973	864.0	5.04	0.14	11.84	4.40	0.23
2008102912	54768.508	2.973	1008.0	5.13	0.14	14.38	4.51	0.24
2008103009	54769.420	2.973	896.0	4.90	0.15	14.84	4.49	0.26
2008103112	54770.536	2.974	816.0	5.13	0.15	13.54	4.54	0.26
2008110110	54771.448	2.974	896.0	5.14	0.15	15.12	4.48	0.25

POLLOCK ET AL.

Table A1 *(continued)*

Sequence	MJD	Phase	Expo.	Net Rate	Rate Error	Bkg Rate	Flux	Error
			s	cts/s	cts/s	cts/s	10^{-11} ergs/s/cm^2	10^{-11} ergs/s/cm^2
2008110211	54772.497	2.975	1056.0	5.08	0.13	13.38	4.52	0.23
2008110307	54773.302	2.975	528.0	5.16	0.18	12.02	4.48	0.30
2008110410	54774.457	2.975	912.0	5.25	0.14	13.38	4.81	0.25
2008110505	54775.239	2.975	896.0	5.35	0.14	12.95	4.84	0.25
2008110607	54776.310	2.976	128.0	6.03	0.38	12.43	4.64	0.55
2008110709	54777.399	2.976	1088.0	5.30	0.13	13.46	4.84	0.23
2008110801	54778.070	2.976	912.0	5.33	0.14	11.91	4.82	0.24
2008110906	54779.251	2.977	48.0	4.80	0.61	13.30	3.85	0.96
2008111007	54780.304	2.977	960.0	4.71	0.13	12.53	4.29	0.24
2008111103	54781.144	2.978	368.0	5.66	0.22	12.51	4.56	0.34
2008111208	54782.368	2.978	864.0	5.67	0.14	12.01	4.95	0.23
2008111310	54783.435	2.978	896.0	5.66	0.14	11.27	4.81	0.22
2008111403	54784.152	2.979	16.0	5.00	1.02	11.69	3.35	1.34
2008111505	54785.254	2.979	848.0	5.94	0.15	12.09	5.04	0.23
2008111604	54786.187	2.979	912.0	5.51	0.14	12.55	4.83	0.23
2008111707	54787.303	2.980	1104.0	5.51	0.13	12.24	5.01	0.22
2008111804	54788.196	2.980	896.0	6.07	0.14	12.29	5.28	0.23
2008111902	54789.128	2.980	944.0	5.67	0.14	12.81	5.21	0.24
2008112000	54790.032	2.981	16.0	7.11	1.12	13.14	4.80	1.42
2008112103	54791.157	2.981	1120.0	5.73	0.13	12.37	5.27	0.22
2008112201	54792.068	2.981	928.0	5.64	0.14	12.60	5.10	0.24
2008112301	54793.049	2.982	928.0	5.73	0.14	12.36	4.89	0.22
2008112403	54794.167	2.982	944.0	5.49	0.14	12.41	5.26	0.25
2008112503	54795.145	2.982	1424.0	5.84	0.11	11.99	5.36	0.19
2008112601	54796.059	2.983	912.0	5.88	0.14	12.41	5.46	0.25
2008112702	54797.106	2.983	944.0	6.01	0.14	12.49	5.61	0.24
2008112801	54798.072	2.983	1040.0	6.18	0.13	11.65	5.47	0.21
2008112823	54799.000	2.984	848.0	5.89	0.15	12.64	5.53	0.26
2008112921	54799.910	2.984	976.0	6.03	0.14	12.54	5.33	0.23
2008120110	54801.424	2.985	832.0	5.91	0.15	13.11	5.50	0.26
2008120212	54802.543	2.985	848.0	6.61	0.15	12.10	5.83	0.24
2008120310	54803.454	2.985	944.0	5.74	0.14	12.03	5.41	0.24
2008120410	54804.434	2.986	928.0	6.37	0.14	11.96	6.02	0.24
2008120509	54805.414	2.986	896.0	6.14	0.14	11.84	5.40	0.23
2008120606	54806.265	2.986	1072.0	5.78	0.13	11.75	5.55	0.23
2008120710	54807.444	2.987	880.0	6.48	0.15	12.53	5.57	0.23
2008120808	54808.355	2.987	944.0	6.28	0.14	11.88	5.61	0.23
2008120905	54809.226	2.987	1104.0	6.14	0.13	12.82	5.43	0.22
2008121012	54810.520	2.988	944.0	6.45	0.15	14.62	5.20	0.23
2008121106	54811.295	2.988	944.0	6.47	0.14	11.84	5.33	0.21
2008121204	54812.171	2.988	704.0	5.80	0.17	13.49	5.12	0.28
2008121307	54813.324	2.989	944.0	6.06	0.14	12.63	4.89	0.21
2008121410	54814.441	2.989	864.0	6.50	0.16	15.47	4.94	0.23
2008121513	54815.557	2.989	896.0	6.01	0.15	13.07	4.46	0.21
2008121604	54816.199	2.990	1152.0	6.20	0.12	11.62	4.75	0.18
2008121705	54817.245	2.990	896.0	5.22	0.14	13.27	4.11	0.22
2008121809	54818.384	2.990	784.0	5.47	0.15	12.34	3.88	0.21
2008121905	54819.234	2.991	816.0	5.56	0.15	11.68	4.11	0.20
2008122000	54820.014	2.991	912.0	5.39	0.14	12.63	3.77	0.19
2008122105	54821.234	2.991	896.0	5.14	0.15	15.16	3.74	0.21
2008122203	54822.149	2.992	864.0	4.90	0.14	12.37	3.38	0.19
2008122303	54823.156	2.992	672.0	5.71	0.16	11.93	3.77	0.21

Table A1 *(continued)*

Sequence	MJD	Phase	Expo.	Net Rate	Rate Error	Bkg Rate	Flux	Error
			s	cts/s	cts/s	cts/s	10^{-11} ergs/s/cm^2	10^{-11} ergs/s/cm^2
2008122403	54824.136	2.992	672.0	5.22	0.16	12.09	3.59	0.21
2008122504	54825.182	2.993	432.0	4.79	0.20	12.72	3.36	0.28
2008122603	54826.164	2.993	128.0	5.26	0.38	12.88	3.74	0.52
2008122709	54827.385	2.993	912.0	4.89	0.14	11.92	3.36	0.18
2008122803	54828.166	2.994	848.0	5.04	0.15	13.57	3.61	0.21
2008122904	54829.214	2.994	1152.0	3.94	0.13	14.37	3.12	0.20
2008123004	54830.194	2.994	864.0	4.81	0.14	13.07	3.32	0.20
2008123102	54831.109	2.995	848.0	4.76	0.15	13.20	3.27	0.20
2009010104	54832.186	2.995	864.0	4.45	0.14	12.17	3.03	0.19
2009010105	54832.186	2.995	864.0	4.45	0.14	12.17	3.03	0.19
2009010204	54833.203	2.996	1056.0	4.44	0.13	12.37	2.94	0.17
2009010304	54834.183	2.996	832.0	4.29	0.14	12.03	2.69	0.18
2009010405	54835.229	2.996	848.0	3.49	0.13	11.76	2.31	0.18
2009010503	54836.145	2.997	816.0	3.46	0.14	12.17	2.29	0.19
2009010600	54837.020	2.997	880.0	2.98	0.13	12.83	1.94	0.19
2009010704	54838.202	2.997	768.0	3.09	0.14	12.45	1.85	0.19
2009010800	54839.022	2.998	832.0	3.12	0.14	12.72	1.92	0.18
2009010901	54840.069	2.998	768.0	2.61	0.14	11.84	1.49	0.18
2009011001	54841.053	2.998	944.0	2.71	0.12	11.76	1.55	0.16
2009011102	54842.096	2.999	784.0	2.49	0.13	11.38	1.39	0.17
2009011123	54842.971	2.999	832.0	2.05	0.13	12.50	0.93	0.15
2009011310	54844.451	2.999	704.0	1.43	0.14	13.09	0.72	0.20
2009011408	54845.367	3.000	560.0	1.43	0.15	11.70	0.55	0.18
2009011508	54846.374	3.000	1216.0	1.04	0.11	13.18	0.54	0.18
2009011608	54847.354	3.000	992.0	1.22	0.12	13.44	0.48	0.16
2009011712	54848.542	3.001	848.0	1.15	0.13	12.70	0.55	0.19
2009011807	54849.316	3.001	1104.0	1.04	0.11	12.97	0.43	0.16
2009011908	54850.365	3.001	896.0	1.44	0.12	11.90	0.53	0.14
2009012006	54851.275	3.002	992.0	1.18	0.12	13.34	0.37	0.14
2009012105	54852.255	3.002	880.0	0.96	0.13	13.60	0.33	0.18
2009012212	54853.510	3.003	848.0	0.79	0.13	14.31	0.30	0.21
2009012306	54854.286	3.003	944.0	1.24	0.12	11.87	0.45	0.14
2009012407	54855.335	3.003	880.0	0.87	0.12	11.80	0.27	0.16
2009012507	54856.333	3.003	640.0	1.06	0.14	11.56	0.41	0.19
2009012610	54857.431	3.004	896.0	1.32	0.13	13.73	0.38	0.14
2009012711	54858.480	3.004	1024.0	1.15	0.12	14.53	0.40	0.16
2009012807	54859.326	3.005	1344.0	0.96	0.10	13.63	0.40	0.16
2009012912	54860.507	3.005	912.0	1.43	0.13	13.70	0.36	0.12
2009013011	54861.487	3.005	992.0	1.29	0.12	13.91	0.45	0.15
2009013111	54862.467	3.006	848.0	1.10	0.13	14.06	0.47	0.19
2009020105	54863.244	3.006	880.0	1.13	0.13	14.65	0.44	0.18
2009020211	54864.496	3.006	1152.0	1.31	0.11	12.53	0.53	0.14
2009020309	54865.410	3.007	1392.0	1.32	0.11	14.06	0.60	0.15
2009020410	54866.458	3.007	1312.0	1.63	0.10	12.50	0.68	0.12
2009020503	54867.164	3.007	896.0	1.92	0.13	13.69	0.85	0.16
2009020609	54868.416	3.008	928.0	2.04	0.12	12.37	0.97	0.15
2009020703	54869.151	3.008	704.0	2.09	0.14	12.34	0.99	0.17
2009020801	54870.067	3.008	640.0	2.35	0.15	11.73	1.20	0.18
2009021304	54875.210	3.010	1152.0	3.24	0.12	12.97	1.86	0.15
2009021401	54876.057	3.010	1136.0	2.99	0.12	14.42	1.64	0.15
2009021503	54877.169	3.011	1024.0	3.01	0.12	12.77	1.66	0.15
2009021603	54878.149	3.011	912.0	2.84	0.13	13.02	1.78	0.18

Table A1 *continued on next page*

Pollock et al.

Table A1 *(continued)*

Sequence	MJD	Phase	Expo.	Net Rate	Rate Error	Bkg Rate	Flux	Error
			s	cts/s	cts/s	cts/s	10^{-11} ergs/s/cm^2	10^{-11} ergs/s/cm^2
2009021702	54879.129	3.011	896.0	2.98	0.13	12.54	1.80	0.17
2009021804	54880.176	3.012	848.0	3.01	0.13	11.83	1.85	0.18
2009021901	54881.055	3.012	896.0	3.22	0.13	12.35	1.82	0.16
2009022002	54882.101	3.012	944.0	3.40	0.13	11.84	2.02	0.16
2009022103	54883.148	3.013	800.0	3.33	0.14	12.11	2.06	0.18
2009022204	54884.193	3.013	704.0	3.56	0.15	12.56	2.20	0.20
2009022300	54885.044	3.013	928.0	3.90	0.13	12.25	2.32	0.16
2009022400	54886.025	3.014	960.0	3.42	0.13	12.52	2.11	0.17
2009022510	54887.440	3.014	1040.0	3.44	0.13	13.42	2.27	0.18
2009022511	54887.440	3.014	1040.0	3.44	0.13	13.42	2.27	0.18
2009022611	54888.487	3.015	928.0	3.63	0.13	13.07	2.35	0.18
2009022700	54889.034	3.015	672.0	3.56	0.16	12.59	2.30	0.21
2009022813	54890.581	3.015	880.0	4.09	0.14	11.96	2.51	0.17
2009030109	54891.363	3.016	496.0	3.84	0.18	12.21	2.27	0.22
2009030208	54892.372	3.016	688.0	3.41	0.16	13.42	2.29	0.22
2009030308	54893.352	3.016	864.0	3.73	0.14	12.88	2.27	0.18
2009030410	54894.435	3.017	912.0	3.73	0.13	11.81	2.49	0.18
2009030509	54895.382	3.017	880.0	3.60	0.13	11.98	2.51	0.19
2009030609	54896.396	3.017	704.0	3.66	0.15	12.06	2.51	0.21
2009030610	54896.396	3.017	704.0	3.66	0.15	12.06	2.51	0.21
2009030703	54897.136	3.018	944.0	3.71	0.14	14.01	2.54	0.19
2009030801	54898.069	3.018	608.0	3.73	0.16	11.50	2.59	0.22
2009030907	54899.303	3.018	880.0	3.72	0.13	11.67	2.57	0.19
2009031004	54900.214	3.019	1040.0	3.72	0.12	12.48	2.58	0.18
2009031101	54901.049	3.019	944.0	3.78	0.13	12.74	2.54	0.18
2009031205	54902.244	3.019	896.0	3.76	0.13	11.59	2.56	0.18
2009031300	54903.018	3.020	1056.0	3.49	0.13	13.83	2.43	0.19
2009031403	54904.134	3.020	928.0	3.35	0.13	12.58	2.50	0.20
2009031504	54905.184	3.020	832.0	3.73	0.14	11.77	2.59	0.19
2009031602	54906.095	3.021	912.0	3.76	0.13	12.17	2.60	0.19
2009031701	54907.075	3.021	896.0	4.04	0.14	12.36	2.87	0.19
2009031801	54908.054	3.021	848.0	3.95	0.14	12.30	2.69	0.19
2009031900	54909.035	3.022	896.0	3.80	0.13	12.47	2.73	0.20
2009032001	54910.084	3.022	912.0	4.12	0.13	11.77	2.74	0.18
2009032106	54911.268	3.022	912.0	3.71	0.14	15.02	2.72	0.22
2009032207	54912.316	3.023	912.0	3.86	0.14	14.21	2.71	0.20
2009032300	54913.024	3.023	944.0	3.59	0.13	12.13	2.72	0.20
2009033120	54921.850	3.026	992.0	3.71	0.12	11.71	2.70	0.18
2009040622	54927.931	3.028	880.0	3.62	0.15	14.92	2.70	0.22
2009041518	54936.762	3.031	880.0	4.08	0.14	12.91	2.82	0.19
2009042218	54943.783	3.034	16.0	3.65	1.01	12.60	4.17	2.25
2009043007	54951.315	3.036	992.0	3.11	0.14	15.35	2.41	0.22
2009050712	54958.514	3.039	912.0	3.22	0.13	11.62	2.58	0.21
2009051407	54965.303	3.041	848.0	2.99	0.13	11.87	2.41	0.22
2009052119	54972.808	3.044	928.0	3.19	0.13	13.55	2.42	0.21
2009052819	54979.805	3.046	880.0	3.16	0.14	13.22	2.55	0.23
2009060323	54985.978	3.048	880.0	3.21	0.13	12.34	2.46	0.21
2009061118	54993.798	3.051	656.0	2.99	0.15	11.37	2.32	0.24
2009061704	54999.199	3.053	832.0	3.05	0.15	14.58	2.49	0.25
2009062318	55005.783	3.055	864.0	3.21	0.14	13.46	2.44	0.22
2009070220	55014.880	3.058	896.0	2.65	0.14	13.74	2.08	0.23
2009070915	55021.671	3.061	832.0	2.22	0.14	13.57	2.20	0.29

Table A1 *(continued)*

Sequence	MJD	Phase	Expo.	Net Rate	Rate Error	Bkg Rate	Flux	Error
			s	cts/s	cts/s	cts/s	10^{-11} ergs/s/cm^2	10^{-11} ergs/s/cm^2
2009071615	55028.668	3.063	912.0	2.48	0.13	14.14	2.10	0.25
2009072210	55034.440	3.065	432.0	2.63	0.19	12.21	2.14	0.32
2009073011	55042.492	3.068	912.0	2.44	0.13	12.58	2.00	0.23
2009080500	55048.026	3.070	800.0	2.41	0.13	12.17	2.15	0.26
2009081308	55056.372	3.073	752.0	2.46	0.14	11.72	2.06	0.25
2009081914	55062.626	3.075	1104.0	2.38	0.11	11.78	2.10	0.21
2009082715	55070.670	3.078	896.0	2.79	0.14	15.41	2.30	0.25
2009090111	55075.503	3.079	896.0	2.33	0.14	14.38	1.80	0.23
2009091723	55091.988	3.085	912.0	2.35	0.13	12.24	1.89	0.22
2009100621	55110.915	3.091	976.0	2.35	0.13	13.04	1.84	0.22
2009101409	55118.414	3.094	944.0	2.54	0.13	12.52	1.83	0.20
2009102209	55126.391	3.097	928.0	1.91	0.13	14.57	1.79	0.28
2009110515	55140.643	3.102	800.0	2.04	0.14	14.50	1.51	0.25
2009111118	55146.794	3.104	880.0	2.12	0.13	11.99	1.68	0.23
2009111814	55153.622	3.106	896.0	2.05	0.13	12.10	1.89	0.25
2009112606	55161.271	3.109	896.0	2.06	0.12	11.30	1.62	0.22
2009120110	55166.429	3.111	1072.0	1.97	0.12	14.07	1.72	0.24
2009121021	55175.918	3.114	1392.0	1.84	0.10	13.40	1.69	0.22
2009121609	55181.418	3.116	832.0	2.03	0.13	11.52	1.61	0.23
2009122403	55189.137	3.118	880.0	2.06	0.13	12.69	1.57	0.23
2009123023	55195.995	3.121	992.0	2.25	0.12	12.56	1.71	0.21
2010010805	55204.242	3.124	1824.0	2.15	0.09	11.81	1.65	0.15
2010012306	55219.270	3.129	944.0	2.00	0.13	14.50	1.65	0.25
2010020604	55233.210	3.134	448.0	1.98	0.18	11.78	1.41	0.29
2010022107	55248.318	3.139	896.0	1.73	0.13	13.66	1.56	0.27
2010030710	55262.446	3.144	1008.0	1.79	0.13	14.30	1.50	0.25
2010032020	55275.853	3.148	880.0	2.00	0.13	12.03	1.55	0.22
2010040223	55288.996	3.153	880.0	1.60	0.13	12.23	1.22	0.23
2010041707	55303.319	3.158	1008.0	1.59	0.12	13.32	1.32	0.24
2010082217	55430.714	3.202	928.0	1.47	0.12	12.78	1.24	0.25
2010090403	55443.136	3.206	1056.0	1.75	0.11	11.82	1.31	0.20
2010091723	55456.987	3.211	896.0	1.50	0.12	12.25	1.16	0.23
2010100112	55470.528	3.216	1136.0	1.58	0.11	13.09	1.27	0.22
2010101512	55484.507	3.220	912.0	1.54	0.13	12.80	1.13	0.23
2010103015	55499.665	3.226	832.0	1.45	0.13	13.32	1.24	0.28
2010111221	55512.904	3.230	1216.0	1.51	0.10	11.60	1.18	0.20
2010112610	55526.431	3.235	736.0	1.84	0.14	12.44	1.17	0.22
2010121007	55540.319	3.240	864.0	1.30	0.12	11.73	1.22	0.28
2010122417	55554.731	3.245	688.0	1.23	0.16	15.74	1.10	0.35
2011010800	55569.042	3.250	800.0	1.14	0.14	13.49	1.02	0.31
2011012300	55584.044	3.255	880.0	1.74	0.13	13.29	1.22	0.22
2011020500	55597.003	3.259	736.0	2.22	0.14	12.33	1.36	0.20
2011021815	55610.636	3.264	1008.0	1.42	0.12	12.40	0.99	0.21
2011030503	55625.147	3.269	880.0	1.41	0.13	14.25	1.03	0.25
2011031803	55638.168	3.274	688.0	1.57	0.14	11.70	1.20	0.26
2011040107	55652.313	3.278	816.0	1.51	0.13	11.82	1.09	0.23
2011041521	55666.917	3.283	768.0	1.23	0.13	12.65	0.92	0.26
2011043003	55681.131	3.288	944.0	1.28	0.12	11.54	0.89	0.21
2011051316	55694.703	3.293	880.0	1.65	0.13	12.39	0.95	0.19
2011052710	55708.456	3.298	608.0	1.46	0.15	12.25	0.94	0.25
2011061017	55722.753	3.303	800.0	1.64	0.13	11.77	1.03	0.20
2011062419	55736.827	3.308	944.0	1.49	0.12	11.64	1.05	0.21

Table A1 *(continued)*

Sequence	MJD	Phase	Expo.	Net Rate	Rate Error	Bkg Rate	Flux	Error
			s	cts/s	cts/s	cts/s	10^{-11} ergs/s/cm^2	10^{-11} ergs/s/cm^2
2011070812	55750.535	3.312	944.0	1.83	0.12	11.58	1.04	0.17
2011072400	55766.037	3.318	1088.0	1.33	0.12	13.58	1.00	0.23
2011080514	55778.615	3.322	848.0	1.43	0.14	14.59	1.05	0.25
2011082009	55793.388	3.327	800.0	1.50	0.13	12.35	1.00	0.22
2011090406	55808.287	3.332	400.0	1.21	0.18	11.32	0.93	0.35
2011091611	55820.490	3.337	800.0	1.77	0.13	12.13	1.15	0.21
2011093003	55834.168	3.341	944.0	2.01	0.12	10.97	1.27	0.18
2011101601	55850.083	3.347	816.0	1.39	0.13	12.76	1.03	0.25
2011102723	55861.997	3.351	912.0	1.62	0.12	11.35	1.18	0.21
2011111106	55876.279	3.356	816.0	1.48	0.13	11.27	0.96	0.21
2011112506	55890.268	3.361	832.0	1.35	0.13	12.74	0.88	0.22
2011120914	55904.610	3.366	704.0	1.25	0.14	12.04	1.08	0.30
2011122315	55918.656	3.370	1328.0	1.60	0.10	12.15	1.11	0.17

Table A2. Log of *SWIFT* Observations and Fluxes

Sequence	MJD	Phase	Expo.	Net Rate	Rate Error	Bkg Rate	Flux	Error	Mode
			s	cts/s	cts/s	cts/s	10^{-11} ergs/s/cm^2	10^{-11} ergs/s/cm^2	
31251001	54689.231	2.946	1379.0	0.967	0.027	0.004	2.477	0.068	pc
31251002	54690.330	2.946	3876.3	0.970	0.016	0.004	2.555	0.042	pc
31251003	54692.603	2.947	516.5	0.917	0.042	0.003	2.395	0.110	pc
31251004	54694.710	2.948	3658.2	0.952	0.016	0.004	2.470	0.042	pc
31251005	54696.218	2.948	3738.4	0.973	0.016	0.004	2.594	0.043	pc
31251006	54698.305	2.949	3811.1	0.861	0.015	0.004	2.484	0.044	pc
31251007	54700.444	2.950	1028.0	0.836	0.029	0.003	2.678	0.092	pc
31251008	54702.340	2.950	2346.8	1.028	0.021	0.004	2.817	0.058	pc
31251009	54709.283	2.953	5731.7	1.046	0.014	0.004	2.712	0.035	pc
31251010	54802.115	2.985	2838.3	1.113	0.020	0.004	4.026	0.072	pc
31251011	54803.926	2.985	1043.0	0.805	0.028	0.003	3.714	0.129	pc
31251012	54804.889	2.986	707.1	0.971	0.037	0.003	4.059	0.155	pc
31251013	54805.830	2.986	1722.5	0.821	0.022	0.003	3.934	0.105	pc
31251014	54806.864	2.986	1785.2	0.921	0.023	0.003	4.031	0.100	pc
31251015	54807.940	2.987	2271.6	0.893	0.020	0.003	4.322	0.096	pc
31251016	54808.876	2.987	1963.2	0.763	0.020	0.003	3.922	0.102	pc
31251017	54809.914	2.987	1953.2	0.701	0.019	0.003	3.433	0.093	pc
31251018	54810.688	2.988	2073.5	0.750	0.019	0.003	4.218	0.107	pc
31251019	54811.957	2.988	1170.9	0.551	0.022	0.002	3.146	0.124	pc
31251020	54812.494	2.988	1885.5	0.642	0.019	0.003	4.252	0.123	pc
31251021	54813.897	2.989	3036.3	0.456	0.012	0.003	3.612	0.098	pc
31251022	54814.506	2.989	2281.6	0.693	0.017	0.003	4.057	0.102	pc
31251023	54815.542	2.989	2512.3	0.563	0.015	0.002	3.997	0.107	pc
31251024	54816.678	2.990	3094.0	0.447	0.012	0.003	3.245	0.088	pc
31251025	54817.518	2.990	3259.5	0.435	0.012	0.003	3.649	0.097	pc
31251026	54818.958	2.991	2043.4	0.434	0.015	0.003	3.203	0.108	pc
31251028	54820.392	2.991	957.8	0.360	0.019	0.002	3.202	0.173	pc
31251029	54821.142	2.991	952.8	0.323	0.018	0.001	2.851	0.163	pc
31251032	54824.542	2.993	1785.2	0.301	0.013	0.002	3.200	0.139	pc
31251033	54826.548	2.993	1138.3	0.267	0.015	0.002	3.340	0.193	pc

Sequence	MJD	Phase	Expo.	Net Rate	Rate Error	Bkg Rate	Flux	Error	Mode
			s	cts/s	cts/s	cts/s	10^{-11} ergs/s/cm^2	10^{-11} ergs/s/cm^2	
31251034	54826.946	2.993	1855.4	0.332	0.013	0.002	3.223	0.131	pc
31251035	54828.588	2.994	2018.4	0.296	0.012	0.002	2.900	0.119	pc
31251036	54829.325	2.994	2056.0	0.265	0.011	0.002	3.200	0.138	pc
31251037	54830.399	2.995	2158.8	0.288	0.012	0.002	3.238	0.131	pc
31251038	54831.099	2.995	2299.2	0.285	0.011	0.002	3.158	0.124	pc
90029001	54834.446	2.996	19760.0	0.210	0.003	0.002	2.323	0.036	pc
31251039	54840.473	2.998	5019.6	0.119	0.005	0.002	1.758	0.073	pc
31251040	54841.276	2.998	4508.1	0.104	0.005	0.002	1.623	0.076	pc
31251041	54842.854	2.999	3878.9	0.085	0.006	0.072	1.045	0.167	wt
31251042	54843.796	2.999	3695.9	0.104	0.007	0.061	0.831	0.123	wt
31251043	54844.821	3.000	2396.0	0.060	0.008	0.078	0.417	0.193	wt
31251044	54845.225	3.000	4100.1	0.072	0.006	0.054	0.325	0.104	wt
31251045	54846.593	3.000	4492.2	0.032	0.005	0.069	0.157	0.183	wt
31251046	54847.595	3.000	4709.2	0.079	0.006	0.079	0.204	0.091	wt
90029003	54874.577	3.010	18647.8	0.153	0.003	0.045	1.428	0.053	wt
90029004	54902.318	3.019	9662.0	0.355	0.007	0.073	2.483	0.067	wt
90029005	54917.520	3.025	9679.3	0.412	0.007	0.080	2.773	0.067	wt
91396001	56024.536	3.407	4152.1	0.324	0.009	0.002	0.985	0.027	pc
91396002	56052.230	3.417	2567.5	0.405	0.013	0.003	0.918	0.029	pc
91396003	56056.573	3.418	1592.1	0.443	0.017	0.002	1.052	0.040	pc
91396004	56080.678	3.426	3482.6	0.300	0.009	0.002	0.924	0.029	pc
91396005	56108.902	3.436	3106.5	0.416	0.012	0.003	0.932	0.026	pc
91396006	56112.047	3.437	975.3	0.275	0.017	0.001	0.939	0.058	pc
91396007	56136.900	3.446	4071.9	0.322	0.009	0.002	1.125	0.031	pc
91396008	56164.501	3.455	3908.9	0.424	0.010	0.002	0.975	0.024	pc
91396009	56192.490	3.465	4723.8	0.409	0.009	0.003	0.891	0.020	pc
91396010	56220.343	3.475	3806.1	0.391	0.010	0.002	0.965	0.025	pc
91396011	56248.138	3.484	4039.3	0.414	0.010	0.003	0.973	0.024	pc
91396012	56276.888	3.494	3382.3	0.310	0.010	0.002	0.953	0.030	pc
91396013	56304.112	3.504	3485.1	0.325	0.010	0.002	1.034	0.031	pc
91396014	56332.373	3.513	3788.5	0.407	0.010	0.002	1.049	0.027	pc
91396015	56360.143	3.523	3923.9	0.408	0.010	0.002	0.969	0.024	pc
31251047	57238.953	3.827	1818.3	1.092	0.025	0.038	1.418	0.052	wt
31251048	57245.864	3.829	1882.6	0.950	0.023	0.086	1.397	0.056	wt
31251049	57252.443	3.831	1222.4	0.920	0.028	0.066	1.427	0.071	wt
31251050	57259.524	3.834	1525.2	0.896	0.025	0.072	1.709	0.073	wt
31251052	57270.784	3.837	432.8	1.011	0.050	0.072	1.451	0.115	wt
31251053	57273.913	3.839	968.6	1.093	0.035	0.083	1.642	0.081	wt
31251054	57275.401	3.839	1327.1	0.852	0.027	0.089	1.275	0.068	wt
31251055	57280.816	3.841	639.5	1.109	0.043	0.060	1.731	0.100	wt
31251056	57287.961	3.843	1731.9	1.077	0.026	0.073	1.362	0.053	wt
31251057	57294.416	3.846	2060.6	1.046	0.023	0.072	1.264	0.047	wt
31251058	57301.637	3.848	1159.3	1.014	0.030	0.042	1.945	0.083	wt
31251059	57305.016	3.849	800.5	1.071	0.038	0.061	1.634	0.088	wt
31251060	57308.074	3.850	1016.1	1.113	0.034	0.061	1.510	0.072	wt
31251061	57315.760	3.853	1887.7	1.095	0.025	0.050	1.595	0.055	wt
31251062	57322.115	3.855	504.4	1.124	0.048	0.042	1.805	0.113	wt
31251063	57325.713	3.856	1499.4	1.111	0.028	0.079	1.442	0.059	wt
31251064	57329.491	3.858	286.6	0.881	0.057	0.052	1.155	0.130	wt
31251065	57336.908	3.860	1541.4	0.754	0.023	0.075	1.608	0.077	wt
31251066	57343.952	3.863	1923.5	0.526	0.018	0.117	1.710	0.095	wt
31251067	57350.865	3.865	1937.2	1.158	0.025	0.075	1.895	0.061	wt

Table A2 *(continued)*

Sequence	MJD	Phase	Expo.	Net Rate	Rate Error	Bkg Rate	Flux	Error	Mode
			s	cts/s	cts/s	cts/s	10^{-11} ergs/s/cm^2	10^{-11} ergs/s/cm^2	
31251068	57357.681	3.868	1885.0	0.972	0.024	0.095	1.815	0.067	wt
31251069	57364.958	3.870	1079.0	0.819	0.029	0.098	1.620	0.091	wt
31251070	57371.950	3.872	1786.9	1.069	0.025	0.072	1.852	0.065	wt
31251071	57378.326	3.875	1389.0	1.084	0.029	0.089	2.128	0.081	wt
31251072	57385.912	3.877	1883.6	1.024	0.024	0.079	1.878	0.066	wt
31251073	57392.620	3.880	1950.6	1.122	0.025	0.087	1.967	0.064	wt
31251074	57399.470	3.882	1901.4	1.266	0.027	0.084	2.042	0.062	wt
31251075	57406.750	3.884	185.2	1.173	0.081	0.038	2.341	0.220	wt
31251076	57410.870	3.886	878.5	1.278	0.039	0.080	3.900	0.149	wt
31251077	57413.823	3.887	2025.7	1.276	0.026	0.073	2.056	0.059	wt
31251078	57420.274	3.889	1857.9	1.196	0.026	0.095	1.937	0.063	wt
31251079	57427.396	3.892	1889.6	1.217	0.026	0.072	1.876	0.059	wt
31251080	57434.410	3.894	1942.4	1.348	0.027	0.083	2.210	0.062	wt
31251081	57441.614	3.897	1899.0	1.291	0.027	0.089	2.038	0.061	wt
31251082	57448.495	3.899	1468.7	0.880	0.026	0.089	1.979	0.085	wt
31251083	57455.269	3.901	455.4	1.102	0.051	0.081	1.968	0.132	wt
31251084	57456.739	3.902	846.9	1.412	0.042	0.073	2.347	0.096	wt
31251085	57462.750	3.904	1588.5	1.159	0.028	0.060	2.430	0.079	wt
31251086	57469.761	3.906	1635.0	1.159	0.027	0.045	2.153	0.070	wt
31251087	57476.256	3.908	1448.8	1.262	0.030	0.083	2.394	0.080	wt
31251088	57483.554	3.911	1949.1	1.420	0.028	0.082	2.233	0.061	wt
31251089	57490.735	3.913	1759.9	1.425	0.029	0.071	2.295	0.065	wt
31251090	57497.052	3.916	1897.0	1.485	0.028	0.055	2.466	0.064	wt
31251091	57504.201	3.918	616.7	1.543	0.051	0.071	2.789	0.122	wt
31251092	57507.954	3.919	1368.3	1.244	0.031	0.107	2.510	0.087	wt
31251093	57511.033	3.920	1687.7	1.452	0.030	0.065	2.235	0.064	wt
31251094	57518.280	3.923	1057.9	1.453	0.038	0.091	2.641	0.093	wt
31251095	57526.800	3.926	1273.6	1.415	0.035	0.106	2.767	0.090	wt
31251096	57532.511	3.928	1646.0	1.272	0.029	0.080	2.698	0.081	wt
31251097	57539.456	3.930	1774.1	1.557	0.031	0.113	2.474	0.067	wt
31251098	57546.369	3.933	1944.6	1.576	0.029	0.083	2.702	0.067	wt
31251099	57552.748	3.935	2183.8	1.700	0.028	0.052	2.730	0.060	wt
31251100	57560.045	3.937	1484.6	1.078	0.029	0.144	1.994	0.079	wt
31251101	57570.380	3.941	1537.2	0.809	0.025	0.152	2.318	0.104	wt
31251104	57580.100	3.944	1107.4	1.754	0.042	0.175	2.930	0.093	wt
31251105	57583.124	3.945	1622.9	1.382	0.031	0.149	2.755	0.083	wt
31251106	57587.177	3.947	1846.8	1.724	0.032	0.206	3.279	0.081	wt
31251107	57591.527	3.948	1945.7	1.841	0.032	0.140	3.290	0.073	wt
31251109	57599.263	3.951	1283.5	1.474	0.036	0.193	3.285	0.106	wt
31251110	57608.006	3.954	682.5	1.836	0.054	0.188	3.533	0.134	wt
31251111	57611.648	3.955	1311.4	1.476	0.036	0.181	3.271	0.103	wt
31251112	57615.067	3.956	1900.4	1.301	0.029	0.246	3.969	0.113	wt
31251113	57622.288	3.959	79.2	1.909	0.160	0.126	5.206	0.520	wt
31251114	57623.817	3.959	261.2	1.906	0.090	0.192	3.327	0.203	wt
31251115	57625.644	3.960	1271.9	1.740	0.040	0.292	3.671	0.110	wt
31251116	57627.496	3.961	1786.1	1.848	0.035	0.298	4.039	0.097	wt
31251117	57631.671	3.962	734.4	1.952	0.054	0.183	4.298	0.147	wt
31251118	57635.206	3.963	1118.5	1.719	0.041	0.205	4.243	0.128	wt
31251119	57639.677	3.965	1769.9	1.748	0.033	0.167	3.768	0.090	wt
31251120	57643.628	3.966	978.8	2.148	0.049	0.163	4.359	0.121	wt
31251121	57647.707	3.968	1926.7	2.196	0.035	0.162	4.190	0.082	wt
31251122	57651.325	3.969	1987.1	2.232	0.035	0.212	4.386	0.085	wt

Table A2 *continued on next page*

Table A2 *(continued)*

Sequence	MJD	Phase	Expo.	Net Rate	Rate Error	Bkg Rate	Flux	Error	Mode
			s	cts/s	cts/s	cts/s	10^{-11} ergs/s/cm^2	10^{-11} ergs/s/cm^2	
31251123	57654.748	3.970	707.5	2.060	0.056	0.164	4.365	0.146	wt
31251124	57655.388	3.970	1893.0	2.224	0.036	0.198	4.316	0.086	wt
31251125	57659.135	3.972	1190.4	2.322	0.046	0.186	4.563	0.110	wt
31251126	57663.116	3.973	1951.6	2.271	0.035	0.177	4.675	0.088	wt
31251127	57667.234	3.974	775.4	1.768	0.050	0.182	5.848	0.197	wt
31251128	57671.422	3.976	2089.3	2.427	0.035	0.186	5.529	0.096	wt
31251129	57675.508	3.977	958.4	2.220	0.050	0.206	5.297	0.144	wt
31251130	57678.913	3.978	210.6	2.325	0.109	0.171	5.065	0.284	wt
31251131	57679.878	3.979	684.5	2.183	0.059	0.162	4.848	0.157	wt
31251132	57683.727	3.980	2710.0	2.088	0.029	0.171	5.479	0.090	wt
31251133	57685.483	3.981	2959.4	0.052	0.006	0.070	6.413	1.123	wt
31251134	57688.312	3.982	3188.5	2.302	0.028	0.222	5.922	0.086	wt
31251135	57689.711	3.982	1961.9	1.683	0.030	0.114	5.521	0.117	wt
31251136	57691.238	3.983	3731.3	2.197	0.026	0.237	5.483	0.077	wt
31251137	57693.449	3.983	3382.1	2.224	0.027	0.157	6.922	0.095	wt
31251138	57695.874	3.984	2625.0	2.194	0.030	0.208	5.675	0.093	wt
31251139	57697.739	3.985	3985.3	2.195	0.025	0.243	6.173	0.082	wt
31251140	57699.131	3.985	2664.3	1.448	0.025	0.243	5.848	0.124	wt
31251141	57701.688	3.986	3514.3	1.688	0.023	0.227	5.438	0.091	wt
31251142	57703.745	3.987	3817.6	1.625	0.022	0.168	5.450	0.087	wt
31251143	57705.651	3.988	3210.9	1.283	0.022	0.215	5.681	0.117	wt
31251144	57707.863	3.988	3900.6	1.197	0.019	0.243	4.748	0.096	wt
31251145	57709.593	3.989	2441.7	1.112	0.023	0.152	5.116	0.128	wt
31251146	57711.552	3.990	3537.3	0.858	0.017	0.176	5.091	0.127	wt
31251147	57713.318	3.990	3640.3	0.838	0.017	0.167	4.123	0.105	wt
31251148	57715.571	3.991	3810.2	0.606	0.014	0.181	3.737	0.119	wt
31251149	57716.105	3.991	1090.7	0.317	0.017	0.001	2.325	0.125	pc
31251150	57717.365	3.992	957.8	0.360	0.019	0.001	3.257	0.176	pc
31251151	57718.827	3.992	945.3	0.212	0.015	0.001	3.304	0.234	pc
31251152	57719.489	3.992	992.9	0.264	0.016	0.001	2.753	0.171	pc
31251153	57720.058	3.993	2785.6	0.286	0.010	0.001	3.065	0.109	pc
31251154	57721.813	3.993	1822.8	0.233	0.011	0.001	2.830	0.138	pc
31251155	57722.509	3.994	1790.2	0.199	0.011	0.001	2.350	0.125	pc
31251156	57723.450	3.994	1973.2	0.251	0.011	0.002	2.564	0.116	pc
31251157	57724.376	3.994	2038.4	0.288	0.012	0.001	3.041	0.126	pc
31251158	57725.441	3.995	2015.9	0.205	0.010	0.001	2.747	0.136	pc
31251159	57726.370	3.995	2173.8	0.245	0.011	0.001	2.803	0.122	pc
31251160	57727.440	3.995	1890.5	0.252	0.012	0.002	2.561	0.118	pc
31251161	57728.168	3.995	1913.1	0.248	0.011	0.002	2.935	0.136	pc
31251162	57729.169	3.996	1353.9	0.163	0.011	0.001	1.967	0.133	pc
31251163	57730.396	3.996	2020.9	0.192	0.010	0.002	2.577	0.132	pc
31251164	57731.087	3.996	1925.6	0.256	0.012	0.002	2.569	0.116	pc
31251165	57732.284	3.997	1429.2	0.143	0.010	0.001	2.121	0.149	pc
31251166	57733.149	3.997	1807.8	0.215	0.011	0.002	2.088	0.107	pc
31251167	57734.211	3.998	1720.0	0.129	0.009	0.001	1.770	0.120	pc
31251168	57735.939	3.998	1689.9	0.217	0.011	0.002	2.108	0.111	pc
31251169	57736.139	3.998	1750.1	0.188	0.010	0.002	1.692	0.094	pc
31251170	57737.338	3.999	2010.9	0.204	0.010	0.002	1.781	0.089	pc
31251171	57738.538	3.999	1913.1	0.064	0.006	0.000	1.163	0.105	pc
31251172	57739.202	3.999	1888.0	0.107	0.008	0.002	1.410	0.100	pc
31251173	57740.067	4.000	2098.6	0.066	0.006	0.001	1.023	0.088	pc
31251174	57741.123	4.000	1579.6	0.076	0.007	0.001	1.290	0.119	pc

Table A2 *(continued)*

Sequence	MJD	Phase	Expo.	Net Rate	Rate Error	Bkg Rate	Flux	Error	Mode
			s	cts/s	cts/s	cts/s	10^{-11} ergs/s/cm^2	10^{-11} ergs/s/cm^2	
31251175	57742.057	4.000	1426.7	0.114	0.009	0.002	1.069	0.084	pc
31251176	57743.729	4.001	1973.2	0.040	0.005	0.001	0.781	0.090	pc
31251177	57744.110	4.001	2005.8	0.040	0.005	0.001	0.880	0.100	pc
31251178	57745.836	4.002	1710.0	0.045	0.005	0.002	0.320	0.037	pc
31251179	57746.303	4.002	2051.0	0.112	0.007	0.002	0.893	0.060	pc
31251181	57748.035	4.002	2028.4	0.030	0.004	0.000	0.674	0.087	pc
31251184	57751.224	4.003	2046.0	0.029	0.004	0.002	0.313	0.042	pc
31251185	57752.617	4.004	2098.6	0.037	0.004	0.002	0.323	0.038	pc
31251187	57754.479	4.005	1888.0	0.030	0.004	0.002	0.300	0.041	pc
31251190	57757.669	4.006	1985.8	0.029	0.004	0.002	0.557	0.075	pc
31251195	57762.442	4.007	1950.7	0.030	0.004	0.001	0.613	0.082	pc
31251196	57763.843	4.008	1607.2	0.037	0.005	0.000	1.064	0.138	pc
31251198	57765.037	4.008	1338.9	0.045	0.006	0.001	0.847	0.110	pc
31251199	57766.433	4.009	1960.7	0.070	0.006	0.002	0.980	0.085	pc
31251200	57767.892	4.009	1732.5	0.179	0.010	0.002	1.267	0.072	pc
31251201	57768.130	4.009	1945.7	0.082	0.007	0.001	1.394	0.112	pc
31251202	57769.887	4.010	1180.9	0.085	0.009	0.001	1.090	0.110	pc
31251203	57770.748	4.010	2033.4	0.078	0.006	0.001	1.099	0.088	pc
31251204	57771.081	4.010	1915.6	0.116	0.008	0.002	1.366	0.092	pc
31251205	57772.149	4.011	1993.3	0.226	0.011	0.002	1.791	0.085	pc
31251206	57773.507	4.011	1993.3	0.187	0.010	0.002	1.672	0.087	pc
31251207	57774.140	4.011	2023.4	0.080	0.006	0.001	1.283	0.101	pc
31251208	57775.869	4.012	1968.2	0.174	0.009	0.002	1.959	0.107	pc
31251209	57776.341	4.012	2025.9	0.130	0.008	0.001	1.703	0.106	pc
31251210	57777.061	4.012	1945.7	0.146	0.009	0.002	1.529	0.091	pc
31251211	57778.394	4.013	1624.7	0.162	0.010	0.001	1.773	0.110	pc
31251213	57780.261	4.013	1028.0	0.234	0.015	0.002	2.305	0.150	pc
31251214	57781.160	4.014	987.9	0.125	0.011	0.001	1.656	0.150	pc
31251215	57782.586	4.014	1286.2	0.220	0.013	0.002	2.183	0.131	pc
31251216	57783.323	4.015	1948.2	0.227	0.011	0.002	1.937	0.093	pc
31251217	57784.712	4.015	1948.2	0.136	0.008	0.001	1.652	0.102	pc
31251218	57785.836	4.015	1960.7	0.198	0.010	0.002	2.117	0.108	pc
31251219	57786.772	4.016	1873.0	0.172	0.010	0.002	1.833	0.103	pc
31251221	57787.230	4.016	1955.7	0.188	0.010	0.001	2.048	0.107	pc
31251220	57788.262	4.016	1602.2	0.227	0.012	0.002	2.313	0.122	pc
31251222	57789.267	4.017	1659.8	0.284	0.013	0.002	2.613	0.121	pc
31251223	57790.073	4.017	759.7	0.239	0.018	0.002	2.342	0.175	pc
31251224	57793.823	4.018	1682.4	0.243	0.012	0.002	2.307	0.115	pc
31251225	57796.605	4.019	1993.3	0.267	0.012	0.002	2.546	0.111	pc
31251226	57799.036	4.020	1634.8	0.263	0.013	0.002	2.325	0.113	pc
31251227	57802.395	4.021	1955.7	0.243	0.011	0.002	2.453	0.113	pc
31251228	57805.497	4.022	1915.6	0.235	0.011	0.002	2.212	0.105	pc
31251229	57808.301	4.023	2336.8	0.236	0.010	0.001	2.203	0.094	pc
31251230	57811.876	4.024	1950.7	0.262	0.012	0.002	2.081	0.093	pc
31251233	57820.708	4.027	2088.6	0.267	0.011	0.001	2.411	0.103	pc
31251234	57823.143	4.028	2000.8	0.267	0.012	0.002	2.507	0.109	pc
31251235	57826.625	4.029	2143.7	0.251	0.011	0.002	2.189	0.095	pc
31251236	57830.194	4.031	376.1	0.160	0.021	0.000	2.256	0.292	pc
31251237	57832.804	4.032	586.7	0.210	0.019	0.001	2.159	0.195	pc
31251238	57835.538	4.033	1273.7	0.251	0.014	0.002	2.085	0.117	pc
31251239	57838.334	4.034	1456.7	0.237	0.013	0.001	2.168	0.117	pc
31251240	57841.727	4.035	1890.5	0.248	0.011	0.002	2.001	0.093	pc

Table A2 *(continued)*

Sequence	MJD	Phase	Expo.	Net Rate	Rate Error	Bkg Rate	Flux	Error	Mode
			s	cts/s	cts/s	cts/s	10^{-11} ergs/s/cm^2	10^{-11} ergs/s/cm^2	
31251241	57844.747	4.036	1396.6	0.313	0.015	0.002	2.276	0.110	pc
31251242	57847.364	4.037	1940.7	0.262	0.012	0.002	1.996	0.089	pc
31251243	57850.963	4.038	1850.4	0.231	0.011	0.001	1.950	0.095	pc
31251244	57853.379	4.039	2008.3	0.288	0.012	0.002	2.391	0.100	pc
31251245	57856.203	4.040	426.2	0.188	0.021	0.000	2.122	0.238	pc
31251246	57859.454	4.041	1885.5	0.348	0.014	0.002	2.360	0.093	pc
31251247	57862.241	4.042	2033.4	0.354	0.013	0.002	2.212	0.083	pc
31251248	57864.275	4.043	1451.7	0.324	0.015	0.002	2.113	0.098	pc
31251249	57868.657	4.044	845.0	0.264	0.018	0.001	1.753	0.118	pc
31251250	57872.181	4.045	564.1	0.289	0.023	0.001	2.120	0.166	pc
31251251	57873.165	4.046	639.4	0.316	0.022	0.002	2.350	0.166	pc
31251252	57881.219	4.048	1414.1	0.201	0.012	0.001	2.104	0.125	pc
31251253	57883.899	4.049	1085.7	0.300	0.017	0.001	1.907	0.106	pc
10120001	57890.690	4.052	2146.2	0.340	0.013	0.002	2.199	0.082	pc
10120002	57897.824	4.054	455.7	0.189	0.030	0.209	1.359	0.417	wt
10120003	57904.497	4.056	2786.5	0.480	0.016	0.208	2.310	0.116	wt
10120004	57911.366	4.059	2456.7	0.532	0.018	0.223	2.094	0.109	wt
10120005	57918.143	4.061	975.7	0.216	0.020	0.180	0.832	0.184	wt
10120006	57919.007	4.061	457.2	0.513	0.038	0.162	2.518	0.277	wt
10120007	57922.434	4.063	757.0	0.521	0.030	0.175	2.294	0.201	wt
10120008	57925.561	4.064	1637.8	0.562	0.021	0.165	2.021	0.117	wt
10120009	57932.765	4.066	407.8	0.592	0.044	0.213	1.888	0.227	wt
10120010	57935.227	4.067	595.1	0.253	0.023	0.053	2.572	0.320	wt
10120011	57939.278	4.068	2692.5	0.537	0.017	0.224	1.827	0.094	wt
10120012	57946.750	4.071	2077.3	0.565	0.019	0.164	1.896	0.099	wt
10120013	57953.124	4.073	2451.5	0.324	0.014	0.150	1.656	0.121	wt
10120014	57960.541	4.076	2748.9	0.316	0.013	0.183	1.157	0.098	wt
10120015	57967.472	4.078	2461.2	0.461	0.016	0.205	1.712	0.103	wt
10120016	57974.481	4.081	1805.6	0.601	0.021	0.180	1.938	0.105	wt
10120017	57981.389	4.083	644.6	0.507	0.033	0.204	2.241	0.226	wt
10120018	57990.602	4.086	1331.4	0.552	0.023	0.175	2.031	0.134	wt
10120019	57997.567	4.089	999.3	0.555	0.027	0.152	1.679	0.131	wt
10120020	58003.721	4.091	2017.7	0.464	0.018	0.168	1.570	0.102	wt
10120022	58016.156	4.095	3024.0	0.587	0.017	0.272	1.736	0.084	wt
10120023	58023.530	4.098	1466.9	0.634	0.022	0.069	1.810	0.094	wt
10120024	58030.281	4.100	2271.1	0.662	0.019	0.180	1.713	0.081	wt
10120025	58037.653	4.102	1687.7	0.413	0.019	0.215	1.368	0.117	wt
10120026	58044.576	4.105	1046.1	0.603	0.027	0.149	1.608	0.117	wt
10120027	58051.536	4.107	2861.5	0.580	0.016	0.155	1.451	0.069	wt
10120029	58065.293	4.112	2865.2	0.470	0.015	0.182	1.188	0.072	wt
10120030	58072.486	4.114	2438.9	0.577	0.018	0.176	1.804	0.088	wt
10120031	58079.928	4.117	2853.9	0.638	0.016	0.134	1.726	0.071	wt
10120032	58086.172	4.119	2313.9	0.324	0.014	0.147	0.746	0.078	wt
10120033	58093.384	4.122	2188.3	0.642	0.020	0.205	1.151	0.067	wt
10120034	58100.264	4.124	2414.0	0.553	0.017	0.159	1.135	0.067	wt
10120035	58107.425	4.126	1216.9	0.520	0.023	0.152	1.171	0.099	wt
10120036	58114.930	4.129	1436.8	0.622	0.023	0.144	1.308	0.085	wt
10120037	58121.637	4.131	2414.0	0.595	0.019	0.313	1.334	0.081	wt
10120038	58128.947	4.134	2312.7	0.651	0.019	0.162	1.365	0.068	wt
10120039	58135.053	4.136	2353.7	0.630	0.018	0.143	1.518	0.073	wt
10120040	58142.072	4.138	2201.0	0.516	0.018	0.176	1.017	0.070	wt
10120041	58149.843	4.141	2433.1	0.583	0.018	0.204	1.208	0.070	wt

Table A2 *continued on next page*

Table A2 *(continued)*

Sequence	MJD	Phase	Expo.	Net Rate	Rate Error	Bkg Rate	Flux	Error	Mode
			s	cts/s	cts/s	cts/s	10^{-11} ergs/s/cm^2	10^{-11} ergs/s/cm^2	
10120042	58156.858	4.144	2360.9	0.522	0.018	0.224	1.075	0.073	wt
10120043	58163.725	4.146	2285.0	0.583	0.019	0.219	1.332	0.077	wt
10120044	58170.794	4.148	2402.6	0.444	0.017	0.225	1.395	0.096	wt
10120045	58177.826	4.151	2393.5	0.639	0.018	0.158	1.295	0.066	wt
10120046	58184.932	4.153	2395.5	0.593	0.018	0.152	1.292	0.068	wt
10120047	58194.542	4.157	1000.7	0.455	0.026	0.205	1.013	0.117	wt
10120048	58198.239	4.158	1175.3	0.523	0.024	0.168	1.252	0.106	wt
10120049	58205.806	4.160	2415.7	0.539	0.018	0.233	1.061	0.070	wt
10120050	58212.742	4.163	1532.4	0.648	0.023	0.198	1.171	0.080	wt
10120051	58213.248	4.163	1430.5	0.626	0.023	0.117	1.070	0.073	wt
10120052	58219.901	4.165	261.4	0.414	0.042	0.054	1.543	0.253	wt
10120053	58226.621	4.168	2361.8	0.566	0.017	0.090	0.975	0.056	wt
10120054	58233.622	4.170	1859.5	0.526	0.018	0.086	1.244	0.075	wt
10120055	58240.792	4.173	2366.9	0.520	0.016	0.087	1.571	0.078	wt
10120056	58254.560	4.177	1477.4	0.521	0.020	0.062	1.082	0.075	wt
10120057	58259.768	4.179	2312.7	0.473	0.015	0.079	1.115	0.067	wt
10120058	58285.154	4.188	3863.3	0.529	0.013	0.087	1.335	0.055	wt
10120059	58315.092	4.198	2330.1	0.656	0.018	0.064	1.214	0.056	wt
10120060	58350.252	4.210	4018.0	0.542	0.012	0.067	1.045	0.044	wt
10120061	58381.424	4.221	4319.8	0.610	0.013	0.070	0.958	0.038	wt
10120062	58409.370	4.231	3920.4	0.534	0.012	0.059	0.946	0.042	wt
10120064	58469.033	4.251	4891.4	0.462	0.011	0.088	1.068	0.046	wt
10120065	58497.413	4.261	4645.9	0.584	0.012	0.090	0.996	0.039	wt
10120066	58528.856	4.272	4949.3	0.627	0.012	0.077	0.988	0.036	wt
10120067	58556.820	4.282	4917.7	0.541	0.011	0.075	0.809	0.035	wt
10120068	58587.463	4.292	4861.5	0.634	0.012	0.064	0.899	0.034	wt

Table A3. Log of *NICER* Observations and Fluxes

Sequence	MJD	Phase	Expo.	Net Rate	Rate Error	Bkg Rate	Flux	Error
			s	cts/s	cts/s	cts/s	10^{-11} ergs/s/cm^2	10^{-11} ergs/s/cm^2
1120010102	58073.892	4.115	146.6	8.70	0.25	0.44	1.95	0.08
1120010103	58074.342	4.115	57.4	7.70	0.43	2.68	1.55	0.12
1120010105	58078.770	4.117	187.9	7.94	0.22	1.15	1.78	0.07
1120010106	58079.797	4.117	216.8	7.60	0.20	1.00	1.80	0.07
1120010107	58080.471	4.117	2075.0	7.65	0.06	0.64	1.61	0.02
1120010108	58081.565	4.118	4362.0	7.81	0.04	0.70	1.74	0.01
1120010109	58082.338	4.118	4460.0	7.79	0.04	0.70	1.66	0.01
1120010110	58105.784	4.126	3067.7	7.68	0.05	1.23	1.54	0.02
1120010111	58113.712	4.129	2025.9	8.07	0.06	0.43	1.64	0.02
1120010112	58119.076	4.131	2413.4	7.77	0.06	0.64	1.49	0.02
1120010113	58124.348	4.132	1936.5	8.05	0.07	0.46	1.58	0.02
1120010114	58126.921	4.133	1919.9	8.04	0.07	0.82	1.63	0.02
1120010115	58127.050	4.133	1548.9	8.18	0.07	0.52	1.68	0.02
1120010119	58155.869	4.143	1622.6	8.12	0.07	0.54	1.50	0.02
1120010120	58156.416	4.143	3852.5	8.23	0.05	0.43	1.55	0.01
1120010121	58163.299	4.146	1172.3	7.98	0.08	0.47	1.42	0.02
1120010123	58167.376	4.147	237.2	7.85	0.19	0.60	1.42	0.05
1120010124	58168.149	4.147	81.4	7.20	0.31	0.76	1.35	0.09

Table A3 *continued on next page*

Table A3 *(continued)*

Sequence	MJD	Phase	Expo.	Net Rate	Rate Error	Bkg Rate	Flux	Error
			s	cts/s	cts/s	cts/s	10^{-11} ergs/s/cm^2	10^{-11} ergs/s/cm^2
1120010125	58169.888	4.148	298.0	8.23	0.17	0.52	1.42	0.04
1120010126	58175.454	4.150	644.1	7.95	0.11	0.54	1.31	0.03
1120010127	58176.034	4.150	203.5	7.63	0.20	0.63	1.31	0.05
1120010129	58178.510	4.151	1736.0	7.70	0.07	0.79	1.29	0.02
1120010130	58179.572	4.151	1945.0	8.06	0.07	0.60	1.34	0.02
1120010132	58186.544	4.154	174.3	7.42	0.22	1.15	1.18	0.06
1120010133	58187.655	4.154	460.6	8.41	0.14	0.39	1.42	0.03
1120010134	58188.476	4.154	253.1	8.37	0.19	0.80	1.46	0.05
1120010135	58189.312	4.155	481.2	8.65	0.14	0.38	1.37	0.03
1120010136	58190.663	4.155	343.1	8.29	0.16	0.81	1.38	0.04
1120010137	58191.504	4.156	2870.5	7.84	0.06	0.94	1.21	0.01
1120010138	58198.162	4.158	3760.6	8.39	0.05	0.32	1.38	0.01
1120010140	58205.365	4.160	1540.0	9.06	0.08	0.60	1.53	0.02
1120010141	58206.102	4.161	477.0	8.46	0.14	0.58	1.39	0.03
1120010145	58228.700	4.168	223.3	7.59	0.22	3.31	1.04	0.05
1120010146	58229.752	4.169	4501.1	8.10	0.04	0.82	1.27	0.01
1120010147	58234.348	4.170	4385.0	8.48	0.05	0.46	1.31	0.01
1120010149	58240.613	4.172	702.3	8.03	0.11	0.44	1.23	0.03
1120010150	58257.083	4.178	3158.6	8.54	0.05	0.38	1.28	0.01
1120010151	58275.912	4.185	2509.0	8.86	0.06	0.60	1.37	0.01
1120010152	58292.948	4.191	679.5	8.83	0.12	0.40	1.39	0.03
1120010153	58293.076	4.191	1513.5	8.33	0.08	0.64	1.24	0.02
1120010155	58305.503	4.195	845.6	8.23	0.10	0.74	1.18	0.02
1120010156	58307.271	4.196	1411.8	8.93	0.08	0.37	1.25	0.02
1120010158	58313.276	4.198	820.0	8.54	0.11	0.67	1.22	0.02
1120010160	58338.280	4.206	2500.9	8.47	0.06	0.75	1.19	0.01
1120010161	58368.714	4.217	2063.6	8.41	0.07	0.76	1.14	0.01
1120010162	58388.526	4.224	2070.2	8.65	0.07	0.59	1.21	0.01
1120010163	58396.959	4.227	391.9	8.72	0.16	1.21	1.14	0.03
1120010164	58397.538	4.227	814.4	8.69	0.11	0.50	1.12	0.02
1120010165	58398.247	4.227	971.5	8.69	0.10	0.35	1.16	0.02
1120010166	58399.244	4.227	1738.7	8.64	0.07	1.08	1.19	0.02
1120010167	58407.352	4.230	1173.0	8.94	0.09	0.37	1.16	0.02
1120010168	58410.572	4.231	1160.0	8.61	0.09	0.62	1.14	0.02
1120010173	58434.738	4.240	3080.0	8.81	0.06	0.59	1.17	0.01
1120010174	58435.256	4.240	3502.1	8.98	0.05	0.84	1.20	0.01
1120010175	58436.471	4.240	1494.4	8.37	0.08	0.80	1.03	0.02
1120010176	58442.945	4.242	545.7	9.28	0.13	0.37	1.26	0.03
1120010178	58451.049	4.245	870.4	9.33	0.11	1.01	1.29	0.02
1120010179	58455.360	4.247	880.1	8.97	0.11	0.76	1.16	0.02
1120010181	58472.300	4.253	2181.9	9.09	0.07	0.55	1.15	0.01
1120010183	58483.692	4.256	2137.9	8.92	0.07	0.55	1.10	0.01
1120010184	58488.217	4.258	273.0	9.23	0.20	1.17	1.25	0.04
1120010185	58489.955	4.259	302.8	8.80	0.18	1.10	1.10	0.04
1120010186	58490.019	4.259	306.3	8.81	0.17	0.56	1.07	0.04
1120010188	58530.411	4.273	1288.8	8.64	0.08	0.54	1.03	0.02
1120010189	58534.274	4.274	462.4	8.69	0.14	0.47	1.03	0.03
1120010190	58538.910	4.276	526.1	8.43	0.13	0.75	0.99	0.03
1120010191	58539.104	4.276	503.5	8.90	0.14	0.45	1.09	0.03
2120010101	58546.180	4.278	1518.5	8.88	0.08	0.53	1.04	0.02
2626010101	58563.955	4.284	1311.4	8.80	0.08	0.42	1.02	0.02
2626010201	58577.389	4.289	524.8	8.68	0.13	0.51	1.00	0.03

Table A3 *continued on next page*

Table A3 *(continued)*

Sequence	MJD	Phase	Expo.	Net Rate	Rate Error	Bkg Rate	Flux	Error
			s	cts/s	cts/s	cts/s	10^{-11} ergs/s/cm^2	10^{-11} ergs/s/cm^2
2626010301	58592.002	4.294	1577.0	8.40	0.08	0.80	0.92	0.01
2626010501	58622.278	4.304	1161.6	8.72	0.09	0.39	0.98	0.02
2626010601	58634.189	4.308	934.3	8.74	0.10	0.79	1.01	0.02
2626010801	58659.323	4.317	2337.6	8.86	0.06	0.34	0.99	0.01
2626010901	58675.812	4.323	1422.5	8.71	0.08	0.50	0.94	0.02
2626011201	58722.301	4.339	940.9	9.11	0.10	0.48	1.02	0.02
2626011301	58732.468	4.342	552.0	8.24	0.13	1.25	0.89	0.03
2626011401	58745.866	4.347	1098.2	8.73	0.09	0.45	0.94	0.02
2626011501	58759.676	4.352	833.5	8.87	0.11	0.64	0.91	0.02
2626011601	58777.959	4.358	985.6	8.51	0.10	0.97	0.89	0.02
2626012201	58854.095	4.384	502.3	8.99	0.14	1.09	0.98	0.03
2626012301	58859.644	4.386	1601.0	8.88	0.08	1.12	0.97	0.01
2626012401	58879.728	4.393	3673.9	8.65	0.05	0.55	0.86	0.01
2626012601	58907.306	4.403	1486.5	8.95	0.08	0.50	0.90	0.01
3591010101	58922.412	4.408	605.1	8.52	0.12	0.76	0.85	0.02
3591010301	58949.363	4.417	1762.4	8.84	0.07	0.50	0.89	0.01
3591010401	58962.857	4.422	1222.3	8.93	0.09	0.82	0.89	0.02
3591010601	58990.537	4.432	2249.3	8.67	0.07	0.93	0.86	0.01
3591010701	59002.117	4.436	1291.7	9.14	0.09	0.67	0.94	0.02